POLITECNICO DI TORINO

DOCTORAL SCHOOL

Ph.D. in Engineering for Natural and Built Environment – XXVII cycle

Ph.D. Thesis

Mathematical modelling of cardiovascular fluid mechanics: physiology, pathology and clinical practice

Andrea Guala

Supervisors
Prof. Carlo Camporeale
Prof. Luca Ridolfi

Ph.D. coordinator
Prof. Claudio Scavia

January 2015

Andrea Guala
Email: andrea.guala@polito.it

Politecnico di Torino
Department of Environment, Land and Infrastructure Engineering
Corso Duca degli Abruzzi, 24 - 10129 Torino, ITALY

Cover illustration: Eréndida Mancilla

Contents

Abstract

The cardiovascular apparatus is a complex dynamical system that carries oxygen and nutrients to cells, removes carbon dioxide and wastes and performs several other tasks essential for life. The physically-based modelling of the cardiovascular system has a long history, which begins with the simple lumped Windkessel model by O. Frank in 1899. Since then, the development has been impressive and a great variety of mathematical models have been proposed.

The purpose of this Thesis is to analyse and develop two different mathematical models of the cardiovascular system able to (i) shed new light into cardiovascular ageing and atrial fibrillation and to (ii) be used in clinical practice. To this aim, in-house codes have been implemented to describe a lumped model of the complete circulation and a multi-scale (1D/0D) model of the left ventricle and the arterial system. We then validate each model. The former is validated against literature data, while the latter against both literature data and numerous in-vivo non-invasive pressure measurements on a population of six healthy young subjects.

Afterwards, the confirmed effectiveness of the models has been exploited. The lumped model has been used to analyse the effect of atrial fibrillation. The multi-scale one has been used to analyse the effect of ageing and to test the feasibility of clinical use by means of central-pressure blind validation of a parameter setting unambiguously defined with only non-invasive measurements on a population of 52 healthy young men. All the applications have been successful, confirming the effectiveness of this approach. Pathophysiology studies could include mathematical model in their setting, and clinical use of multi-scale mathematical model is feasible.

Introduction

The mathematical modelling of the cardiovascular system is a fast-growing research field. Considering that in Europe cardiovascular diseases cause over 4 million deaths yearly [120], accounting alone for around half of all deaths, and pondering that the overall cardiovascular diseases-related cost has been estimated to be around €200 billion a year [120], it is easy to understand such an increasing interest. Indeed, related mathematical models have already proven to be helpful in understanding cardiovascular system in physiological and pathological condition, forecasting its evolution and supporting measurement instruments.

Although the cardiovascular apparatus is a very complex dynamical system, its physically-based modelling has a long history. Indeed, we have to go back to Leonhard Euler who wrote in 1775 the first set of one-dimensional equation representing the blood flow in arteries [28]. However, such a set of equation was by far too complex to be solved at that time, and the first successful application of fluid-mechanics knowledge can be considered as beginning with the much more simple lumped Windkessel model proposed by O. Frank in 1899, more than one hundred years later, exploiting the concept of electrical analogy. We now call this first lumped model ""two-element Windkessel model"", because the overall response of the cardiovascular system is described by means of a resistance and a capacitance [183]. The following crucial step on lumped description of the cardiovascular system happened again almost one hundred years later, in 1971, when Westerhof and colleagues introduced a third element: the inlet characteristic impedance, thus correcting the erroneous continuous decrease on impedance at high frequencies [193]. Even if a further effective improvement has been proposed by Stergiopulos and co-workers [170] in 1999, by adding an inertance

in order to correct the low frequency inconsistency of the three-element Windkessel model, the great majority of successive works has been using Westerhof's version.

However, the blood motion in the cardiovascular system is mainly a phenomenon of wave propagation and reflection, and arteries are far from being uniform through the bifurcating tree. Consequently, in order to improve the predictive capacities of lumped description, several authors have worked on different wave-transmission model, where multiple lumped block have been assembled in a tree-like structure, finally producing a better approximation of the local flow field. The advantages of this description were mainly consequent to the better description of local geometrical and mechanical property, but the effectiveness of the resulting propagation phenomena have been questioned. It is only in 2004 that the formal proof of the distributed lumped model as a first order approximation of linear one dimensional model has been given [110]. The continuous arterial tree was thus broken in an growing number of increasingly-smaller compartments, until continuous description has been introduced. One dimensional models were the first type of continuous models proposed, due to their relative simplicity. From the first linear one dimensional description several improvements have been made. The inclusion of non-linear convective acceleration, the arterial tapering, the non-linear viscoelastic mechanical properties of vessel walls, the imposed velocity profile and the distal boundary conditions can be considered as the most important examples of subsequent improvements. Furthermore, thanks to the huge advances on both medical imaging technique and computing capacities, two- and three-dimensional models have been proposed. Two-dimensional models have been set apart while three-dimensional characterization is likely to have a brilliant future in cardiovascular modelling. Despite a recent first successful implementation of full-scale three-dimensional representation [200], such a description is still to expensive in terms of input information and computational cost, at least when deformable arterial walls are considered.

The present Thesis arises from the fundamental hypotheses that mathematical description of the cardiovascular system can shed new light on cardiovascular pathophysiology and that it can be effectively used in clinical practice. To this aim, in-house codes have been implemented. We thus designed a lumped model of

the complete circulation and a multi-scale (1D/0D) one of the left ventricle and the arterial system.

The Thesis is organized as follow. In the first Chapter the cardiovascular system is introduced. The second Chapter is dedicated to the description of the two mathematical models. The third Chapter contains the validation and the applications of the lumped model. Later, atrial fibrillation is simulated and deeply analysed. In Chapter four the use of the multi-scale model is presented. Firstly we validate the model against literature data. Afterwards, we develop a subject-specific setting procedure based on non-invasive measurements and validate it against *in-vivo* data from a population of six healthy young subjects. Such a subject-specific setting is then improved and blindly tested against a much larger population with the aim of testing its performance on central pressure evaluation. Finally, the multi-scale mathematical model is further used to analyse ageing. By imposing age-dependence of several key parameters, we reproduce the main feature of an ageing arterial system. Analysing the obtained results, an embracing description of cardiovascular ageing is proposed.

Chapter 1

The cardiovascular system

The cardiovascular apparatus is a complex dynamical system that comprises blood, heart and a hierarchy of different vessels. This system carries oxygen and nutrients to cells, removes carbon dioxide and wastes, stabilizes body temperature, maintains homoeostasis and performs several other tasks essential for life.

The left ventricle forces blood to move through the bifurcating tree that is composed by large arteries, which distribute the blood to various districts, followed by middle and small arteries and capillaries, which diffuse the blood to whole human volume. Once nutrients have been exchanged with wastes at the cellular level, exhausted blood is collected by the smallest veins, which merge into bigger and bigger veins finally reaching the heart again. The loop is then closed by the pumping function of the right heart, which forces blood through pulmonary circulation, lastly arriving back to the left atrium and ventricle.

The aim of this first Chapter is to introduce the reader to the principal constituents of the cardiovascular system and to briefly explain the main processes involved in such a very complex system. We firstly start from blood, analysing his composition and rheological properties. Afterwards, heart structures and their functioning will be discussed. Finally, we will focus on arteries, veins, capillary beds and pulmonary circulation.

1.1 Blood

Blood is formed by a liquid, called plasma, where different particles are suspended. The principal role of blood is to transport oxygen and nutrients to tissues and to remove waste elements, but other fundamental functions are connected to heat dissipation and to elimination of external biological agents.

A description of the main components of blood is proposed in the next paragraphs.

Blood plasma Blood plasma is a pale-yellow liquid mainly composed by water (for more than 90%), proteins (around 7 %) and mineral nutrients. Rheologically, blood density is normally around 1.06 g/cm^3, and it varies slightly even in pathological condition [193], while blood viscosity, depending on plasma viscosity, temperature, hematocrit, vessel size, shear stress, etc., sharply changes, easily ranging from being 10 to 60% more viscous than water at a temperature of 20°C. Blood plasma viscosity strongly depends on temperature and red blood cells prevalence, and can be importantly affected by some pathologies, like Multiple myeloma, among others.

Blood plasma protein content is fundamental in maintaining the osmotic pressure, which regulates the exchange between intra and extra-vascular substances. Although a detailed description of such a mechanism is out of the scope of the present work, it is important to highlight how the force that moves substances across permeable materials depends on relative concentration of the solutes.

Red blood cells The most present particles suspended in blood plasma are red blood cells, also called erythrocytes, which transport oxygen in the arterial circulation and carbon dioxide in the venous side. Red blood cells are composed by water (around 65% in weight), haemoglobin (around 32% in weight) with a small presence of inorganic substances like potassium, sodium, magnesium and calcium.

The volumetric concentration of red blood cells in the blood is called hematocrit. Considering that normal values of hematocrit are around 40-45 % the red blood cells relevance into viscosity [10;93]

is straightforward. In detail, there is about 4% increase of blood viscosity per unit increase of hematocrit [10].

Red blood cells are characterized by a biconcave disk-shape with a diameter of around 7 micrometers. This particular shape provides great flexibility, allowing the passage in section much smaller than their undeformed dimension. In fact, when red blood cells are forced to pass through small sections, so when strong tangential forces act on their surface, they are able to largely deform, as illustrated in figure 1.1.

Figure 1.1. Red blood cell deformation when passing through microcirculation. (Reproduced from Schmid-Schönbein *et al.* [158].)

Another important rheological feature of red blood cells is their tendency to aggregate into *rouleaux*, i.e. linear aggregates arranged like stacks of coins. Such an aggregation is influenced by the shearing forces and impacts the overall blood rheological properties. Cumulated size of particles augments viscosity [10] and amplifies disturbance of the flow. In figure 1.2 an example of rouleaux aggregation patterns is showed.

White blood cells White blood cells, also called leukocytes, are particles of different size that occupy a small volume on the

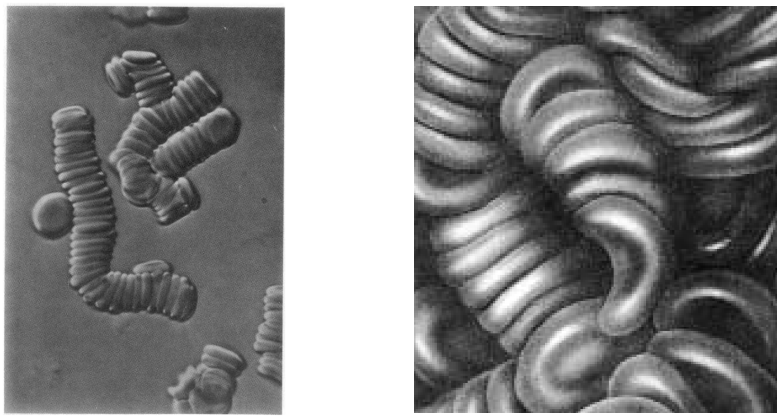

Figure 1.2. Left: lateral vision of rouleaux (From Bessis [16]). Right: red blood cells aggregates. (Reproduced from Schmid-Schönbein *et al.* [158].)

blood. White blood cells play a vital role, protecting the body from infectious processes either through physical removal of microorganisms or by the production of antibodies. Being white blood cells number and volumetric concentration smaller than other cellular elements of blood, they have negligible effect on blood viscosity in large vessels [10], although they can play a role in very small conduits.

Platelets Also called thrombocytes, platelets are very small particles (2-3 micrometers) whose main function is to contribute to hemostasis, i.e. the process of stopping bleeding through a damaged blood vessel. As shown in figure 1.3, inactivated platelets are biconvex discoid structures but during the activation they underneath morphological changes that produce numerous dendrites playing a key role in the aggregation phase.

Since both number and size are relatively low, inactivated platelets do not influence blood flow in a substantial way.

1.2 Heart

The heart is the principal organ of the cardiovascular system. Functioning as a pump, the heart is able to eject into the arterial tree the amount of blood needed to irrigate all human tissues. The heart is

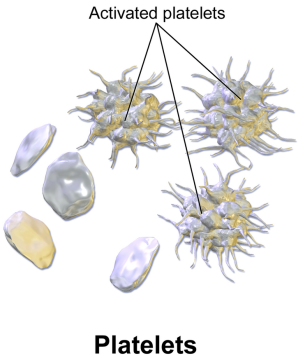

Figure 1.3. Platelet activation. (Reproduced from Blausen gallery 2014[169])

located into the thoracic cavity, it is contained by the pericardium and protected by the chest.

In figures 1.4 and 1.5 the heart structures and main blood flux directions are shown. The heart is divided by the interatrial and interventricular septa into two main parts, the right and the left heart, which in turn are divided into an atrium and a ventricle by means of atrioventricular valves.

The left and right atria are positioned in the upper part and receive blood from pulmonary veins and the venae cavae, respectively, while left and right ventricles receive blood from the corresponding atria and eject it through aorta and pulmonary arteries. Unidirectionality of the flux between atria and ventricles and between ventricles and the corresponding arteries is guaranteed by four valve: two atrioventricular and two semilunar valves.

The heart functions in a cycling way and its period depends on the overall condition of the body. A heart rate of around 55/75 beats per minute (bpm) is characteristic of a healthy heart rhythm at rest, but in case of intense physical activity it can reach 200 bpm.

Heart rhythm is generated by the sinoatrial node, an impulse-generating tissue located in the right atrium of the heart, at least

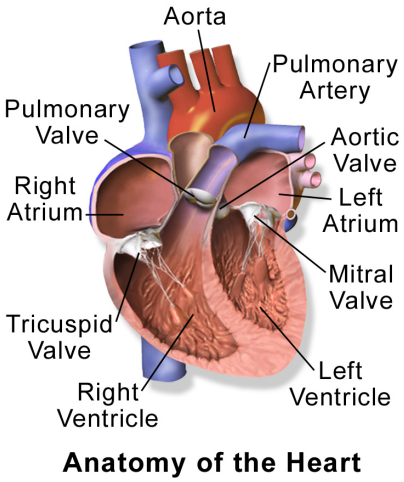

Figure 1.4. Heart physiology. (Reproduced from Blausen gallery 2014[169])

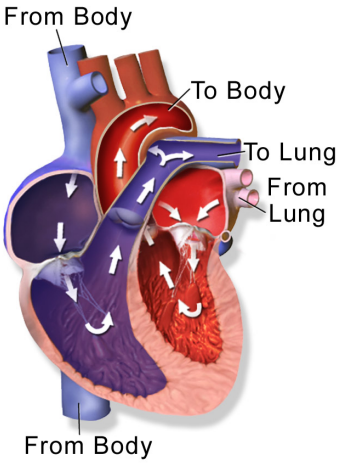

Figure 1.5. Heart blood flux directions. (Reproduced from Blausen gallery 2014[169])

in healthy condition. The sinoatrial node firstly generate the electrical impulse, which then propagates through an electrical conduction system to the whole heart. Both the sinoatrial node and the conduction system have a primary role in both heart rhythm and atrio-ventricular coordination.

Heart period is divided into two part: systole and diastole. The former is conventionally defined as the time between the beginning of (almost simultaneous) ventricular contractions and the end of ventricular ejections while the latter corresponds to the rest of the period, normally connected to the atria filling. Systolic period is thus initiated by the main electrical activation, i.e. the QRS complex of the electrocardiogram, and ends when aortic pressure exceeds the ventricular one.

In the left side of figure 1.6 a schematic representation of the heart is proposed. The division in left and right heart is highlighted by blue and red color, respectively. On the top of the right side of figure 1.6, a classical behaviour of the aortic pressure (top) and flow (bottom) are shown. The pulsatility nature of both pressure and flow is evident. Indeed the pressure profile is obtained by a first part, where pressure steeply increases, followed by a decaying phase. Analysing the graphic relative to flow, we can see how the systolic part covers less than half of the cycle. Finally, by looking at both pressure and flow charts together, one can appreciate how the ejected amount of blood increases almost instantaneously the aortic pressure, which afterwards decays during the diastolic time when flow is null. On the bottom chart of the right side, the pressure-volume loop of the left ventricle is showed. Analysing the loop from bottom right corner, we follow the isovolumic contraction phase (segment I), where the left-ventricle contract and the internal pressure increases. When internal pressure exceeds the aortic one, we enter the systolic phase (segment II), where ejection happens. When the left-ventricle has ejected the needed amount of blood, relaxation phase initiates (segment III), aortic valve closes and ventricular pressure sharply decays, finally reaching values below atrial pressure. At this point, atrioventricular valve opens, thus allowing blood to fill the ventricle (segment IV).

A brief description of the four heart chamber and of the heart valves is here proposed.

Right atrium Apart from the interatrial septum, the right

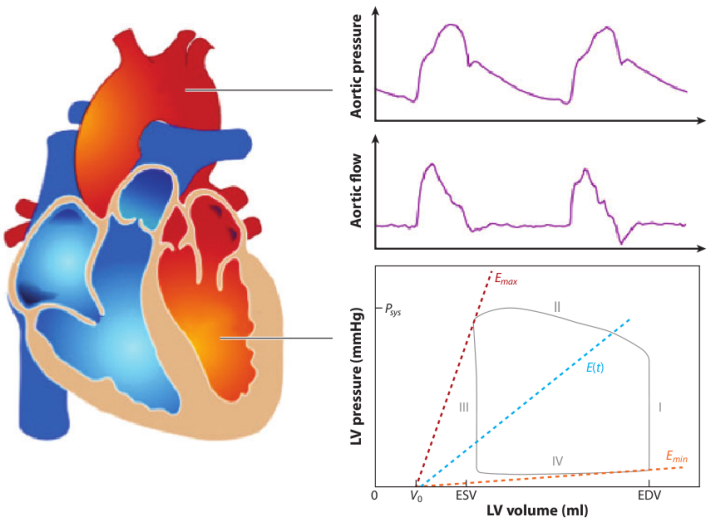

Figure 1.6. Left: schematic representation of a human heart. Right: top: aortic pressure, middle: aortic flow, bottom: left ventricular pressure-volume loop (Reproduced from van de Vosse *et al.*[183].

atrium structure is mainly constituted by the musculi pectinati. The blood reaches the right atrium from the venae cavae and the coronary sinus, and it is pushed through the unidirectional tricuspid valve to the right ventricle (see figure 1.5).

Right ventricle The right ventricle is the chamber of the human heart that has the function to send blood through the semilunar pulmonary valve to pulmonary circulation (see figure 1.5). Internally, the right ventricle presents the trabeculae carneae, a series of irregular muscolar formations forming prominent ridge.

Left atrium The left atrium collects the blood from the pulmonary veins and pumps it to the left ventricle toward the large mitral valve (see figure 1.5). The main aim of the left ventricle seems to be sustaining diastolic filling of the right ventricle both regularizing the inflow and increasing the late-diastolic pressure gradient with what is called ""atrial kick""[201].

Left ventricle The left ventricle is responsible of blood supply for the great majority of the circulation. Being filled of oxygenated blood by the left atrium, this heart chamber is able to eject a volume of blood of around 70 mL at every cycle toward the aortic

valve.

Structurally, left ventricle is formed by a succession of of layers constituted by differently-oriented fibers. In particular, longitudinal orientation characterizes the innermost (endocardial) and the outermost (epicardial) layers, where a direction valve-apex is predominant, while the fibres located in the deep myocardium are more circumferentially-oriented. Considering that muscle fibres can bear only axial tension, such an arrangement saves from the presence of weaker directions or planes[25]. A very important role on the left ventricular filling is played by its overall shape. In fact, incoming blood flow is pushed down by the forces of inertia toward the left ventricular apex. Once the blood reaches the bottom, the flow is rotated with the emergence of major vortex, addressing the flow toward the top, so as to facilitate ejection to the aorta (see figure 1.7). Very interesting works have been proposed on the

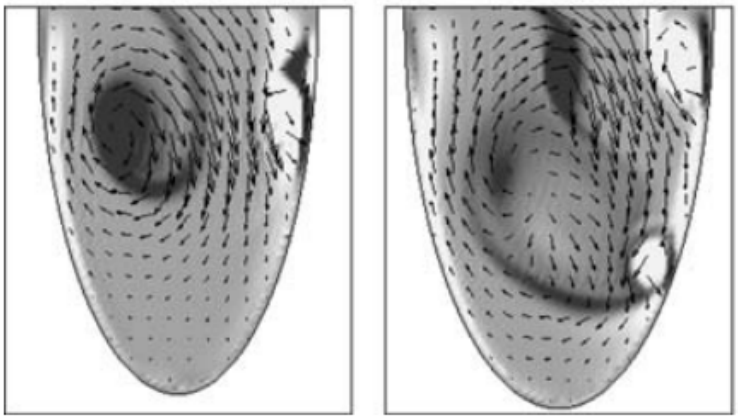

Figure 1.7. Numerical simulation of blood flow in the left ventricle (Reproduced from Pedrizzetti *et al.*[136]).

fluid mechanics of the filling and emptying left ventricle[135], where computation fluid mechanics has been able to shed new light on pathophysiology.

Heart valves The heart functioning is controlled by four unidirectional valve: tricuspid, mitral, aortic and pulmonary valve. Heart valves consist of a fibrous ring of the cardiac skeleton with a variable number of leaflet (or cusps), mainly consisting of collagen-reinforced endothelium. Since does not exist any kind of nerve

or muscle control, valve movement is fully governed by pressure gradients, inertia and viscous and turbulent forces.

In figures 1.4 and 1.8 the four valves are shown along with their reciprocal position. The heart valves function is to prevent

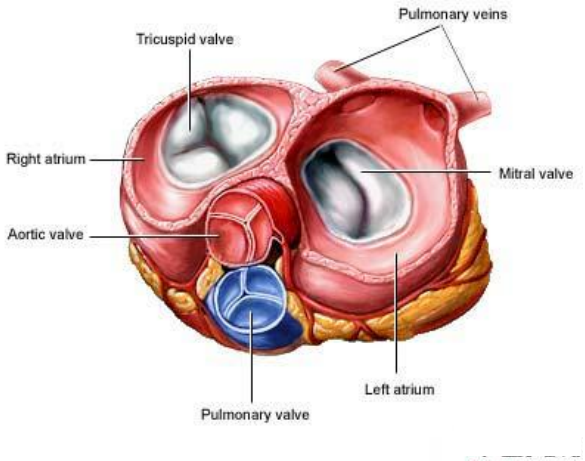

Figure 1.8. Cardiac valves.

blood backflows toward atria during systolic phase (bicuspid and tricuspid valves) or toward ventricles during the diastolic phase (semilunar valves aortic and pulmonary).

During the cardiac cycle atrioventricular valves open at the end of the ventricular systole and close when the ventricle active, while mitral and aortic valves open when ventricular pressures exceed the value at the aortic and pulmonary arteries and close when the pressure gradient is reversed.

1.3 Systemic circulation

The systemic circulation is a complex network of arteries, veins and capillaries that distributes blood throughout the body and recollects it after the chemical exchanges have taken place. As shown in figure 1.9, the systemic circulation begins, just after the aortic valve, with the ascending aorta. Afterwards, through a series of bifurcations, blood is subsequently split among various arteries, which gradually decrease in diameter and increase in total number.

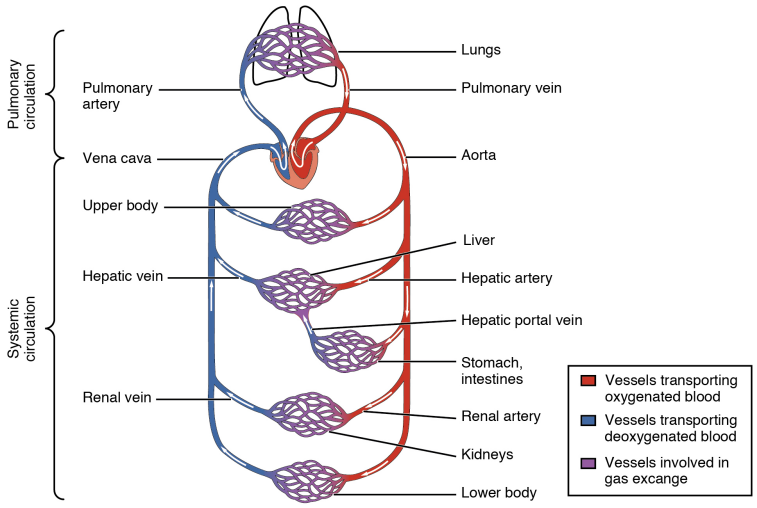

Figure 1.9. Systemic and pulmonary circulation.

This dividing and splitting mechanism results in the creation of the capillary bed, where the needed exchange of nutrients and wastes between blood and cells happens. Thereafter, blood passes from the arterial to the venous side of the systemic circulation, where it begins to merge in larger and larger venules, finally converging to the right atrium through venae cavae or the coronary sinus.

In table 1.10, a quantification of the result of splitting and merging in diameter, wall thickness, number of vessel, volume included and mean pressure is shown. In order to reach every cell compos-

Vessel	*Diameter of lumen* (mm)	*Wall thickness* (mm)	*Number of vessels*	*Blood volume* (%)	*Mean pressure* (kPa)
Aorta	25	2	1	2	12.5
Large arteries	1–10	1	50	5	12
Small arteries	.5–1	1	10^3	5	12
Arteriole	.01–.5	0.03	10^4	5	7
Capillary	.006–.01	0.001	10^6	5	3
Venule	.01–.5	0.003	10^4	25	1.5
Vein	.5–15	0.5	10^3	50	1
Vena cava	30	1.5	2	3	0.5

Figure 1.10. Geometrical and pressure characteristics of systemic circulation (After Caro *et al*[26])

ing the human body, the arterial network is organized to have a increase on number, cross sectional area and volume through the bifurcation. In an opposite way, the merging venous network decrease the overall cross sectional area in the direction of the flow.

Arteries As briefly introduced in the precedent Subsection, the arteries form an elastic bifurcating network, normally called arterial tree. The biggest artery of the network is the aorta, from which the other large arteries are originated by subsequent bifurcation.

Arteries are very complex deformable vessels. The arterial wall displays a location-dependent anisotropic non-linear viscoelastic behaviour[80;121;193]. The main components of the arterial wall are the fibrous elastic interlocked elastin and collagen and the active smooth muscle[121].

The local dependence of the mechanical properties should be understood from the arteries different functions. The large elastic central arteries serve predominantly as a cushioning reservoir. The long muscular arteries act principally as a conduits, distributing blood to the periphery; these arteries also actively modify wave propagation by changing smooth muscle tone. The arterioles, by changing their calibre, alter peripheral resistance with the aim to maintain the mean arterial pressure[121]. Starting from the central arteries and moving to more peripheral vessels there is a reduction in relative importance of the elastic components (elastin end collagen) in favour of the active behaviour of the smooth muscle component. The difference in mechanical response is thus due to changes in relative constituents compositions. It is important to point out that there is also a pure geometrical reason. Indeed, Laplace law states that the circumferential stress on a cylinder T_θ can be written as

$$T_\theta = r\Delta P \tag{1.1}$$

where r is the radius and ΔP is the pressure difference across the wall. Consequently, the bigger is an artery the bigger is the stress on the wall for a given transmural pressure, i.e. the pressure difference across the vessel wall. Therefore, for a given arterial wall mechanical property, the bigger is an artery the more is deformable.

The non-linearity of the arterial wall mechanical properties

comes from the progressive recruitment of stiffer collagen fibres as circumferential strain increases, thus manifesting an increase in stiffness with strain intensity [193]. Starting from a non-stressed condition and slowly augmenting stress state, load passes from being charged mainly on the more deformable elastin fibre to be sustained from collagen component. This arrangement provides a safety net to prevent vessel excessive deformation at high transmural pressures [121].

Arterial wall viscosity, by smoothing high-frequency pressure component, contributes to preservation of the mechanical integrity of arterial structures [182]. It has been shown that vessels with compromised high-frequency filter capacity are more prone to vascular disease [7]. Viscous properties are mainly attributed to smooth-muscles cells [7] and to an amorphous substance formed of mucoprotein that suspends elastin and collagen fibres [121]. According to the numerical results obtained by Reymond and co-workers [145], arterial wall viscosity has been estimated to be responsible from 1.5 to 2.4 per cent on the obtained pressure behaviour.

Blood pressure within systemic circulation is obtained by the sum of three different components: atmospheric, hydrostatic and dynamic. The former represent reference pressure, conventionally defined as the pressure measured in the right atrium in conditions of muscle relaxation. Hydrostatic pressure is due to the height of the point considered with respect to the reference point, normally assumed coincident with the left ventricle. This value represents the difference in pressure generated by the column of blood interposed between measuring point and the heart. Finally, the dynamic component is generated by left ventricular ejection, and it is responsible for blood motion.

A fundamental role in arterial regulation and functioning is played by the transmural pressure, i.e. the pressure difference across arterial walls. Since the external value is approximately the atmospheric pressure, transmural pressure coincides with the sum of the dynamic component and of the hydrostatic. Transmural pressure, along with gradient of blood particle concentration, has a fundamental importance in the exchange across arterial walls.

In figure 1.11 and in table 1.10, the pressure trend within different kind of vessels is represented. Pressure range dramatically changes along the arterial tree, from being highly variable into the

left ventricle, were minimum pressure around 5 mmHg, to an almost invariable pressure of few mmHg into microcirculation.

From figure 1.11 is clearly visible as into large arteries the mean pressure is fairly conserved, while maximum systolic values underneath a progressive increase due to what is called pulse pressure amplification. However, further moving in the apparatus average pressure strongly decreases because of increased viscous losses, while fluctuation are reduced thanks to arterial capacitive function. Indeed, thanks to their elastic character, large conduit ar-

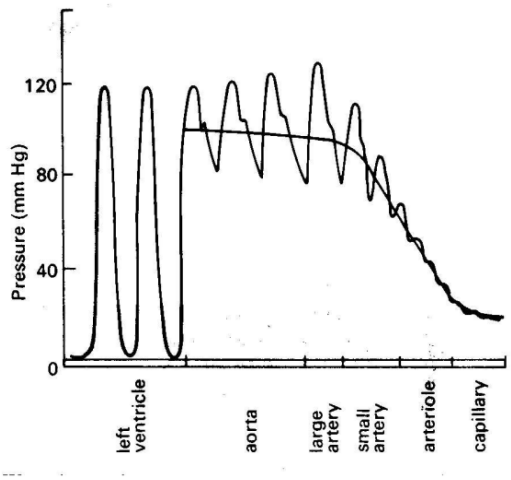

Figure 1.11. Distribution of classical value of time-varying pressure inside the arterial network (Reproduced from Caro *et al*[26])

teries function as a reservoir, accumulating blood during systolic phase, when the heart enters large quantities of fluid through the network. During diastolic phase dynamic pressure falls, flow rate is reduced and the elastic energy accumulated in the arterial wall during systole is transmitted to blood, pushing it through microcirculation. The elasticity of large arteries, accumulating energy and blood during high energy and flow periods, and subsequently releasing both in low-energy and no-flow phase, has thus a fundamental homogenizing role.

As in every non-rigid medium, pressure wave propagates with a finite celerity inside the cardiovascular system. In particular, a

local change on pressure will move in every direction at a celerity proportional to the stiffness of the medium in that direction. Since arteries are characterized by a preponderance of longitudinal direction, an analysis of the propagations through the radial direction will not be discussed. In figure 1.12 the classical behaviour of pressure pulse when propagates in the aorta is shown.

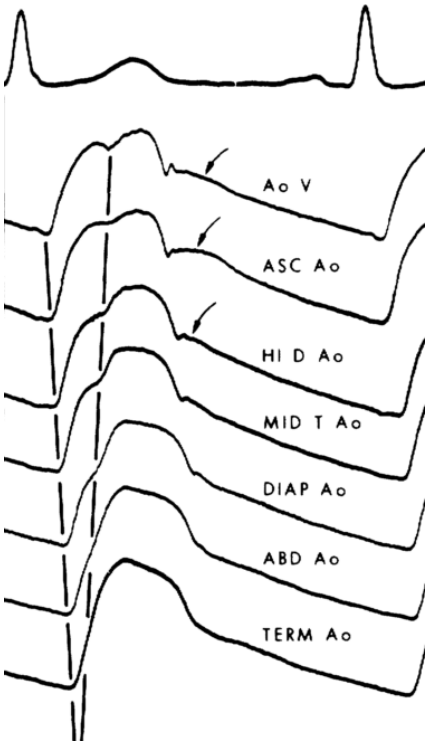

Figure 1.12. Simultaneous invasive pressure measurement in human at aortic valve (Ao V), ascending aorta (ASC Ao), high descending aorta (HI D Ao), mid thoracic aorta (MID T Ao), aorta at the level of diaphragm (DIAP Ao), abdominal aorta (ABD Ao) and terminal aorta (TERM Ao) along with the corresponding ECG signal. (Adapted from Murgo *et al*[115])

Analysing this figure several important feature of wave propagation inside large arteries can be deduced. Firstly, the finite celerity of propagation is highlighted by the inclination of the first line connecting the foot of the waves. Furthermore, distinct pressure shapes at different locations demonstrates an evolution of the

wave when travelling. In particular, one can appreciate both an increased pulse pressure and the existence of backward propagating pressure waves, here further underlined by a second line. Finally, the smoothing of the dicrotic notch (i.e. a rapid pressure elevation due to inertial effect of backward moving blood mass when aortic valve closes) can highlight the viscous dissipations.

Locally, pressure wave passage is accompanied by a radial expansion-contraction of the vessel wall. The fact that pressure and deformation waves are almost in phase suggests a predominantly elastic behaviour of the vessel wall, which partly justifies the adoption (often followed by researchers) of a linear elastic model for mechanical characterization of arterial walls[134].

Similar conclusion about pressure wave propagation can be draft from figure 1.13, where also velocity waves are presented. Both the increased pulse pressure and the increased pressure front

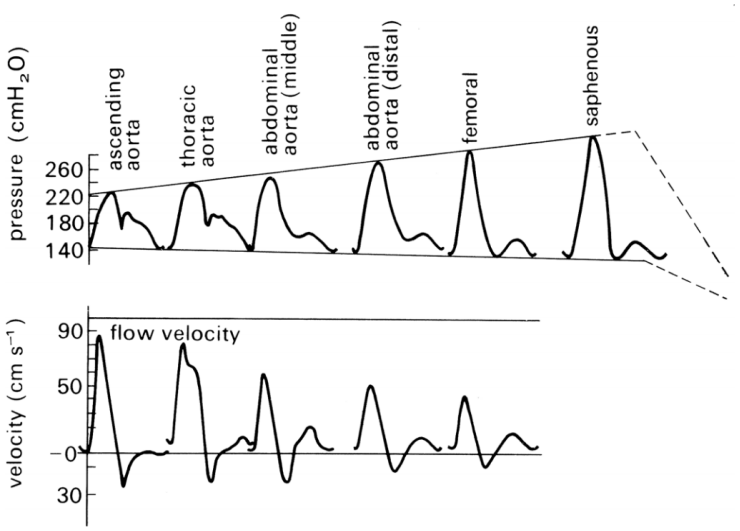

Figure 1.13. Simultaneous invasive pressure measurement in dog at different location along with the corresponding velocity waves. (From McDonald (1974). *Blood Flow in Arteries*. Edward Arnold, London.))

steepness are visible.

We here report a brief comment on velocity field. Firstly, in the early aorta velocity presents a preponderant period of direct

motion, which begins at the aortic valve opening, and where flow speed increases rapidly to a peak. This is followed by a short retrograde motion followed by a large resting phase. At rest, the duration of the direct motion occupies from a quarter to a third of the heart period but, as the frequency increases, it may reach values close to half. Progressing into circulation, the aforementioned function of hydraulic storage of large arteries implies a regularization of the velocity waveform, which mainly consists in a reduction of the velocity peak in favour of a more sustained second peak.

Veins Venous system originates in the capillary networks and ends in the right atrium. Although it is characterized by several morphological similarities with arterial system, venous system has significant differences. Firstly, veins are bigger, so that they contain about eighty percent of total blood volume, while their walls are thinner and more deformable relative to arteries. Furthermore, venous pressure is significantly lower than the arterial one, and often, also in physiological conditions, it is lower than atmospheric value. Indeed, venous blood pressure drops near the heart to values of up to 0.6 kPa; a value much lower than 13.3 kPa which is considered average in large arteries. This low pressure implies partial collapse of venous vessels due to the onset of negative transmural pressures, especially in sections placed at heights exceeding the heart one. Consequently, sections lose their characteristic circularity and undergo a strong reduction of the lumen. As can be seen in the figure 1.14 when the circular shape becomes unstable collapse proceeds through a series of states corresponding to certain transmural pressures. In the initial phase of collapse section remains cylindrical and there is just a gradual reduction in diameter due to fibre elasticity. With a further reduction on trasmural pressure, however, area divides in two almost-circular channels, separated by a completely-collapsed flattened portion, resulting in a large decrease in cross-section. In the left box of figure 1.14 a quantitative trend of vessel cross-sectional area is shown as a function of a measure of trasmural pressure (α), highlighting the strong non-linearity of the deformation law.

Since dynamic pressure, which is responsible for arterial blood motion, is greatly attenuated in the passage of blood through capillary bed, there is not enough pressure gradient for guarantee blood

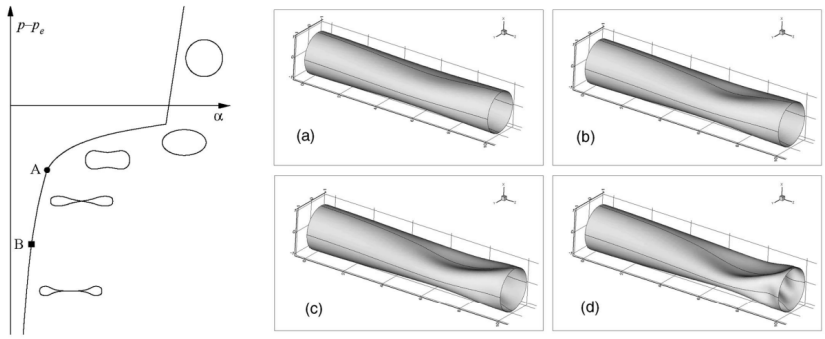

Figure 1.14. Left: representation of the deformation law (transmural pressure-area) for a flexible conduit with sketches of typical cross-sections; Right: numerical results of a vessel collapse consequent of a transmural pressure reduction (from a to d) (From Grotberg *et al*[67]).

return to the heart against gravitational forces. Venous blood motion to the heart is thus obtained with a series of distinct processes. The most important force acting on venous blood is represented by surrounding muscles contraction, which compresses until collapse large veins, moving the contained blood. A crucial role is also played by a series of unidirectional valve, especially present in the medium to large calibre vessels, typically constituted by two cusps of connective tissue containing elastin. Another positive force is obtained by respiratory cycle, which reduces thoracic internal pressure during exhalation imposing a suction through venous system. On the opposite side, gravitation acceleration and backward pressure wave due to right atrium contraction are common opposite forces acting on venous blood return.

Microcirculation Microcirculation is formed by millions of small vessels which separate the arterial from the venous side, and it is where the exchange of nutrients and cell excreta takes place. In order to reach every single cell, large arteries generally branch from six to eight times before vessels become small enough to be called arterioles, which generally have internal diameters of only 10 to 15 micrometers[70]. Then, arterioles themselves branch two to five times, reaching diameters of 5 to 9 micrometers at their

ends where they supply blood to capillaries[70]. At this stage, the exchange can take place. Subsequently, blood flows from capillaries into venules, where is further recollected into the veins. In figure 1.15 a sketch of the mesenteric capillary bed is proposed. By means of their smooth-muscle coat and their good innervation,

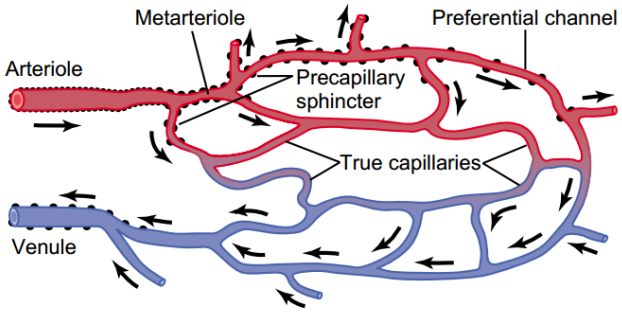

Figure 1.15. Sketch of the mesenteric capillary bed (From Zweifach BW: Factors Regulating Blood Pressure. New York: Josiah Macy, Jr., Foundation, 1950.

arterioles can change their diameter manifold[70], accomplishing to the task of regulate flow through each specific capillary bed, thus controlling effective tissue perfusion. Such a complex phenomena is usually called vasomotion and has important implication on central pressure, ventricular work and overall cardiovascular functioning. In order to preserve and regulate perfusion at different systemic pressure and condition, arteriolar smooth-muscle contraction depends on sympathetic nervous condition, tissue metabolism, vessel distension and activation state of circulating hormones and other plasma constituents in a very elaborate and efficient way.

Differently, capillary walls do not present muscle fibers, being constituted by a single layer of flat endothelial cells. According to their structure and location, capillaries can be divided in continuous, fenestrated and sinusoidal (see figure 1.16). The former, which are present in muscles and nervous and connective tissues, allow only very small molecule to pass through their walls. The fenestrated capillaries present small pore in the endothelial layer, allowing small protein and molecules to filter. These capillary are usually encountered in pancreas, intestines and part of the kidney. Differently, even red and white cell pass through the sinusoidal

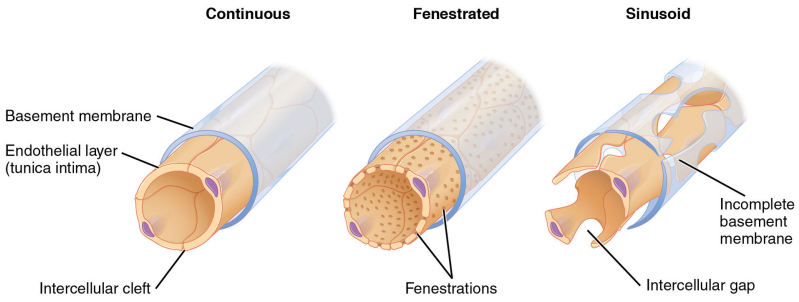

Figure 1.16. Three major capillary types.

capillary openings.

At capillary level, the great majority of substances exchange is obtained by means of molecular diffusion through capillary membrane. Other exchange methods rely on direct blood filtration through capillary wall or in a mechanism called transcytosis.

Once blood has exchanged nutrient and oxygen with waste products and carbon dioxide it is conveyed in a venule, and the path through venous network starts.

1.4 Pulmonary circulation

Pulmonary circulation is the combination of vessels that carry blood from the right ventricle through pulmonary alveoli of the lungs and back to the left atrium (see figure 1.9).

Although flow through the pulmonary arteries is comparable to that of the aorta, such a network provides a much smaller overall resistance. Consequently, pressure is much lower, and the right heart is weaker and thinner than its left counterpart.

Chapter 2

Mathematical modelling

The analysis of the motion of a fluid subjected to a variable pressure in a network of deformable vessels is important in many engineering and medical applications. Despite the large amount of research produced by a wide range of scholars, from physicists to mathematicians and engineers, the exact solution of the flow field is not yet available. By examining the real situation of this motion the reasons why the problem is so complicated can be understood. Since the aim of this Section is introduce the reader to the mathematical modelling of the cardiovascular system, we would consider blood as fluid, and arteries as containing vessels.

The first difficulty in modelling blood motion within the systemic circulation is found by analysing blood rheological properties. Indeed, as introduced in the precedent Chapter, blood is not a perfect liquid, being formed by the viscous plasma where several deformable particles are suspended. A correct rheological mathematical model should thus consider the interaction between the suspended particles, their deformation and the consequent overall non-Newtonian behaviour. Another strong difficulty arises from the implementation of the arterial wall mechanical properties and of their complex structure. Arterial walls are formed by several different living layers that globally results in a location-dependent anisotropic non-linear viscoelastic behaviour[80;121;193]. It is easy to understand how a mechanical model that considers the different layers, their large deformations, their compositions and their mutual living interactions would be very complex. Furthermore, such

a description should be able to enters in a fluid dynamic mathematical model, which often impose important restrictions. On the other side, left-ventricular ejection is intermittent and the connection between this pumping volume and the receiving network is mediated by the aortic valve, a marvellous passive viscoelastic moving structure whose motion is very complex. The flow into the large arteries is strongly pulsatile. Consequently, the pressure and flow patter is time- and location-dependent and flow and pressure pulse underneath important changes when moving within the network. Fortunately, the flow field is most of time laminar, although laminar-turbulent transition happens close to the most complicated geometries such as the heart valve. Finally, the network is itself complex, as introduced in the apposite Section. Large arteries bifurcate several times, greatly increasing in number and reducing their calibre through the arterial tree. Bifurcations can be very different, ranging form cases where one branch can be considered lateral and minor, to conditions where the incoming artery is split in two similar arteries. Moreover, arteries are often curved, and important secondary flow fields are known to arise. Considering that every artery is itself a very complex entity, the interaction between their network become impossible to solve.

Recognizing all these characteristics one can understand how the resulting system of equation, forming the mathematical model, would be highly non-linear and complex. Additionally, it is important to point out that a detailed description of all these characteristic would require an elevated number of information, which often are not available.

Consequently, a significant number of simplifying assumption have been adopted in order to allow the resolution of the model. With the progress of technology, however, the increase of knowledge and computing capacity has allowed a gradual reduction of the assumptions needed, allowing a wide range of gradually more complex mathematical models to be created.

Indeed, as introduced at the beginning of this Thesis, the physically-based modelling of the cardiovascular system has a long history and the successive refinements have been impressive[183]. In the next Sections two different mathematical models will be presented. Although the descriptions of some subsystem are identical, crucial differences exist. The first model presented is a lumped model of

the complete cardiovascular system, while the second is a multi-scale (1D/0D) model of the left ventricle-arterial interaction with one-dimensional description of the arterial tree. The former, exploiting electrical analogy, allows to describe the fluid-mechanical behaviour by means of a set of ordinary differential equations. Differently, multi-scale modelling results in a set of partial differential equations, where the spatio-temporal propagations are considered. By the way, left-ventricle and aortic valve are modelled in the same way, and important assumptions are shared by the models.

2.1 Lumped model

The present lumped model, proposed by Korakianitis and Shi[89], extends the Windkessel approach[131;193] and consists of a network of capacitors, resistances and inductances describing the pumping heart coupled to the systemic and pulmonary systems. Viscous effects are taken into account by resistances, R [mmHg s/ml], inertial terms are considered by inductances, L [mmHg s^2/ml], while vessel elastic properties are described by capacitors, C [ml/mmHg]. Three cardiovascular variables are involved at each section: blood flow, Q [ml/s], volume, V [ml] and pressure, P [mmHg]. A schematic representation of the cardiovascular system is shown in Fig. 2.1.

All four chambers forming the heart are described. Cardiac pulsatility properties are included by means of two pairs of time-varying elastance functions, one for atria and one for ventricles, which are then used in the constitutive equations, relating pressure and volume). For the four heart valves, the basic pressure-flow relation is described by an orifice model. Valve motion mechanisms are deeply analysed, accounting for the following blood-flow effects: pressure difference across the valve, frictional effects from tissue resistance, dynamic motion effect of blood acting on valve leaflets and the action of the vortex downstream of the valve. The introduction of a time-varying elastance for atria accounts for their contraction, while heart dynamics description allows to model valvular regurgitation and dicrotic notch mechanism. An equation for the mass conservation (accounting for the volume variation, dV/dt) concludes the description of each chamber.

Systemic and pulmonary systems are divided into 5 parts (see

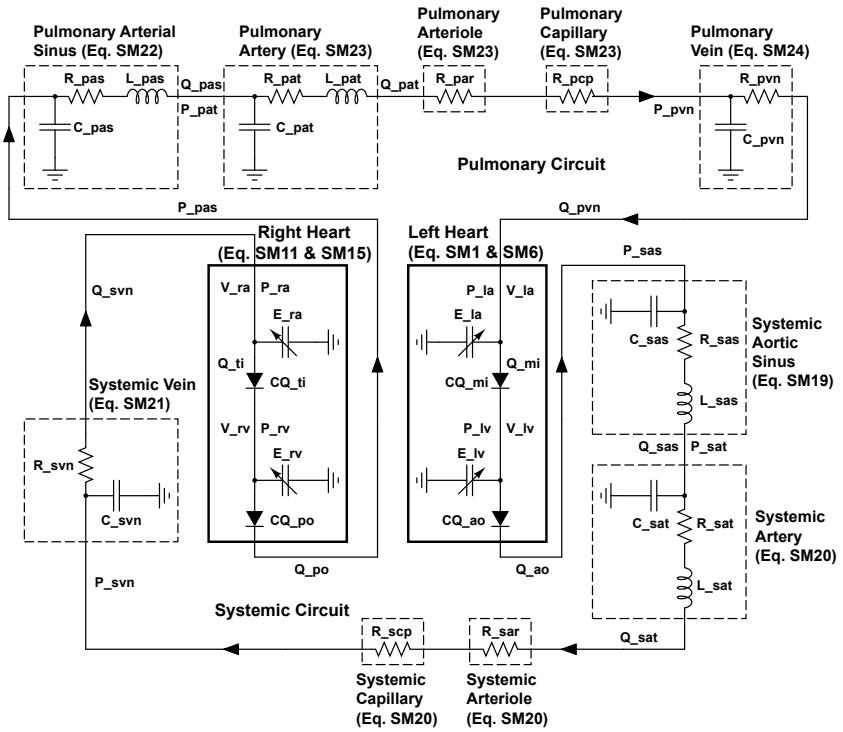

Figure 2.1. Scheme of the model: blood flow Q, volume V, pressure P. Subscripts *sas*, *sat*, *sar*, *scp* and *svn* refer to aortic sinus, and systemic arteries, arterioles, capillaries and veins. *ra*, *rv*, *la* and *lv* indicate right atrium, right ventricle, left atrium and left ventricle. *pas*, *pat*, *par*, *pcp* and *pvn* specify pulmonary arterial sinus, arteries, arterioles, capillary and veins.

Fig. 2.1). Systemic circulation is split in four interacting subsystems (aortic sinus, artery, arteriole and capillary), while systemic venous circulation is characterized by a unique compartment. Similarly division is used for pulmonary circuit. Each section of the systemic and pulmonary circuits may contain three components (viscous, R, inertial, L, and elastic, C term), and is characterized by three equations: an equation of motion (accounting for flow variation, dQ/dt), an equation for mass conservation (expressed in terms of pressure variations, dP/dt), and a linear state equation between pressure and volume.

The resulting differential system is numerically solved by means

of a multistep adaptative scheme based on the numerical differentiation formulas (NDFs).

2.1.1 Governing equations

In this Section the governing equation are presented. For the sake of simplicity, equations are grouped into cardiac (with the four chambers) and circulatory (with systemic and pulmonary loops) sections.

Cardiac

As introduced, all cardiac chambers are here modelled. We here report their governing equations.

Left Atrium
The following equations describe left atrium behaviour, relating left atrial volume V_{la} and pressure P_{la} and inflow Q_{pvn} and outflow Q_{mi} as

$$\begin{aligned} \frac{dV_{la}}{dt} &= Q_{pvn} - Q_{mi}, \\ P_{la} &= P_{la,un} + E_{la}(V_{la} - V_{la,un}), \\ Q_{mi} &= \begin{cases} CQ_{mi}\Theta_{mi}\sqrt{P_{la} - P_{lv}}, & \text{if } P_{la} \geq P_{lv}, \\ -CQ_{mi}\Theta_{mi}\sqrt{P_{lv} - P_{la}}, & \text{if } P_{la} < P_{lv}, \end{cases} \end{aligned} \tag{2.1}$$

where the subscript un denotes the unstressed pressure and volume levels of each cardiovascular section, CQ is a flow coefficient and Θ is a function which simulates the non-ideal behaviour of the valve orifice. The time-varying elastance governs the left atrial activation, and it is written as

$$E_{la}(t) = E_{la,min} + \frac{E_{la,max} - E_{la,min}}{2} e_a(t), \tag{2.2}$$

where the atrium activation function $e_a(t)$ is

$$e_a(t) = \begin{cases} 0, & \text{if } 0 \leq t \leq T_{ac}, \\ 1 - \cos\left(\frac{t - T_{ac}}{RR - T_{ac}} 2\pi\right), & \text{if } T_{ac} < RR, \end{cases} \tag{2.3}$$

and where $E_{la,min}$ and $E_{la,max}$ are the minimum and maximum elastance values, respectively, while T_{ac} is time at the beginning of atrial contraction.

The non-binary state of the mitral valve opening is quantified from the angular position of the leaflets as

$$\Theta_{mi} = \frac{(1-\cos\theta_{mi})^2}{(1-\cos\theta_{max})^2}. \tag{2.4}$$

The valve opening angle is obtained solving the following balance of force acting on the leaflets

$$\frac{d^2\theta_{mi}}{dt^2} = \begin{cases} (P_{la}-P_{lv})K_{p,mi}\cos\theta_{mi} - K_{f,mi}\frac{d\theta_{mi}}{dt} \\ \quad +K_{b,mi}Q_{mi}\cos\theta_{mi} \\ \quad -K_{v,mi}Q_{mi}\sin 2\theta_{mi}, \quad \text{if } Q_{mi}\geq 0, \\ (P_{la}-P_{lv})K_{p,mi}\cos\theta_{mi} - K_{f,mi}\frac{d\theta_{mi}}{dt} \\ \quad +K_{b,mi}Q_{mi}\cos\theta_{mi}, \quad \text{if } Q_{mi}<0, \end{cases} \tag{2.5}$$

where the coefficients $K_{p,mi}, K_{f,mi}, K_{b,mi}$ and $K_{v,mi}$ have been selected by Korakianitis *et al*[89] by means of numerical experiments in order to produce physiological valve motion process as described in the literature.

Left Ventricle

Similarly, left ventricle mathematical description results in the following ordinary differential equations.

$$\begin{aligned} \frac{dV_{lv}}{dt} &= Q_{mi} - Q_{ao}, \\ P_{lv} &= P_{lv,un} + E_{lv}(V_{lv} - V_{lv,un}), \\ Q_{ao} &= \begin{cases} CQ_{ao}\Theta_{ao}\sqrt{P_{lv}-P_{sas}}, & \text{if } P_{lv}\geq P_{sas}, \\ -CQ_{ao}\Theta_{ao}\sqrt{P_{sas}-P_{lv}}, & \text{if } P_{sas}<P_{lv}, \end{cases} \end{aligned} \tag{2.6}$$

where inflow Q_{mi} comes from mitral valve while the outflow Q_{ao} is the ejection through the aortic valve.

The time-varying elastance is written as

$$E_{lv}(t) = E_{lv,min} + \frac{E_{lv,max}-E_{lv,min}}{2}e_v(t), \tag{2.7}$$

and the ventricle activation function is

$$e_v(t) = \begin{cases} 1-\cos\left(\frac{t}{T_{me}}\pi\right), & \text{if } 0 \le t < T_{me}, \\ 1+\cos\left(\frac{t-T_{me}}{T_{ce}-T_{me}}\pi\right), & \text{if } T_{me} \le t < T_{ce} \\ 0, & \text{if } T_{ce} \le t < RR, \end{cases} \tag{2.8}$$

where $E_{lv,min}$ and $E_{lv,max}$ are minimum and maximum elastance values, respectively. T_{me} and T_{ce} are the instants where elastance reaches its maximum and constant values, respectively.

The valve opening function is decided by the angular position of the leaflets:

$$\Theta_{ao} = \frac{(1-\cos\theta_{ao})^2}{(1-\cos\theta_{max})^2} \tag{2.9}$$

while aortic valve motion is governed by the following system of ordinary differential equations

$$\frac{d^2\theta_{ao}}{dt^2} = \begin{cases} (P_{lv}-P_{sas})K_{p,ao}\cos\theta_{ao} - K_{f,ao}\frac{d\theta_{ao}}{dt} \\ \quad +K_{b,ao}Q_{ao}\cos\theta_{ao} \\ \quad -K_{v,ao}Q_{ao}\sin 2\theta_{ao}, \quad \text{if } Q_{ao} \ge 0, \\ (P_{lv}-P_{sas})K_{p,ao}\cos\theta_{ao} - K_{f,ao}\frac{d\theta_{ao}}{dt} \\ \quad +K_{b,ao}Q_{ao}\cos\theta_{ao}, \quad \text{if } Q_{ao} < 0, \end{cases} \tag{2.10}$$

Right Atrium

Right atrium description is analogous, and results in the following system of equations.

$$\begin{aligned} \frac{dV_{ra}}{dt} &= Q_{svn} - Q_{ti}, \\ P_{ra} &= P_{ra,un} + E_{ra}(V_{ra} - V_{ra,un}), \\ Q_{ti} &= \begin{cases} CQ_{ti}\Theta_{ti}\sqrt{P_{ta}-P_{tv}}, & \text{if } P_{ta} \ge P_{tv}, \\ -CQ_{ti}\Theta_{ti}\sqrt{P_{rv}-P_{ra}}, & \text{if } P_{ra} < P_{rv}, \end{cases} \end{aligned} \tag{2.11}$$

where right atrial volume is obtained from the balance between inflow from venous system Q_{svn} and outflow through tricuspid valve Q_{ti} and where time-varying elastance is written as

$$E_{ra}(t) = E_{ra,min} + \frac{E_{ra,max} - E_{ra,min}}{2} e_a(t). \tag{2.12}$$

The activation function is given by Eq. (2.3), while $E_{ra,min}$ and $E_{ra,max}$ are the minimum and maximum elastance values, respectively.

Tricuspid valve opening coefficient is obtained from angular as

$$\Theta_{ti} = \frac{(1-\cos\theta_{ti})^2}{(1-\cos\theta_{max})^2} \tag{2.13}$$

and valve motion is governed by

$$\frac{d^2\theta_{ti}}{dt^2} = \begin{cases} (P_{ra}-P_{rv})K_{p,ti}\cos\theta_{ti} - K_{f,ti}\frac{d\theta_{ti}}{dt} \\ \quad +K_{b,ti}Q_{ti}\cos\theta_{ti} \\ \quad -K_{v,ti}Q_{ti}\sin 2\theta_{ti}, \quad \text{if } Q_{ti} \geq 0, \\ (P_{ra}-P_{rv})K_{p,ti}\cos\theta_{ti} - K_{f,ti}\frac{d\theta_{ti}}{dt} \\ \quad +K_{b,ti}Q_{ti}\cos\theta_{ti}, \quad \text{if } Q_{ti} < 0, \end{cases} \tag{2.14}$$

Right Ventricle

Finally, right ventricle description is deduced in an identical way as

$$\begin{aligned} \frac{dV_{rv}}{dt} &= Q_{ti} - Q_{po}, \\ P_{rv} &= P_{rv,un} + E_{rv}(V_{rv} - V_{rv,un}), \\ Q_{po} &= \begin{cases} CQ_{po}\Theta_{po}\sqrt{P_{rv}-P_{pas}}, & \text{if } P_{rv} \geq P_{pas}, \\ -CQ_{po}\Theta_{po}\sqrt{P_{pas}-P_{rv}}, & \text{if } P_{pas} < P_{rv}, \end{cases} \end{aligned} \tag{2.15}$$

where time-varying elastance is written as

$$E_{rv}(t) = E_{rv,min} + \frac{E_{rv,max}-E_{rv,min}}{2}e_v(t), \tag{2.16}$$

and where ventricle activation function is. Again, $E_{rv,min}$ and $E_{rv,max}$ are minimum and maximum elastance values, respectively.

The valve opening effect is computed from leaflet angular position as

$$\Theta_{po} = \frac{(1-\cos\theta_{po})^2}{(1-\cos\theta_{max})^2} \tag{2.17}$$

and valve motion is governed by

$$\frac{d^2\theta_{po}}{dt^2} = \begin{cases} (P_{rv} - P_{pas})K_{p,po}\cos\theta_{po} - K_{f,po}\frac{d\theta_{po}}{dt} \\ \quad +K_{b,po}Q_{po}\cos\theta_{po} \\ \quad -K_{v,po}Q_{po}\sin 2\theta_{po}, \quad \text{if } \ Q_{po} \geq 0, \\ (P_{rv} - P_{pas})K_{p,po}\cos\theta_{po} - K_{f,po}\frac{d\theta_{po}}{dt} \\ \quad +K_{b,po}Q_{po}\cos\theta_{po}, \quad \text{if } \ Q_{po} < 0. \end{cases} \tag{2.18}$$

Systemic Circuit

The network of large arteries that bifurcates several time resulting in a huge number of inhomogeneous small vessels is here brought together and concentrated in a punctual description. Having disregarded all the spatial informations, the set of resulting equation is composed by ordinary differential equation, and the unique independent variable is *time*.

Systemic circulation is here divided in five sectors. Aortic sinus (subscript sas), large arteries (sat), arterioles (sar), capillaries (scp) and veins (svn), which are thus independently modelled. Each sector is described by three equations and the different predominances of particular characteristic is obtained balancing parameter values. A special case is represented by the venous system, where very low acceleration entails negligible inertia. Consequently, venous inertance is totally neglected. Large arteries description are dominated by elastic behaviour while arterioles and capillaries results in a mainly resistive characteristic. A three sector description of the network is here analysed. The following systems of equations describe the systemic circuit.

$$\begin{cases} \frac{dP_{sas}}{dt} = \frac{Q_{ao} - Q_{sas}}{C_{sas}}, \\ \frac{dQ_{sas}}{dt} = \frac{P_{sas} - P_{sat} - R_{sas}Q_{sas}}{L_{sas}}, \\ P_{sas} - P_{sas,un} = \frac{1}{C_{sas}}(V_{sas} - V_{sas,un}), \end{cases} \tag{2.19}$$

$$\begin{cases} \frac{dP_{sat}}{dt} = \frac{Q_{sas} - Q_{sat}}{C_{sat}}, \\ \frac{dQ_{sat}}{dt} = \frac{P_{sat} - P_{svn} - (R_{sat} + R_{sar} + R_{scp})Q_{sat}}{L_{sat}}, \\ P_{sat} - P_{sat,un} = \frac{1}{C_{sat}}(V_{sat} - V_{sat,un}), \end{cases} \tag{2.20}$$

$$\begin{cases} \frac{dP_{svn}}{dt} = \frac{Q_{sat}-Q_{svn}}{C_{svn}}, \\ Q_{svn} = \frac{P_{svn}-P_{ra}}{R_{svn}}, \\ P_{svn} - P_{svn,un} = \frac{1}{C_{svn}}(V_{svn} - V_{svn,un}), \end{cases} \tag{2.21}$$

Pulmonary Circuit

Pulmonary circuit is modelled in a similar way. Indeed, pulmonary circulation is divided in five compartments: pulmonary arterial sinus (subscript pas), pulmonary large arteries (pat), pulmonary arterioles (par), capillary (pcp) and veins (pvn). The resulting systems of equation are written as

$$\begin{cases} \frac{dP_{pas}}{dt} = \frac{Q_{po}-Q_{pas}}{C_{pas}}, \\ \frac{dQ_{pas}}{dt} = \frac{P_{pas}-P_{pat}-R_{pas}Q_{pas}}{L_{pas}}, \\ P_{pas} - P_{pas,un} = \frac{1}{C_{pas}}(V_{pas} - V_{pas,un}) \end{cases} \tag{2.22}$$

$$\begin{cases} \frac{dP_{pat}}{dt} = \frac{Q_{pas}-Q_{pat}}{C_{pat}}, \\ \frac{dQ_{pat}}{dt} = \frac{P_{pat}-P_{pvn}-(R_{pat}+R_{par}+R_{pcp})Q_{pat}}{L_{pat}}, \\ P_{pat} - P_{pat,un} = \frac{1}{C_{pat}}(V_{pat} - V_{pat,un}), \end{cases} \tag{2.23}$$

$$\begin{cases} \frac{dP_{pvn}}{dt} = \frac{Q_{pat}-Q_{pvn}}{C_{pvn}}, \\ Q_{pvn} = \frac{P_{pvn}-P_{la}}{R_{pvn}}, \\ P_{pvn} - P_{pvn,un} = \frac{1}{C_{pvn}}(V_{pvn} - V_{pvn,un}). \end{cases} \tag{2.24}$$

2.1.2 Numerical Scheme

The system of ordinary differential equation is solved in time by means of a multistep adaptative solver for stiff problems, implemented by the `ode15s` Matlab function (MATLAB version 7.9.0 (2009) Natick, Massachusetts: The MathWorks Inc). The relative error tolerance, `RelTol`, is set equal to 10^{-10}. The absolute error tolerance, `AbsTol`, is in general imposed equal to 10^{-6}, except for equations involving aortic and pulmonary flows, Q_{ao} and Q_{po}, where a more stringent tolerance (10^{-10}) is required to avoid numerical oscillations.

The variable order solver adopted is based on the numerical differentiation formulas (NDFs) and is chosen because is one of the most efficient and suitable routines for stiff problems. In fact, the equation representing the cardiovascular system shows some stiffness features, including some terms that can lead to rapid variation in the solutions. This aspect is particularly relevant for valve dynamics, where sudden variations of leaflet angular position occur when valves open and close.

2.1.3 Initial Conditions and parameters values

Initial conditions are given in terms of pressures, volumes, flow rates and valve opening angles. The total volume is taken as the average value for a healthy adult, V_{tot}=5250 ml. Initial condition considers that all the valves are closed and no flow is present. Initial pressures in the circulatory sections are given as typical values reached during a normal cardiac cycle. Volumes in the four chambers are obtained at t=0 subtracting from the total volume, V_{tot}, all the volume contributes at the generic vascular section i, using the constitutive relation $P_{i,t=0} - P_{i,un} = \frac{1}{C_i}(V_{i,t=0} - V_{i,un})$, where $P_{i,t=0}$ is imposed as previously said. Table 2.1 summarizes the adopted initial values. Cardiovascular parameters are shown in tables from 2.2 to 2.6.

Variable	Value ($t = 0$)
$V_{la,0}$	60 ml
$V_{lv,0}$	130 ml
$V_{ra,0}$	39 ml
$V_{rv,0}$	110 ml
$P_{sas,0}$	100 mmHg
$Q_{sas,0}$	0 ml/s
$P_{sat,0}$	100 mmHg
$Q_{sat,0}$	0 ml/s
$P_{svn,0}$	10 mmHg
$P_{pas,0}$	20 mmHg
$Q_{pas,0}$	0 ml/s
$P_{pat,0}$	20 mmHg
$Q_{pat,0}$	0 ml/s
$P_{pvn,0}$	10 mmHg
$\theta_{mi,0} = d\theta_{mi,0}/dt$	0 rad
$\theta_{ao,0} = d\theta_{ao,0}/dt$	0 rad
$\theta_{ti,0} = d\theta_{ti,0}/dt$	0 rad
$\theta_{po,0} = d\theta_{po,0}/dt$	0 rad

Table 2.1. Initial conditions.

Parameter	Value
CQ_{ao}	350 ml/(s mmHg$^{0.5}$)
CQ_{mi}	400 ml/(s mmHg$^{0.5}$)
$E_{lv,max}$	2.5 mmHg/ml
$E_{lv,min}$	0.07 mmHg/ml
$P_{lv,un}$	1 mmHg
$V_{lv,un}$	5 ml
$E_{la,max}$	0.25 mmHg/ml
$E_{la,min}$	0.15 mmHg/ml
$P_{la,un}$	1 mmHg
$V_{la,un}$	4 ml
CQ_{po}	350 ml/(s mmHg$^{0.5}$)
CQ_{ti}	400 ml/(s mmHg$^{0.5}$)
$E_{rv,max}$	1.15 mmHg/ml
$E_{rv,min}$	0.07 mmHg/ml
$P_{rv,un}$	1 mmHg
$V_{rv,un}$	10 ml
$E_{ra,max}$	0.25 mmHg/ml
$E_{ra,min}$	0.15 mmHg/ml
$P_{ra,un}$	1 mmHg
$V_{ra,un}$	4 ml

Table 2.2. Heart parameters.

Parameter	Value
C_{sas}	0.08 ml/mmHg
R_{sas}	0.003 mmHg s/ml
L_{sas}	0.000062 mmHg s^2/ml
$P_{sas,un}$	1 mmHg
$V_{sas,un}$	25 ml
C_{sat}	1.6 ml/mmHg
R_{sat}	0.05 mmHg s/ml
L_{sat}	0.0017 mmHg s^2/ml
$P_{sat,un}$	1 mmHg
$V_{sat,un}$	775 ml
R_{sar}	0.5 mmHg s/ml
R_{scp}	0.52 mmHg s/ml
R_{svn}	0.075 mmHg s/ml
C_{svn}	20.5 ml/mmHg
$P_{svn,un}$	1 mmHg
$V_{svn,un}$	3000 ml

Table 2.3. Systemic circulation parameters.

Parameter	Value
C_{pas}	0.18 ml/mmHg
R_{pas}	0.002 mmHg s/ml
L_{pas}	0.000052 mmHg s^2/ml
$P_{pas,un}$	1 mmHg
$V_{pas,un}$	25 ml
C_{pat}	3.8 ml/mmHg
R_{pat}	0.01 mmHg s/ml
L_{pat}	0.0017 mmHg s^2/ml
$P_{pat,un}$	1 mmHg
$V_{pat,un}$	175 ml
R_{par}	0.05 mmHg s/ml
R_{pcp}	0.07 mmHg s/ml
R_{pvn}	0.006 mmHg s/ml
C_{pvn}	20.5 ml/mmHg
$P_{pvn,un}$	1 mmHg
$V_{pvn,un}$	300 ml

Table 2.4. Pulmonary circulation parameters.

Parameter	Value
$K_{p,mi}$, $K_{p,ao}$, $K_{p,ti}$, $K_{p,po}$	5500 ml/mmHg
$K_{f,mi}$, $K_{f,ao}$, $K_{f,ti}$, $K_{f,po}$	50 s^{-1}
$K_{b,mi}$, $K_{b,ao}$, $K_{b,ti}$, $K_{b,po}$	2 rad/(s ml)
$K_{v,mi}$, $K_{v,ti}$	3.5 rad/(s ml)
$K_{v,ao}$, $K_{v,po}$	7 rad/(s ml)
θ_{max}	5/12 π rad

Table 2.5. Valve dynamics parameters.

Parameter	Value
T_{ac}	0.875 RR s
T_{me}	0.3 $\sqrt{RR}$ s
T_{ce}	3/2 T_{me} s

Table 2.6. Temporal parameters. Activation times are those typically introduced in the time-varying elastance models[89;131], and are here settled considering that, at RR=0.8 s, the ventricular systole lasts about 0.3 s, while the atrial systole length is about 0.1 s[70].

2.2 Multi-scale model

In current literature the effectiveness of the multi-scale mathematical approach for the description of the cardiovascular system has been recognized[17;100;163]. Consisting in coupling of submodels of different dimensions, multi-scale modelling allows to evaluate the interactions of different sectors, each of them described with the most suitable level of detail. Indeed, left ventricle, its bounding valves, large arteries and microcirculation volumes are described independently, although then solved together.

With the aim of obtaining an optimal balance among computational efforts, required data and results, one-dimensional description of large arteries has been adopted by the majority of authors[2;15;17;56;100;122;124;125;139;140;144;171], while three-dimensional (3D) models are usually limited to detailed descriptions of local vascular conditions[17;18], although very recently a full scale 3D model has been proposed[200]. Several studies concerned the mechanical description of the arterial walls, namely the so-called constitutive relation, that associates stress and deformation. Even though the arterial wall tissues display a complex non-linear viscoelastic behaviour[77;80;193], several simplified constitutive laws have been adopted. They range from the linear elastic description[15;56;125] to more complex linear[2;8;14;55] or non-linear[17;145] viscoelastic characterizations.

For what concern heart modelling, the lumped description introduced by Sagawa[155] has been largely successful, being time-varying elastance able to accurately reproduce the main features of the contracting myocardium[17;89;100;145;163]. Finally, in spite of the key role of aortic valve in the heart-arterial coupling, just a few authors introduced a physically-based description of aortic valve leaflet movement in their models[89;116]. Valves are in fact generally approximated as an ideal diode plus a resistance, thus ignoring important dynamical features[163].

Microcirculation fluid mechanics is by far too complex for being described with similar fully-non linear system of continuous equations. Indeed, micro-circulation networks have been modelled as

regular fractal networks[125], where non-linear terms have been disregarded, or by a zero-dimensional approach, using three-elements Windkessel models[193], thus avoiding spatial discretization.

Venous return has received less attention, mainly due to the fluid dynamic complexity of such collapsible conduits; however, some lumped[17;19] and one-dimensional models[113] have been proposed.

In the next Section we present a multi-scale (1D/0D) model of the left ventricular-arterial interaction. Large artery are described with fully-non linear one dimensional Navier-Stokes equation, where non-linear viscoelastic mechanical properties of the containing vessels are considered. Left ventricular dynamics are modelled by means of time-varying elastance function. Aortic valve motion is obtained from balance of force acting on its leaflet, while mitral valve is assumed ideal. Finally, Windkessel description of small-vessel network is used.

2.2.1 Hydraulics of the large arteries

One dimensional description of large arterial blood flow assumes that vessel geometry and flow field are axisymmetric and flow is laminar[93]. Arterial walls are considered impermeable and longitudinally tethered. A small vessel radius-to-length ratio is assumed [125] and vessel deformations are small and only radial. Therefore, deformed sections remain perpendicular to the axial direction and vessels maintain constant length[56]. Effects of suspended particles are neglected and blood is assumed Newtonian, incompressible and characterized by constant density, ρ, and kinematic viscosity, ν[122].

Under these assumptions, the mass and momentum balance equations integrated over the transversal section are

$$\frac{\partial A}{\partial t} + \frac{\partial Q}{\partial x} = 0 \tag{2.25}$$

$$\frac{\partial Q}{\partial t} + \frac{\partial}{\partial x}\Big(2\pi \int_0^R u^2 r dr\Big) = -\frac{A}{\rho}\frac{\partial P}{\partial x} + Ag\sin\gamma + 2\pi\nu\Big[r\frac{\partial u}{\partial r}\Big]_{r=R} \tag{2.26}$$

where x and r are the axial and radial coordinates, respectively, t is time, A is the vessel cross-sectional area, P is the radially-constant pressure, $Q = 2\pi \int_0^R urdr$ is the flow rate (R the vessel radius and

$u = u(r)$ the axial velocity profile), g is the gravitational acceleration, and γ is the angle between axial and horizontal directions.

In order to compute the convective and viscous terms of equation (2.26) a velocity profile has to be assumed. Left-ventricular periodic ejection imposes a pulsating flow throughout the arterial tree, making the velocity profile time-variable both in shape and in its mean value. This entails that flow and wall shear stresses are not in phase[15], the core flow being mainly subjected to inertial forces while the outermost part being mainly influenced by viscous forces. The diameter reduction from the large central arteries to the small arterioles determines a spatial dependence of the importance of the viscous boundary layer with respect to the central, almost flat, portion of profile. Lighthill[101] suggested that the boundary layer thickness remains almost constant along the arterial tree, thus playing a marginal role in large arteries but becoming comparable to the arterial radius in more distal and small vessels. A first-order estimate of the boundary layer thickness, $\tilde{\delta}$, is given from the equilibrium between inertial and viscous forces at the interface between viscous layer and inviscid core. It gives $\tilde{\delta} = \sqrt{\nu/\omega} \approx 1$ mm, where $\omega = 2\pi/T$ being T the cardiac period.

To date, several velocity profiles have been proposed[183]. Commonly, flat profile[56;171], various parabolic forms[2;8;17;33;105] and a profile joining a linear viscous layer and a flat inviscid core[124] are commonly adopted. In all these cases, velocity profile depends only on the flow. Differently, Bessems *et al*[15] proposed a flow field depending also on the spatial derivative of pressure, while Reymond *et al.*[145] implemented a velocity profile obtained from the Womersley theory.

Aiming at a good balance between physiological likelihood and computational complexity, we propose a new velocity distribution by assuming a central flat profile joined to a parabolic boundary layer of thickness δ. The local velocity $u(r, x, t)$ takes the form

$$u(r,x,t) = \begin{cases} \tilde{u}(x,t) & \text{if } 0 < r < R(x,t) - \delta(x,t) \\ \frac{R(x,t)^2 - r^2}{2R(x,t)\delta(x,t) - \delta(x,t)^2}\tilde{u}(x,t) & \text{if } r \geq R(x,t) - \delta(x,t) \end{cases} \tag{2.27}$$

where $\delta(x,t) = \tilde{\delta}$ if $\tilde{\delta} < R(x,t)$ and $\delta(x,t) = R(x,t)$ otherwise. Since cross-sectional integral of velocity profile must equals flow, the local velocity of the flat core $\tilde{u}(x,t)$ is related to arterial flow and radius

as

$$\tilde{u}(x,t) = \frac{2Q(x,t)}{\pi(\delta(x,t)^2 + 2R(x,t)(R(x,t) - \delta(x,t)))}.$$

Using profile (2.27), the convective term of equation (2.26) can be written as

$$\frac{\partial}{\partial x}\Big(2\pi \int_0^R u^2 r dr\Big) = \frac{\partial}{\partial x}\Big(\beta \frac{Q^2}{A}\Big) \tag{2.28}$$

where β is the Coriolis coefficient (or momentum correction factor) computed as

$$\beta(x,t) = \frac{4}{3}\frac{3A^2 - 4A^{3/2}\sqrt{\pi}\delta + 2A\pi\delta^2}{(2A - 2\sqrt{A}\sqrt{\pi}\delta + \pi\delta^2)^2}. \tag{2.29}$$

In the limit $\delta/R(x) \to 0$ typical of the large arteries $\beta = 1$, while in the small vessels (where $\delta = R$) $\beta = 4/3$ as in the Poseuille flow.

The viscous drag force term becomes

$$2\pi\nu\Big[r\frac{\partial u}{\partial r}\Big]_R = \frac{8AQ\sqrt{\pi}\nu}{\delta(-4A^{3/2} + 6A\sqrt{\pi}\delta - 4\sqrt{A}\pi\delta^2 + \pi^{3/2}\delta^3)} = N_4(x,t). \tag{2.30}$$

and, accordingly, equation (2.26) becomes

$$\frac{\partial Q}{\partial t} + \frac{\partial}{\partial x}\left(\beta\frac{Q^2}{A}\right) = -\frac{A}{\rho}\frac{\partial P}{\partial x} + Ag\sin\gamma + N_4. \tag{2.31}$$

2.2.2 Constitutive relation

Equations (2.25) and (2.31) contain three dependent variables, namely $P(x,t)$, $Q(x,t)$ and $A(x,t)$, so a third equation is needed. By linking pressure and area, the constitutive relation quantifies wall deformation induced by a change of pressure. We choose $Q(x,t)$ and $A(x,t)$ as dependent variables because the corresponding differential system results more suitable to be numerically simulated by Discontinuous Galerkin method; moreover, 1D models are generally written in the domain $\{Q, A\}$. It follows that pressure has to be written as a function of the vessel area.

The arterial wall exhibits a vessel-dependent anisotropic nonlinear viscoelastic behaviour, due to the complex interplay among the fibrous elastic interlocked elastin, collagen, and active smooth muscles[80;121;182;193]. The mechanical properties depend on artery

function: large elastic central arteries serve predominantly as a cushioning reservoir, long muscular arteries actively modify wave propagation by changing smooth muscle tone, and arterioles alter the peripheral resistance by changing their calibre to maintain the mean arterial pressure[121]. Accordingly, from the central arteries to more peripheral vessels a reduction of the relative importance of the elastic components (elastin and collagen) occurs, while the action of smooth muscle component increases. Along with these structural characteristics, it is worth recalling that deformability also depends on geometry, being a function of diameter.

In this model a non-linear viscoelastic constitutive relation is considered. For the sake of of clarity, we present separately the elastic (P_e) and the viscous (P_v) pressure components, so that

$$P(x,t) = P_e(x,t) + P_v(x,t). \tag{2.32}$$

The elastic component is modelled following Langewouters[96] and Reymond *et al.*[145]. Therefore, the elastic component of arterial compliance, C_A^e, is written as

$$C_A^e = \frac{\partial A}{\partial P_e} = C_d^e(d(x))\ C_p^e(P_e). \tag{2.33}$$

where C_d^e and C_p^e are the geometry- and pressure-dependant components, and $d(x)$ is the tapered arterial diameter. Using the Bramwell-Hill relation the geometry-dependent term is written as $C_d^e(d(x,t)) = A(x,t)/(\rho PWV(x,t)^2)$, where PWV is the pulse wave velocity, which can, in turn, be expressed as a function of the diameter as $PWV(d(x,t)) = a_2/d(x,t)^{b_2}$, where a_2 =13.3 $\mathrm{m}^{1.3}/\mathrm{s}$ and b_2 =0.3[145]. In the geometry-dependent term the diameter is approximated as $d_0(x)$, i.e. the diameter evaluated at the reference pressure P_0=100 mmHg, being its changes small during the cardiac cycle.

The pressure-dependent component can be written as[96]

$$C_p^e(P_e) = a_1 + \frac{b_1}{1 + \left[\frac{P_e - P_{maxC}}{P_w}\right]^2}, \tag{2.34}$$

where a_1, b_1, P_{maxC}, and P_w are fitting parameters. Reymond *et al.*[145] demonstrated that relation (2.34) holds throughout the main arterial tree.

In order to obtain P_e as an explicit function of area, and recalling that we work in the $\{Q, A\}$ space, equation (2.33) is integrated and fitted with an invertible function, $A_p(P_e)$, as

$$A_p(P_e) = \int_{P_e} C_p^e \mathrm{d}P_e \approx a_3 P_e^{1/3} + a_5, \tag{2.35}$$

where a_3=1914 $\mathrm{N}^{2/3}/\mathrm{m}^{4/3}$ and a_5=-45348 $\mathrm{N/m}^2$ in the physiological pressure range of 50-120 mmHg (the coefficient of determination is R^2=0.994).

The elastic component is then obtained as the product of the inverse of the function $A_p(P_e)$ by the geometry-dependent component, $C_d^e(d_0(x))$. After some manipulations one obtains

$$P_e(x,t) = \left(\rho \frac{PWV^2(d_0(x))}{a_3} \frac{A(x,t) - A_0}{A_0} - \frac{a_5}{a_3}\right)^3. \tag{2.36}$$

Finally, the elastic component of the constitutive equation is obtained from equation (2.36) by expanding it as a polynomial function of the area $A(x,t)$, i.e.

$$P_e(x,t) = B_1(x) + B_2(x)A(x,t) + B_3(x)A(x,t)^2 + B_4(x)A(x,t)^3 \tag{2.37}$$

where the space-dependent coefficients B_i (i = 1-4), which embed information about the local mechanical properties of the arterial walls, are written as

$$B_1 = -\frac{1}{a_3^3}(a_5^3 + PWV^6\rho^3 + 3PWV^4\rho^2 a_5 + 3a_5^2 PWV^2\rho) \quad \left[\frac{\mathrm{N}}{\mathrm{m}^2}\right]$$

$$B_2 = \frac{3\rho PWV^2}{A_0 a_3^3}(\rho^2 PWV^4 + 2\rho a_5 PWV^2 + a_5^2) \quad \left[\frac{\mathrm{N}}{\mathrm{m}^4}\right]$$

$$B_3 = -\frac{3\rho^2 PWV^4}{A_0^2 a_3^3}(a_5 + \rho PWV^2) \quad \left[\frac{\mathrm{N}}{\mathrm{m}^6}\right]$$

$$B_4 = \left(\frac{\rho PWV^2}{a_3 A_0}\right)^3 \quad \left[\frac{\mathrm{N}}{\mathrm{m}^8}\right].$$

It is worth recalling that this procedure can be easily extended to other forms of non-linear elasticity.

About the viscoelastic behaviour, we follow the recently recalled [17] approach of Kivity and Collins[87], by posing

$$P_v(x,t) = \frac{kh_0}{2\sqrt{A_0(x)}R_0(x)} \frac{1}{\sqrt{A(x,t)}} \frac{\partial A(x,t)}{\partial t} \tag{2.38}$$

where k is the wall effective viscosity and h_0 is the arterial wall thickness at reference pressure. Exploiting the continuity equation (2.25) time derivative can be eliminated so that

$$P_v(x,t) = -B_5(x) \frac{1}{\sqrt{A(x,t)}} \frac{\partial Q(x,t)}{\partial x}. \tag{2.39}$$

where $B_5(x) = (kh_0)/(2\sqrt{A_0}R_0)$.

Finally, the constitutive equation reads

$$P = B_1 + B_2 A + B_3 A^2 + B_4 A^3 - B_5 \frac{1}{\sqrt{A}} \frac{\partial Q}{\partial x} \tag{2.40}$$

that, substituted into equation (2.31), gives

$$\frac{\partial Q}{\partial t} + \frac{\partial}{\partial x}\left(\beta \frac{Q^2}{A}\right) + \frac{A}{\rho}\frac{\partial}{\partial x}\left(B_1 + B_2 A + B_3 A^2 + B_4 A^3 - B_5 \frac{1}{\sqrt{A}} \frac{\partial Q}{\partial x}\right) = \\ = Ag \sin\gamma + N_4. \tag{2.41}$$

2.2.3 Left ventricle

Left ventricle (LV) is represented by a time-varying elastance model [155]. The elastance, $E_{LV}(t)$, modules force of contraction by relating the left-ventricular pressure (P_{LV}) to the corresponding volume (V_{LV}) as

$$E_{LV}(t) = \frac{P_{LV}(t)}{V_{LV}(t) - V_0}, \tag{2.42}$$

where V_0 is a corrective volume.

The elastance function is described as [131]

$$E_{LV}(t) = E_{min,LV}(1 - \Phi(t)) + E_{max,LV}\Phi(t) \tag{2.43}$$

being $E_{max,LV}$ and $E_{min,LV}$ the maximal and the minimal elastance, respectively, and $\Phi(t)$ the activation function

$$\Phi(t) = \begin{cases} a_\Phi \sin(\frac{\pi t}{t_{ce}}) - b_\Phi \sin(\frac{2\pi t}{t_{ce}}) & \text{if } 0 < t \leq t_{ce} \\ 0 & \text{if } t_{ce} < t < T \end{cases} \tag{2.44}$$

where $a_\Phi = 0.9$, $b_\Phi = 0.25$, t_{ce} is the time for onset of constant elastance, and T is the heart period.

2.2.4 Cardiac valves

Mitral valve is modelled as an ideal diode with a resistive component. The flow through the mitral valve is given by $Q_{MI} = (P_{LV} - \bar{P}_{LA})/R_{MI}$, where $\bar{P}_{LA}$ is the imposed left-atrial pressure and the resistance R_{MI} instantaneously switch from a value of 3 mmHg s/L[145] to infinite when the pressure gradient becomes negative.

Differently from the mitral valve, aortic leaflets are modelled to move freely between a minimum, θ_{min}, and a maximum, θ_{max}, opening angle, depending on the forces applied, and leaflet dynamics results from a system of ordinary differential equations, as described in the apposite Section for the lumped model.

Following Blanco *et al.*[17], the pressure-flow relation for the aortic valve is

$$L\frac{\mathrm{d}Q}{\mathrm{d}t} + RQ + B|Q|Q = \Theta(P_{LV} - P) \tag{2.45}$$

where P is the ascending aorta pressure, L accounts for the inertance of the fluid, B is the turbulent flow separation coefficient, and R is the viscous resistance. The aortic valve opening angle dynamics is modelled following Korakianitis and Shi[89], as described in the precedent Section for the lumped model.

2.2.5 Small arteries and micro-circulation

The arterial tree is terminated by three-element Windkessel models, namely lumped representations of the distal arterial behaviour. Distal circulation response is represented by a first entering resistance R_1, followed by a parallel combination of a resistance R_2 and a capacitance C. As reflections vanish at high frequencies[145],

the first resistance R_1 equals the characteristic impedance of the terminating vessel, while the second resistance is calculated as the difference between the total resistance R_T and R_1. The capacitor C considers the effect of the volumetric compliance of the distal arterioles.

This distal model corresponds to

$$\frac{\mathrm{d}Q}{\mathrm{d}t} - \frac{1}{R_1}\frac{\mathrm{d}P}{\mathrm{d}t} = \frac{P - P_{ven}}{R_1 R_2 C} - \Big(1 + \frac{R_1}{R_2}\Big)\frac{Q}{R_1 C} \tag{2.46}$$

where Q and P are flow and pressure at the distal boundary, and $P_{ven} = 5$ mmHg is a constant pressure in the microcirculation.

2.2.6 Vessel bifurcation

At any arterial bifurcation, conservation of total pressure and mass are set. Considering a generic bifurcation where a parent vessel (1) splits into two daughter vessels (2 and 3); the conservation of total pressure reads

$$\begin{aligned} P_1(L_1,t) + \frac{1}{2}\rho\bar{u}_1(L_1,t)^2 &= P_2(0,t) + \frac{1}{2}\rho\bar{u}_2(0,t)^2 \\ P_1(L_1,t) + \frac{1}{2}\rho\bar{u}_1(L_1,t)^2 &= P_3(0,t) + \frac{1}{2}\rho\bar{u}_3(0,t)^2 \end{aligned} \tag{2.47}$$

where the subscripts refer to the vessel number, L is the vessel length, and $\bar{u}$ is the mean velocity. Mass conservation further entails

$$Q_1(L_1,t) = Q_2(0,t) + Q_3(0,t). \tag{2.48}$$

These relations are solved along with the outgoing characteristics of the three vessels.

2.2.7 Numerical Method

In the next Section a detailed description of the mathematical model is proposed. The model is solved using a Runge-Kutta Discontinuous-Galerkin method[40]: first, space is discretized by a Discontinuous-Galerkin approach, then time evolution is described by a second-order Runge-Kutta scheme.

Conservative form

In conservative form, model (2.25) and (2.41) reads

$$\frac{\partial \mathbf{U}}{\partial t} + \frac{\partial \mathbf{F}(\mathbf{U})}{\partial x} + \mathbf{S}(\mathbf{U}) = 0 \tag{2.49}$$

where $\mathbf{U} = [A(x,t), Q(x,t)]^T$ are the conservative variables, whereas the corresponding fluxes and source terms are

$$\mathbf{F}(\mathbf{U}) = \begin{bmatrix} Q \\ \beta \frac{Q^2}{A} + \sum_{j=2}^{4} \frac{j-1}{\rho j} A^j B_j - \frac{B_5}{\rho}\sqrt{A}\frac{\partial Q}{\partial x} \end{bmatrix},$$

$$\mathbf{S}(\mathbf{U}) = \begin{bmatrix} 0 \\ \sum_{j=1}^{4} \frac{A^j}{\rho j}\frac{\mathrm{d}B_j}{\mathrm{d}x} + \frac{B_5}{\rho\sqrt{A}}\frac{\partial Q}{\partial x}\frac{\partial A}{\partial x} - N_4 - A\, b_x \end{bmatrix},$$

where $b_x = g\sin(\gamma)$ is the longitudinal projection of the gravitational acceleration.

To solve system (2.49) in a one-dimensional generic domain Ω discretized into N_{el} elemental non-overlapping regions $\Omega_e = [x_e^l, x_e^r]$ – such that $x_{e+1}^l = x_e^r$ for $e = 1, ..., N_{el}$ and $\cup_{e=1}^{N_{el}} \Omega_e = \Omega$ – the weak form of equation (2.49) is written

$$\left(\frac{\partial \mathbf{U}}{\partial t}, \boldsymbol{\psi}\right)_\Omega + \left(\frac{\partial \mathbf{F}}{\partial x}, \boldsymbol{\psi}\right)_\Omega + \Big(\mathbf{S}, \boldsymbol{\psi}\Big)_\Omega = 0 \tag{2.50}$$

where $\boldsymbol{\psi}$ is a set of arbitrary test functions in Ω and $(\mathbf{v}, \mathbf{p})_\Omega = \int_\Omega \mathbf{vp}\mathrm{dx}$ is the standard $\mathbf{L}^2(\Omega)$ inner product between two generic function $\mathbf{v}$ and $\mathbf{p}$ whose domain is the closed interval Ω. Decomposing the integrals in equation (2.50) into elemental regions, one obtains

$$\sum_{e=1}^{N_{el}} \left[\left(\frac{\partial \mathbf{U}}{\partial t}, \boldsymbol{\psi}\right)_{\Omega_e} + \left(\frac{\partial \mathbf{F}}{\partial x}, \boldsymbol{\psi}\right)_{\Omega_e} + \Big(\mathbf{S}, \boldsymbol{\psi}\Big)_{\Omega_e} \right] = 0. \tag{2.51}$$

The second term can be integrated by part, obtaining

$$\sum_{e=1}^{N_{el}} \left[\left(\frac{\partial \mathbf{U}}{\partial t}, \boldsymbol{\psi}\right)_{\Omega_e} - \left(\mathbf{F}, \frac{d\boldsymbol{\psi}}{dx}\right)_{\Omega_e} + [\mathbf{F}\boldsymbol{\psi}]_{\partial\Omega_e} + \Big(\mathbf{S}, \boldsymbol{\psi}\Big)_{\Omega_e} \right] = 0. \tag{2.52}$$

In order to discretize the problem in space, $\mathbf{U}$ is assumed to belong to the finite dimensional space of the $\mathbf{L}^2(\Omega)$ functions – that are polynomials of degree 1 on each element Ω_e – obtaining the approximate solution $\mathbf{U}_h$ (subscript h marks an element of such a space). Even if the solution $\mathbf{U}_h$ can be discontinuous at boundaries between elemental regions, information propagates by upwinding the fluxes $\mathbf{F}$ on the third term of equation (2.52).

The approximate solution $\mathbf{U}_h = \mathbf{U}_h(x,t)$ on the element Ω_e can be represented as

$$\mathbf{U}_h(x_e(\xi),t) = \sum_{i=1}^{2} \alpha_i(t)\phi_i(\xi)$$

where α_i are the time dependent unknown weights, $\phi_i(\xi)$ are the trial functions on the reference element $\hat{\Omega} = [-1,1]$, and the following affine mapping between $\hat{\Omega}$ and Ω_e is introduced

$$x_e(\xi) = x_e^l \frac{1-\xi}{2} + x_e^r \frac{1+\xi}{2}.$$

We choose first-degree Lagrange functions as expansion polynomial basis, $\phi_1(\xi) = (1-\xi)/2$, $\phi_2(\xi) = (1+\xi)/2$, and, following the usual Galerkin approach, the discrete test functions $\boldsymbol{\psi}_h$ are chosen in the same discrete space as the numerical solution $\mathbf{U}_h$.

Introducing the approximate solution $\mathbf{U}_h$ and the discrete test function into relation (2.52), one obtains the weak formulation as

$$\sum_{e=1}^{N_{el}} \Bigg[\left(\frac{\partial \mathbf{U}_h}{\partial t}, \boldsymbol{\psi}_h \right)_{\Omega_e} - \left(\mathbf{F}(\mathbf{U}_h), \frac{d\boldsymbol{\psi}_h}{dx} \right)_{\Omega_e} + \\ + \left[\mathbf{F}_{LF}\, \boldsymbol{\psi}_h \right]_{\partial\Omega_e} + \Big(\mathbf{S}(\mathbf{U}_h), \boldsymbol{\psi}_h \Big)_{\Omega_e} \Bigg] = 0 \quad (2.53)$$

where $\mathbf{F}_{LF}$ are the upwinded numerical fluxes. They are obtained using the Lax-Friedrichs method as

$$\mathbf{F}_{LF} = \frac{1}{2}(\mathbf{F}(\mathbf{U}^-) + \mathbf{F}(\mathbf{U}^+) - \lambda_{max}(\mathbf{U}^+ - \mathbf{U}^-))$$

where $\mathbf{U}^+$ ($\mathbf{U}^-$, resp.) are the variables on the right (left, resp.) side of the boundary and λ_{max} is the maximum eigenvalue of the matrix $\mathbf{H}(\mathbf{U})$ of the quasi-linear form (see eq. (2.55), below).

The formulation (2.53) is then advanced in time by a second-order Runge-Kutta explicit method. The choice of such a low-order time-advancing scheme is coherent with the spatial discretization, in which the order of the expansion polynomial is one. This method is stable if the well-known Courant-Friedrichs-Lewy (CFL) condition is satisfied.

Treatment of the boundary conditions

When characteristics have slopes of opposite signs – as in the present situation, see below –, the differential system (2.25) and (2.41) needs only one physical condition at each domain boundary. However, the solution of the numerical problem requires to prescribe both variables at each boundary. For this reason, extra relations (called compatibility equations) have to be written at each boundary by projecting the differential equations along the outgoing characteristics.

Quasi-linear form

In order to formulate compatibility conditions, system (2.49) is written in quasi-linear form as

$$\frac{\partial \mathbf{U}}{\partial t} + \mathbf{H}(\mathbf{U})\frac{\partial \mathbf{U}}{\partial x} + \mathbf{S}_2(\mathbf{U}) = 0 \tag{2.54}$$

where the terms

$$\mathbf{H}(\mathbf{U}) = \begin{bmatrix} 0 & 1 \\ \frac{1}{\rho}\sum_{j=1}^{4} j A^j B_{j+1} - \beta\frac{Q^2}{A^2} & 2\beta\frac{Q}{A} \end{bmatrix},$$

$$\mathbf{S}_2(\mathbf{U}) = \begin{bmatrix} 0 \\ \frac{1}{\rho}\sum_{j=1}^{4} j A^j \frac{\mathrm{d}B_j}{\mathrm{d}x} - N_4 - A\, b_x \end{bmatrix}$$

are obtained by neglecting viscoelasticity. Notice that the characteristic variables move along the corresponding characteristic directions for a spatial distance equal to the product of the time step by the local wave celerity. Being both time step and celerity small, the

spatial distance is very small thus allowing the viscoelastic effect to be neglected.

Let $\mathbf{\Lambda}$ and $\mathbf{L}$ be the eigenvalue and left eigenvector matrices of $\mathbf{H}(\mathbf{U})$, respectively, so that $\mathbf{LHL}^{-1} = \mathbf{\Lambda}$. They read

$$\mathbf{\Lambda}(\mathbf{U}) = \begin{bmatrix} \lambda_1 & 0 \\ 0 & \lambda_2 \end{bmatrix} \qquad \mathbf{L}(\mathbf{U}) = \begin{bmatrix} -\lambda_2 & 1 \\ -\lambda_1 & 1 \end{bmatrix}.$$

In the present case, the eigenvalues read

$$\lambda_1 = \beta \frac{Q(x,t)}{A(x,t)} - c(x,t), \qquad \lambda_2 = \beta \frac{Q(x,t)}{A(x,t)} + c(x,t)$$

where

$$c(x,t) = \sqrt{\frac{A}{\rho}(B_2 + 2B_3 A + 3B_4 A^2) + (\beta - 1)\beta \frac{Q^2}{A^2}}$$

is the celerity of the propagation when the fluid is at rest. At least in physiological condition, the system results strictly hyperbolic because c is always greater than $\beta Q/A$, entailing $\lambda_1 < 0$ (backward propagation) and $\lambda_2 > 0$ (forward propagation).

Compatibility conditions

Characteristic variables $\mathbf{W}$ are defined as

$$\frac{\partial \mathbf{W}}{\partial \mathbf{U}} = \mathbf{L}(\mathbf{U}). \tag{2.55}$$

Due to the present structure of the matrix $\mathbf{L}$, it is not possible to obtain the characteristic variables analytically. Therefore, pseudo-characteristic variables are introduced by linearising equation (2.55).

By pre-multiplying the vectorial equation (2.54) by the left eigenvector matrix, one obtains

$$\mathbf{L}(\mathbf{U})\frac{\partial \mathbf{U}}{\partial t} + \mathbf{L}(\mathbf{U})\mathbf{H}(\mathbf{U})\frac{\partial \mathbf{U}}{\partial x} + \mathbf{L}(\mathbf{U})\mathbf{S}_2(\mathbf{U}) = 0$$

and then

$$\mathbf{L}(\mathbf{U})\frac{\partial \mathbf{U}}{\partial t} + \mathbf{\Lambda}(\mathbf{U})\mathbf{L}(\mathbf{U})\frac{\partial \mathbf{U}}{\partial x} + \mathbf{L}(\mathbf{U})\mathbf{S}_2(\mathbf{U}) = 0. \tag{2.56}$$

In order to introduce the total derivative, the first term of equation (2.56) is rewritten as

$$\mathbf{L}(\mathbf{U})\frac{\partial \mathbf{U}}{\partial t} = \frac{\partial}{\partial t}\Big(\mathbf{L}(\mathbf{U})\mathbf{U}\Big) - \mathbf{U}\frac{\partial \mathbf{L}(\mathbf{U})}{\partial t}$$

and the second term as

$$\mathbf{\Lambda}(\mathbf{U})\mathbf{L}(\mathbf{U})\frac{\partial \mathbf{U}}{\partial x} = \mathbf{\Lambda}(\mathbf{U})\frac{\partial}{\partial x}\Big(\mathbf{L}(\mathbf{U})\mathbf{U}\Big) - \mathbf{\Lambda}(\mathbf{U})\mathbf{U}\frac{\partial \mathbf{L}(\mathbf{U})}{\partial x},$$

obtaining

$$\begin{aligned}\frac{\partial}{\partial t}\Big(\mathbf{L}(\mathbf{U})\mathbf{U}\Big) + \mathbf{\Lambda}(\mathbf{U})\frac{\partial}{\partial x}\Big(\mathbf{L}(\mathbf{U})\mathbf{U}\Big) + \\ - \mathbf{\Lambda}(\mathbf{U})\mathbf{U}\frac{\partial \mathbf{L}(\mathbf{U})}{\partial x} - \mathbf{U}\frac{\partial \mathbf{L}(\mathbf{U})}{\partial t} + +\mathbf{L}(\mathbf{U})\mathbf{S}_2(\mathbf{U}) = 0.\end{aligned}$$

By introducing the total derivative $\mathrm{D}/\mathrm{D}t$, the last equation becomes

$$\frac{D\mathbf{L}(\mathbf{U})\mathbf{U}}{Dt} - \mathbf{\Lambda}(\mathbf{U})\mathbf{U}\frac{\partial \mathbf{L}(\mathbf{U})}{\partial x} - \mathbf{U}\frac{\partial \mathbf{L}(\mathbf{U})}{\partial t} + \mathbf{L}(\mathbf{U})\mathbf{S}_2(\mathbf{U}) = 0. \quad (2.57)$$

If time is now discretized so that $\Delta t = t_{n+1} - t_n$ is the time step (the subscript n denotes the n-th time instant), the total derivative can be approximated as

$$\begin{aligned}\frac{D}{Dt}\Big(\mathbf{L}_{n+1}\mathbf{U}_{n+1}\Big) \approx \frac{\mathbf{L}_{n+1}\mathbf{U}_{n+1} - \mathbf{L}_n^\star\mathbf{U}_n^\star}{\Delta t} = \\ = \frac{\mathbf{L}_n\mathbf{U}_{n+1} - \mathbf{L}_n^\star\mathbf{U}_n^\star}{\Delta t} + \frac{(\mathbf{L}_{n+1} - \mathbf{L}_n)\mathbf{U}_{n+1}}{\Delta t} \quad (2.58)\end{aligned}$$

where the superscript $\star$ refers to the point located at the distance from the boundary equal to $c \cdot \Delta t$. By assuming that

$$\frac{(\mathbf{L}_{n+1} - \mathbf{L}_n)\mathbf{U}_{n+1}}{\Delta t} \approx \mathbf{U}\frac{\partial \mathbf{L}(\mathbf{U})}{\partial t}$$

the departure of the pseudo-characteristic from a generic state $\mathbf{U}_n^\star$ is taken as

$$\mathbf{L}_n\mathbf{U}_{n+1} = \mathbf{L}_n^\star\mathbf{U}_n^\star + \Delta t\left(\mathbf{\Lambda}_n^\star\frac{\partial \mathbf{L}_n^\star}{\partial x}\mathbf{U}_n^\star - \mathbf{L}_n^\star\mathbf{S}_2(\mathbf{U}_n^\star)\right) \quad (2.59)$$

where $\mathbf{L}_n = \mathbf{L}(\mathbf{U}_n)$ and $\mathbf{\Lambda}_n = \mathbf{\Lambda}(\mathbf{U}_n)$.

Finally, because the pseudo-characteristics at the initial state are set null, equation (2.59) needs to be balanced by subtracting the initial condition to the dependent variables[105], i.e.

$$\begin{aligned}\mathbf{L}_n(\mathbf{U}_{n+1} - \mathbf{U}_0) = \mathbf{L}_n^\star(\mathbf{U}_n^\star - \mathbf{U}_0^\star) + \\ + \Delta t \left(\mathbf{\Lambda}_n^\star \frac{\partial \mathbf{L}_n^\star}{\partial x}(\mathbf{U}_n^\star - \mathbf{U}_0^\star) - \mathbf{L}_n^\star(\mathbf{S}_2(\mathbf{U}_n^\star) - \mathbf{S}_2(\mathbf{U}_0^\star))\right) \quad (2.60)\end{aligned}$$

where the subscript 0 refers to the initial condition. Since the reference condition (uniform pressure of 100 mmHg and no flow) is assumed as initial condition, the same subscript 0 is used to define both quantities.

The formulation (2.60) has to be coupled with the physical boundary conditions (2.47, 2.48) at every (internal and external) boundary. The corresponding non-linear systems are solved by an adaptive trust-region-dogleg method.

2.2.8 Initial Conditions and parameters values

Sizes and distal values of the arterial tree refer to the benchmark data set collected by different authors in the last 60 years: the starting data set collected by Noordergraaf *et al.*[123], has been subsequently adapted[171;192], and recently updated[145]. Since we are not interested here in a detailed description of the cerebral circulation, and considering that the effect of such a district has been found to be minimal on the aorta[145], we chose to limit our network to the main 48 arteries by excluding the cerebral arteries, as proposed in Stergiopulos *et al.*[171]. Similarly to Reymond *et al.*[144], resistances have been multiplied by a correction factor (here equal to 1.95) in order to obtain realistic ranges of pressure. Wall thickness, viscoelasticity coefficients, parameters of the aortic valve pressure-flow relation, and the extreme values of the elastance are the ones adopted in Blanco *et al.*[17]. Heart rate is set to 75 bpm, gravity is not considered, and blood rheological properties used are: $\rho = 1050\,\mathrm{Kg/m^3}$ and $\mu = 0.004\,\mathrm{Pa\ s}$. Finally, taking advantage of the symmetry, only one leg is simulated.

Simulations were carried out with a time step equal to $3 \cdot 10^{-4}$ s and a mean element length of 2.5 cm, resulting in a maximum CFL

number of 0.2. Error analysis confirmed that the model is second-order accurate, i.e. the error scales proportionally to the square of the time step. Results showed not to be sensitive to the initial conditions, converging to the same periodic solution. Choosing an initial condition of constant pressure (100 mmHg) and no flow, the numerical scheme reached the convergence – fixed to a maximum difference of pressures between two consecutive cardiac cycles less than 1 % – in around five heart cycles.

Chapter 3

Results from the lumped model

In this Chapter the results obtained from the application of the lumped model are presented. In particular, the lumped model has been used to understand and characterize the atrial fibrillation.

3.1 Atrial fibrillation

Atrial fibrillation (AF) occurs when the electrical activity of the atria, governed by the sinoatrial node, is disorganized, causing irregular and rapid heartbeats[58]. AF can lead to disabling symptoms, such as palpitations, chest discomfort, anxiety, fall in blood pressure, decreased exercise tolerance, pulmonary congestion, which are all related to rapid heart rate and inefficient cardiac output. Moreover, the persistence of fibrillated conditions can enhance heart failure and stroke, being AF responsible for 15 to 20 percent of ischemic strokes, and increasing the risk of suffering an ischemic stroke by five times[103].

The estimated number of individuals with atrial fibrillation globally in 2010 was 33.5 million[38]. AF incidence gets higher with age: 2.3% of people older than 40 years are affected, up to more than 8% of people older than 80 years[90], with a prevalence which is markedly amplifying in industrialized countries[5]. AF currently affects almost 7 million people in the USA and Europe, but because of the rise of life expectancy in Western countries, incidence

is expected to double within the next forty years [103]. Nevertheless, AF is responsible for substantial morbidity and mortality in the general population [12], with an increased risk for all-cause mortality [53]. Treatment of AF gives rise to huge healthcare costs. The treatment for diagnosis and therapy was estimated around 6.65 billion per year for the US [44].

For the above reasons, AF is a subject of broad interest under several aspects. Some examples are, among many others, statistical analyses on the heartbeat distributions [74;177], risk factors [82;179] and correlation with other cardiac pathologies [184].

However, several key points on the consequences of AF are not completely understood [104]. Literature data, as we will show later on, reveal for example contrasting trends regarding pulmonary and systemic arterial pressures during AF: hypotension, normotension and hypertension seem to be equally probable when AF emerges. Invasive measures could, for instance, better clarify how AF acts on arterial systemic and pulmonary pressures. But, these and other non-invasive measures are often difficult to be performed especially during atrial fibrillation, since the heart rate variability causes problems to oscillometric instruments and the clinical framework often requires immediate medical treatment. Moreover, the anatomical and structural complexity of some cardiac regions (e.g., right ventricle) makes estimates not always feasible and accurate [71]. This leads to a substantial absence of well-established information regarding the behaviour of the right ventricle and central venous pressure during AF. Nevertheless, AF usually occurs in presence of other pathologies (such as hypertension, atrial dilatation, coronary heart disease, mitral stenosis). Therefore, the specific role of atrial fibrillation on the whole cardiovascular system is not easily detectable and distinguishable. It is still nowadays debatable whether atrial dilatation acts mainly as cause or effect of AF events [130;157], while the role of hypertension as causative agent and predictor makes it difficult to discern whether it is also a consequence of AF [184].

This research arises in this scenario and aims at being a first attempt to quantify, through a stochastic modelling approach, the impact of acute AF on the cardiovascular variables with respect to the normal rhythm. Structural remodelling effects due to persistent or chronic AF are not taken into account.

Our goal of understanding the global response of the cardiovascular system during fibrillated paroxysmal events can be achieved by means of a lumped-parameter approach[89], which is here carried out paying particular attention to the stochastic modelling of the irregular heartbeats and the reduced contractility function of the heart. In particular, the beating model accounts for a time-correlated regular beat typical of the normal rhythm, while the irregular fibrillated beating is composed by two differently correlated random distributions.

The proposed approach has a double advantage. First, AF conditions can be analysed without the presence of other side pathologies. Therefore, the outcomes should be read as purely consequent of a fibrillated cardiac status in a healthy young adult. To this end, the AF parametrization through the modelling is presented to highlight single cause-effect relations, trying to address from a mechanistic point of view the cardiovascular feedbacks which are currently poorly understood. Second, the main cardiac variables and hemodynamics parameters can all be obtained at the same time, while clinical studies usually focus only on a few of them at a time. The present global response is indeed compared with more than thirty works in literature, which describe the variations of different hemodynamic features between normal sinus rhythm and atrial fibrillation conditions. The overall agreement with clinical state-of-the-art measures is rather good. Moreover, additional information related to the statistical properties of the cardiovascular variables as well as hemodynamic parameters (such as right ventricle data) which are difficult to measure and almost never offered in literature, are here provided. An accurate statistical analysis of the cardiovascular dynamics, yielding the main values and the probability distributions, is not easily accomplished by in vivo measurements, while it is here carried out thanks to the statistically stationarity of the performed simulations.

Cardiac cycle simulation: physiologic and fibrillated beating

The main aim of the present work is to compare the cardiovascular outcomes of the physiologic case (normal sinus rhythm, NSR) with those during acute AF events. We recall that RR [s] is the temporal

range between two consecutive heart beats, while the heart rate, HR, is the number of heartbeats per minute, so that $HR = 60/RR$ bpm.

The normal heart-beating is an example of pink noise, which means that the electrocardiogram has an approximately $1/f$ power spectrum[74;88], where f is the beat frequency. The presence of a pink noise induces a temporal correlation, differently from the white noise, which is instead uncorrelated. During NSR the RR interval is usually Gaussian distributed[75;137], with a coefficient of variation $cv{=}\sigma/\mu$, where σ is the standard deviation and μ is the mean value of the RR distribution, which is between 0.05 and 0.13 [137;168]. Thus, we here extract the RR intervals from a pink Gaussian distribution with an average value for normal adults, μ=0.8 s, and choosing cv=0.07. Pink noise is generated as follows. An uncorrelated temporal signal is created extracting values from a white Gaussian distribution. A Fourier transform of the signal is carried out and the spectrum is multiplied by a filter so that the resulting spectral density is proportional to $1/f$. In the end, an inverse Fourier transform is performed to recover the filtered signal in time.

During AF, the RR distribution can be unimodal (61% of the cases), bimodal (32%), trimodal (5%), or multimodal (2%)[191]. The presence of multiple modes is often attributed to a modification of the atrio-ventricular node conduction properties[148;191]. Here we focus on the unimodal distribution, affecting the large part of AF patients, which can be fully described by the superposition of two statistically independent times[74;75], $RR{=}\tau{+}\eta$. τ is extracted from a correlated pink Gaussian distribution (mean μ_G, standard deviation σ_G), while η is drawn from an uncorrelated exponential distribution (rate parameter γ). The resulting RR distribution is an exponentially modified Gaussian (EMG) distribution, with mean $\mu{=}\mu_G + \gamma^{-1}$, standard deviation $\sigma{=}\sqrt{\sigma_G^2 + \gamma^{-2}}$, and probability density function:

$$\begin{aligned} p(RR;\mu_G,\sigma_G,\gamma) &= \frac{\gamma}{2} e^{\frac{\gamma}{2}(2\mu_G+\gamma\sigma_G^2-2RR)} \\ &\times \operatorname{erfc}\left(\frac{\mu_G+\gamma\sigma_G^2-RR}{\sqrt{2}\sigma_G}\right), \end{aligned} \tag{3.1}$$

where erfc(·) is the complementary error function. The parameters are suggested by the fibrillated RR data available[75;168], and by considering that the coefficient of variation, cv, is around 0.24 during AF[177].

In Fig. 3.1a, the fibrillated and physiologic distributions, from which RR intervals are extracted, are shown for comparison.

Two other important features of the AF are introduced into the model. First, there is a complete loss of atrial contraction[42;138], which can be taken into account, for both atria, by considering a constant atrial elastance. In so doing, we exclude the *atrial kick*, i.e. the atrial contribution to the ventricular filling during late diastole. Second, a reduced systolic left ventricular function is experienced during AF[29;175] and this aspect is included by decreasing the maximum left ventricular elastance, $E_{lv,max}$, to a value depending on the preceding ($RR1$) and pre-preceding ($RR2$) heartbeats[175]:

$$E_{lv,max} = 0.59\frac{RR1}{RR2} + 0.91 \text{ mmHg/ml}. \tag{3.2}$$

A reduced contractile capacity is also observed for the right ventricle[71]. However, since the partial disfunction of the right ventricle cannot be easily traduced into elastance terms, here we prefer not to change the $E_{rv,max}$ value with respect to the normal case.

Runs

The duration of AF episodes can greatly vary, depending on which kind of fibrillation is considered[58]. For example, during paroxysmal atrial fibrillation recurrent episodes usually occur and self-terminate in less than 7 days. Permanent fibrillation instead induces an ongoing long-term episode, which can last up to a year or more.

The model equations are integrated in time until the main statistics (mean and variance) of the cardiac variables remain insensitive to further extensions of the computational domain size, highlighting the statistically steadiness of the results. The first 20 periods are left aside since they reflect the transient dynamics of the system. In fact, the NSR configuration shows periodic solutions after 5-6 cycles (also refer to[89]), therefore we can assume that for both NSR and AF simulations the transient dynamics are

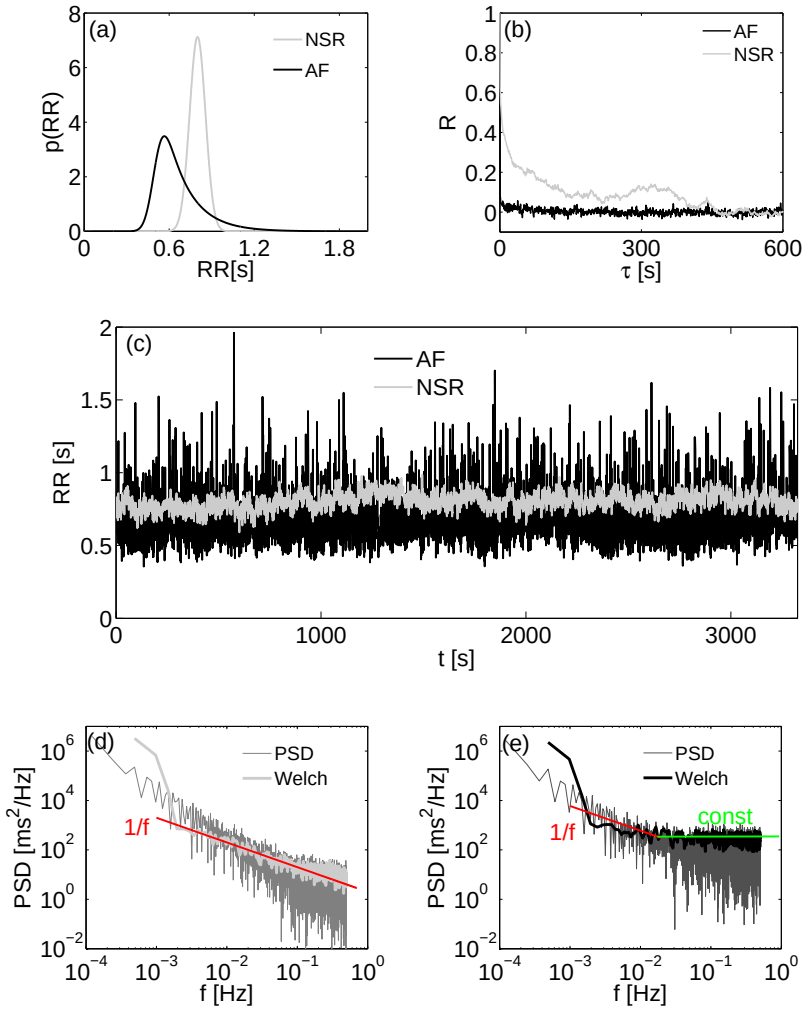

Figure 3.1. (a) RR distributions: NSR (μ=0.8 s, σ=0.06 s), AF (μ_G=0.5 s, σ_G=0.05 s, γ=6 Hz). (b) Autocorrelation functions, R. (c) RR temporal series. (d)-(e) Power spectrum density, PSD: (d) NSR, (e) AF. Light: NSR, dark: AF

completely extinguished after 20 periods. Once the system exceeds the transient and reaches a statistically stationary state, 5000 cycles are then simulated for the normal and the fibrillated cases. Our choice of computing 5000 heartbeats can be thought of as a representative acute fibrillation episode of about one hour length,

affecting a healthy young adult without pre-existing and structural pathologies.

The two simulated cases are listed below:

(a) Normal sinus rhythm (NSR)

- RR extracted from a correlated pink Gaussian distribution: μ=0.8 s, σ=0.06 s;
- Time varying (right and left) atrial elastance;
- Full left ventricular contractility: $E_{lv,max}$=2.5 mmHg/ml.

(b) Atrial fibrillation (AF)

- RR extracted from an EMG distribution: μ_G=0.5 s, σ_G=0.05 s, γ=6 Hz; μ=0.67 s, σ=0.17 s, cv=0.26;
- Constant (right and left) atrial elastance;
- Reduced left ventricular contractility, Eq. (3.2). depending on the preceding, $RR1$, and the pre-preceding, $RR2$, heartbeats:
  $E_{lv,max} = 0.59\, RR1/RR2 + 0.91$ mmHg/ml.

For both NSR and AF we report the autocorrelation functions, R, (Fig. 3.1b), the RR time series (Fig. 3.1c), and the power spectrum density, PSD (Fig. 3.1, panels d and e), computed directly from the RR series (thin curves), and estimated through the Welch method (thick curves) to smooth the oscillations. The NSR spectrum shows the typical $1/f$ power-law scaling observed in healthy subjects, while the AF spectrum displays two distinct power-law scalings which is a common feature of a real fibrillated beating[74;75]. As for the autocorrelation function, R, during AF it immediately drops to zero, revealing furthermore its uncorrelated nature with respect to the NSR.

3.1.1 Results

The proposed goal is to quantify, through a stochastic approach, the impact of atrial fibrillation on the cardiovascular variables with respect to the normal rhythm. We focus on the most relevant variables of the cardiovascular model, in terms of pressures, P, and

volumes, V. The temporal series, the probability density function (PDF), and the main statistics (computed over 5000 periods) are reported, trying to highlight significant trends emerging with a fibrillated heartbeat. The ranges where the temporal series are visualized are therefore chosen as representative of the general behaviours.

We also evaluate pressures and volumes at particular instants of the heartbeat: end-systole (ES) and end-diastole (ED). Left (or right) end-systole is the instant defined by the closure of the aortic (or pulmonary) valve, while left (or right) end-diastole corresponds to the closure of the mitral (or tricuspid) valve.

Other important hemodynamics parameters, referred to the left ventricle, are evaluated: the stroke volume (SV), the ejection fraction (EF), the stroke work (SW), and the cardiac output (CO).

When in vivo fibrillated data are available, they are compared with the present outcomes. To provide a quick overview of the comparison, the current results and the available literature data are summarized in Table 3.1, where the variations during AF with respect to NSR are synthesized as follows: + increase, − decrease, = no substantial variation, / no data available. It should be reminded that measurements come from very different types of arrythmia, i.e. persistent, chronic, paroxysmal, induced, benign fibrillations. Moreover, AF is usually present along with other pathologies, which can themselves substantially affect the cardiac response. Nevertheless, depending on the clinical case, different techniques (cardioversion, catheter ablation, drugs treatment, ...) are used to restore the normal sinus rhythm, as well as differing follow-up periods (from 24 hours to 6 months) are analyzed. The invasiveness of some medical procedures, together with the anatomical and structural heart complexity, can contribute to the incompleteness of data regarding certain hemodynamics variables (e.g., right ventricle measurements).

Keeping in mind these aspects, the literature data should not be taken for a comparison on the specific values (which can largely vary from case to case), but as indicators of general trends during AF.

The pressures P are expressed in terms of [mmHg], the volumes V in [ml], the stroke volume SV in [ml], the ejection fraction EF in percentage, the stroke work SW in [J], the cardiac output CO

Variable	Present Model	Literature Data
P_{la}	+	+ 43,161
P_{laed}	+	/
P_{laes}	+	/
P_{lv}	-	/
P_{lved}	+	- 3
P_{lves}	-	/
P_{ra}	=	+ 3,35,39,161
P_{raed}	=	/
P_{raes}	-	/
P_{rv}	=	/
P_{rved}	+	- 3
P_{rves}	-	/
V_{la}	+	= 126, - 35
V_{laed}	+	+ 1,165,172,178,198,199
V_{laes}	+	+ 1,165,172,178,198,199
V_{lv}	+	/
V_{lved}	+	+ 6,178, = 126
V_{lves}	+	+ 6,178, = 126
V_{ra}	-	/
V_{raed}	=	+ 178*
V_{raes}	-	+ 178*
V_{rv}	-	/
V_{rved}	-	+ 178*
V_{rves}	=	+ 178*
P_{sas}	-	- 42,138, + 61, = 3,39,85
$P_{sas,s}$	-	+ 61,81, = 3,39,85
$P_{sas,d}$	-	+ 61,81, = 3,39,85
P_p	-	- 81
P_{pas}	=	= 143,161, + 3,39
$P_{pas,s}$	-	+ 35,39, = 3
$P_{pas,d}$	+	+ 3,35,39
P_{svn}	-	/
P_{pvn}	+	+ 3,35,39,47, = 126
SV	-	- 3,43,61,72,156, = 85
EF	-	- 6,35,60,178,198, = 199
SW	-	- 84,126
CO	-	- 35,42,37,47,63,72,85 - 39,43,84,112,126,138,156,180 = 3,61,143,161

Table 3.1. Present outcomes (II column) and literature data (III column): + increase during AF, − decrease during AF, = no significant variations during AF, / no data available. All the variables of the present model are intended as averaged over 5000 cycles. * Slight increase which is significant only after 6 months.

in [l/min], the temporal variable t in [s]. Mean, μ, and standard

Variable	NSR	AF	AF with normal LV contractility
P_{la}	$\mu = 9.12$, $\sigma = 0.74$	$\mu = 10.29$, $\sigma = 0.70$	$\mu = 9.16$, $\sigma = 0.75$
P_{laed}	$\mu = 8.71$, $\sigma = 0.05$	$\mu = 10.73$, $\sigma = 0.12$	$\mu = 9.59$, $\sigma = 0.08$
P_{laes}	$\mu = 10.06$, $\sigma = 0.10$	$\mu = 11.11$, $\sigma = 0.15$	$\mu = 10.08$, $\sigma = 0.15$
P_{lv}	$\mu = 43.23$, $\sigma = 45.18$	$\mu = 40.64$, $\sigma = 38.98$	$\mu = 45.21$, $\sigma = 45.37$
P_{lved}	$\mu = 11.25$, $\sigma = 0.40$	$\mu = 17.16$, $\sigma = 0.82$	$\mu = 17.23$, $\sigma = 0.94$
P_{lves}	$\mu = 100.18$, $\sigma = 0.78$	$\mu = 86.45$, $\sigma = 2.99$	$\mu = 96.76$, $\sigma = 2.83$
P_{ra}	$\mu = 7.90$, $\sigma = 1.56$	$\mu = 7.50$, $\sigma = 1.55$	$\mu = 8.06$, $\sigma = 1.71$
P_{raed}	$\mu = 7.70$, $\sigma = 0.10$	$\mu = 7.72$, $\sigma = 0.33$	$\mu = 8.29$, $\sigma = 0.54$
P_{raes}	$\mu = 10.41$, $\sigma = 0.09$	$\mu = 9.73$, $\sigma = 0.28$	$\mu = 10.56$, $\sigma = 0.32$
P_{rv}	$\mu = 13.33$, $\sigma = 8.84$	$\mu = 13.06$, $\sigma = 8.65$	$\mu = 13.53$, $\sigma = 8.78$
P_{rved}	$\mu = 10.48$, $\sigma = 0.13$	$\mu = 11.81$, $\sigma = 0.55$	$\mu = 12.66$, $\sigma = 1.21$
P_{rves}	$\mu = 19.38$, $\sigma = 0.32$	$\mu = 17.67$, $\sigma = 0.89$	$\mu = 18.00$, $\sigma = 0.89$
V_{la}	$\mu = 56.53$, $\sigma = 6.25$	$\mu = 65.95$, $\sigma = 4.64$	$\mu = 58.41$, $\sigma = 5.03$
V_{laed}	$\mu = 55.37$, $\sigma = 0.35$	$\mu = 68.84$, $\sigma = 0.80$	$\mu = 61.26$, $\sigma = 0.54$
V_{laes}	$\mu = 64.41$, $\sigma = 0.67$	$\mu = 71.41$, $\sigma = 1.00$	$\mu = 64.53$, $\sigma = 1.03$
V_{lv}	$\mu = 93.19$, $\sigma = 27.72$	$\mu = 108.76$, $\sigma = 23.43$	$\mu = 88.62$, $\sigma = 25.80$
V_{lved}	$\mu = 119.79$, $\sigma = 1.68$	$\mu = 126.93$, $\sigma = 5.03$	$\mu = 110.30$, $\sigma = 5.28$
V_{lves}	$\mu = 55.95$, $\sigma = 0.97$	$\mu = 79.72$, $\sigma = 7.34$	$\mu = 56.69$, $\sigma = 2.19$
V_{ra}	$\mu = 48.70$, $\sigma = 11.17$	$\mu = 47.36$, $\sigma = 10.34$	$\mu = 51.10$, $\sigma = 11.38$
V_{raed}	$\mu = 48.72$, $\sigma = 0.64$	$\mu = 48.77$, $\sigma = 2.20$	$\mu = 52.62$, $\sigma = 3.59$
V_{raes}	$\mu = 66.71$, $\sigma = 0.63$	$\mu = 62.22$, $\sigma = 1.88$	$\mu = 67.72$, $\sigma = 2.17$
V_{rv}	$\mu = 70.36$, $\sigma = 25.95$	$\mu = 62.90$, $\sigma = 22.42$	$\mu = 66.87$, $\sigma = 25.03$
V_{rved}	$\mu = 98.25$, $\sigma = 2.98$	$\mu = 81.90$, $\sigma = 8.27$	$\mu = 87.75$, $\sigma = 11.16$
V_{rves}	$\mu = 34.41$, $\sigma = 0.33$	$\mu = 34.69$, $\sigma = 8.27$	$\mu = 35.09$, $\sigma = 1.68$
P_{sas}	$\mu = 99.52$, $\sigma = 10.12$	$\mu = 89.12$, $\sigma = 9.10$	$\mu = 99.47$, $\sigma = 10.20$
$P_{sas,s}$	$\mu = 116.22$, $\sigma = 1.32$	$\mu = 103.66$, $\sigma = 3.00$	$\mu = 114.92$, $\sigma = 2.98$
$P_{sas,d}$	$\mu = 83.24$, $\sigma = 2.42$	$\mu = 77.24$, $\sigma = 5.18$	$\mu = 86.23$, $\sigma = 6.11$
P_p	$\mu = 32.99$, $\sigma = 1.13$	$\mu = 26.42$, $\sigma = 6.20$	$\mu = 28.69$, $\sigma = 3.54$
P_{pas}	$\mu = 20.14$, $\sigma = 4.00$	$\mu = 20.10$, $\sigma = 3.37$	$\mu = 20.15$, $\sigma = 3.78$
$P_{pas,s}$	$\mu = 26.73$, $\sigma = 0.22$	$\mu = 25.38$, $\sigma = 0.74$	$\mu = 26.03$, $\sigma = 0.84$
$P_{pas,d}$	$\mu = 14.27$, $\sigma = 0.39$	$\mu = 15.68$, $\sigma = 1.21$	$\mu = 15.21$, $\sigma = 1.41$
P_{svn}	$\mu = 13.89$, $\sigma = 0.16$	$\mu = 12.84$, $\sigma = 0.16$	$\mu = 14.04$, $\sigma = 0.19$
P_{pvn}	$\mu = 9.60$, $\sigma = 0.46$	$\mu = 10.72$, $\sigma = 0.45$	$\mu = 9.64$, $\sigma = 0.49$
SV	$\mu = 63.84$, $\sigma = 2.63$	$\mu = 47.21$, $\sigma = 8.32$	$\mu = 53.61$, $\sigma = 7.26$
EF	$\mu = 53.27$, $\sigma = 1.46$	$\mu = 37.12$, $\sigma = 6.01$	$\mu = 48.40$, $\sigma = 4.29$
SW	$\mu = 0.87$, $\sigma = 0.02$	$\mu = 0.57$, $\sigma = 0.14$	$\mu = 0.74$, $\sigma = 0.06$
CO	$\mu = 4.80$, $\sigma = 0.17$	$\mu = 4.38$, $\sigma = 0.67$	$\mu = 4.92$, $\sigma = 0.55$

Table 3.2. Mean (μ) and standard deviation (σ) values for the analyzed parameters. II column: NSR, III column: AF, IV column: AF without the reduced and variable LV elastance (i.e. $E_{lv,max} = 2.5$ mmHg/ml). The pressures P are expressed in [mmHg], the volumes V in [ml], the stroke volume SV in [ml], the ejection fraction EF in percentage, the stroke work SW in [J], the cardiac output CO in [l/min].

deviation, σ, values of the present simulations are summarized in Table 3.2 for all the variables here considered. Second column refers to the NSR, third column to the AF case, while fourth column refers to AF without the forced decrease of the LV elastance ($E_{lv,max}$ is constant and equal to 2.5 mmHg/ml).

Left heart pressures

The left atrial pressure increases during atrial fibrillation, by shifting its mean value from 9.12 mmHg (NSR) to 10.29 mmHg (AF). The range of values reached during AF is a bit less wide than in the normal case (AF σ=0.70, NSR σ=0.74). The PDFs of end-diastolic and end-systolic left atrial pressures (see Fig. 3.2b) also reveal that, during AF, end-diastolic and end-systolic pressure values are by far closer to each other than in the normal rhythm. The differences emerging in the temporal series of normal and fibrillated cases (see Fig. 3.2a) are mainly due to the passive atrial role. When the heartbeat is longer, P_{la} slowly increases until it almost reaches a plateau value. When instead the heartbeat is shorter, the pressure rapidly grows and no plateau region is observable.

A decrease of the left atrial pressure is found[43;161] after cardioversion in patients with AF, a result which is in agreement with the present observations.

During AF the left ventricular pressure reduces its mean value, from 43.23 mmHg (NSR) to 40.64 mmHg (AF), and the standard deviation value as well (NSR σ=45.18, AF σ=38.98). Lower maxima values in the fibrillated case are in general found (see Fig. 3.2c), while the longer the heartbeat, the higher is the next maximum value with respect to the previous one. For a long heartbeat the pressure remains constant for more than 50% of the RR interval, while for a short heartbeat a phase of constant pressure almost disappears.

The PDFs (see Fig. 3.2d, e) of end-diastolic and end-systolic pressure values show, during AF, an increase and a decrease, respectively. As for left atrial pressure, the fibrillated sequence tends to get the two values closer. In particular, the peak corresponding to the end-systolic pressure value shifts from 100 mmHg (NSR) to 87 mmHg (AF). By focusing on the end-diastolic left ventricular pressure, we observe an increase of its mean value during atrial

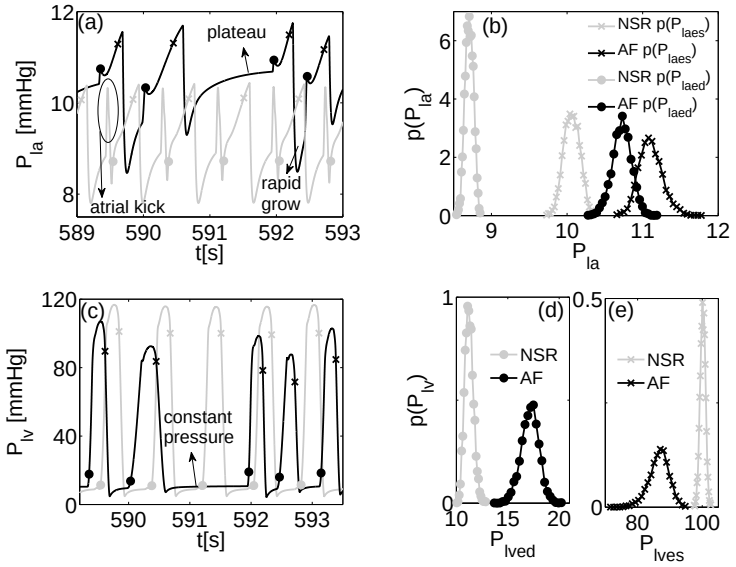

Figure 3.2. Left heart pressures: (a) left atrial pressure series, (b) PDFs of left atrial end-systolic and end-diastolic pressures. (c) Left ventricular pressure series, (d)-(e) PDFs of left ventricular end-diastolic and end-systolic pressures. Light: NSR, dark: AF. Symbols indicate end-systole (×) and end-diastole (•) values.

fibrillation: $\mu = 11.25$ mmHg (NSR), while 17.16 mmHg (AF). Although there is no clear evidence of the effects of AF on the left ventricular pressure (only one work[3] showed a decrease of the end-diastolic pressure during induced AF), an increase of the end-diastolic left ventricular pressure is in general a symptom of heart failure risk and ventricle dysfunction[109].

Right heart pressures

Even though the mean right atrial pressure is frequently reported to increase its mean value during atrial fibrillation[3;35;39;161], here we do not identify substantial differences with respect to the physiologic case, in terms of mean value (NSR μ=7.90, AF μ=7.50) and standard deviation (NSR σ=1.56, AF σ=1.55). The comparison of the time series in Fig. 3.3a mainly highlights the lack of the atrial kick in the fibrillated case. The PDFs of end-diastolic pressures confirm no strong differences in the mean values, while

the mean end-systolic pressure is shifted toward lower values during AF (see Fig. 3.3b). Both end-systolic and end-diastolic pressure PDFs present pronounced right tails during AF, meaning that higher maxima values are possible.

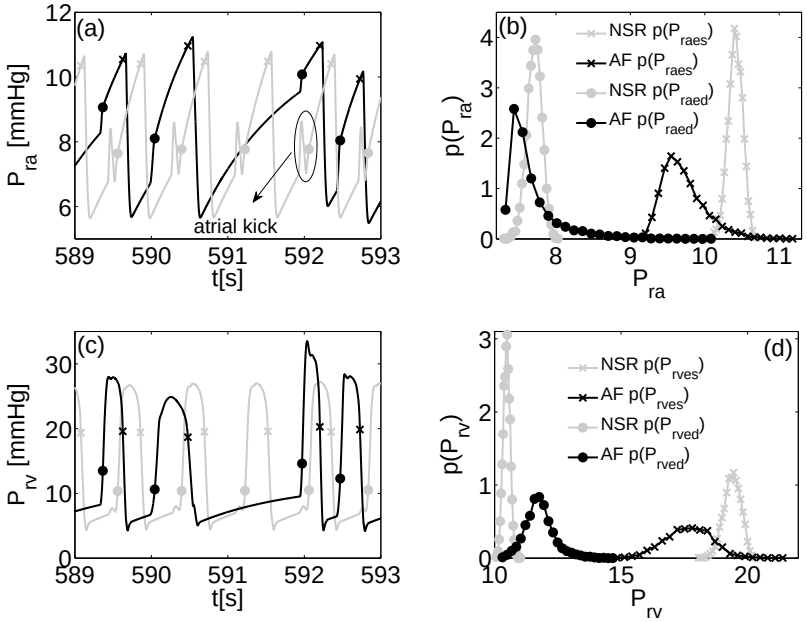

Figure 3.3. Right heart pressures: (a) right atrial pressure series, (b) PDFs of end-diastolic and end-systolic right atrial pressures. (c) Right ventricular pressure series, (d) PDFs of end-diastolic and end-systolic right ventricular pressures. Light: NSR, dark: AF. Symbols indicate end-systole (×) and end-diastole (•) values.

Probably due to the geometrical and structural complexity of the right ventricle[71] and to the difficulty of invasive measures, effects of AF in terms of right ventricular pressure are not easily available[71]. Although there are no significant variations of the two fundamental statistical measures (NSR: μ=13.33, σ=8.84; AF: μ=13.06, σ=8.65), an inspection of the temporal series (Fig. 3.3c) reveals that higher values are possible during AF. As for the left ventricle, higher maxima are more probable after a long heartbeat, while after a short heartbeat the maximum pressure value is usually lower than the previous one. When considering the end-diastolic pressure (Fig. 3.3d), an average increase is experienced

during atrial fibrillation (NSR μ=10.48, AF μ=11.81), with values that are much more spread out (NSR σ=0.13, AF σ=0.55). On the contrary, end-systolic pressure decreases during AF (NSR μ=19.38, AF μ=17.67), thereby getting closer to the end-diastolic mean value. The only available result come from induced AF[3], showing a decrease of the end-diastolic pressure.

Atrial Volumes

Atrial dilatation, together with systemic and pulmonary hypertension, is by itself one of the most important risk factors for AF[82;179]. For this reason, when looking at the available data in literature it is not easy to discern whether atrial enlargement is a cause or a consequence of atrial fibrillation.

In the present work, at least for the left atrium, we observe an average increase of the atrial volume during atrial fibrillation (NSR: μ=56.53, σ=6.25; AF: μ=65.95, σ=4.64), which is therefore here considered as a consequence of AF. This average enlargement is confirmed by higher average end-diastolic and end-systolic volumes (end-diastolic volumes: NSR μ=55.37, AF μ=68.84; end-systolic volumes: NSR μ=64.41, AF μ=71.41). Several results [1;165;172;178;198;199] agree with an increase of the left atrial (end-diastolic and end-systolic) volumes during AF. Only two works are not aligned, by remarking no substantial differences[126] or a decrease[35] of the left atrial volume when a fibrillated heartbeat is present.

Concerning the volumes of the right atrium, during atrial fibrillation we observe a small decrease of the mean (NSR: μ=48.70, AF: μ=47.36) and end-systolic (NSR: μ=66.71, AF μ=62.22) values, while the end-diastolic volume remains unvaried (NSR: μ=48.72, AF: μ=48.77). Right atrial volume is rarely measured during atrial fibrillation and sometimes only to assess the effects of varying volume loading conditions and heart rate[199]. A statistically significant decrease of right atrial end-diastolic and end-systolic volumes after cardioversion was found only after 6 months[178].

Ventricular Volumes

End-systolic and end-diastolic left ventricle volume data are not often offered in the atrial fibrillation literature, maybe because the

related ejection fraction better synthesizes a similar kind of information. The available results show an increase of both end-diastolic and end-systolic volumes during atrial fibrillation[6;178], while in one case no significant variations are encountered[126]. Here we find an increase of the mean values of end-diastolic (EDV) and end-systolic (ESV) volumes during atrial fibrillation (EDV: NSR μ=119.79, AF μ=126.93; ESV: NSR μ=55.95, AF μ=79.72), as well as an increase of the mean left ventricle volume (NSR μ=93.19, AF μ=108.76). The shifts of the EDV and ESV toward higher values during atrial fibrillation are clearly detectable by the PDFs reported in Fig. 3.4c. Braunwald et al.[22] found a direct proportion between the end-diastolic volume and the heartbeat length (RR). This relation can be verified by considering the fibrillated temporal series in Fig. 3.4a. The left ventricle is overfilled when the beat is long, while is under-filled when the beat is short. Figure 3.4f shows the relation $V_{lved}(RR)$, confirming the positive correlation between RR and V_{lved}.

During atrial fibrillation the right ventricle experiences, with less data dispersion (coefficient of determination, R^2=0.99), a filling dynamics similar to the left ventricle: overfilling occurs for long beats, while under-filling follows a short heartbeat (Fig. 3.4b, g). The PDFs reveal that end-systolic values are more spread out maintaining the mean value of the NSR, while end-diastolic volume decreases even if during atrial fibrillation important overfilling are possible (see Fig. 3.4d, e). The mean RV volume is lower than in normal conditions (NSR μ=70.36, σ=25.95; AF μ=62.90, σ=22.42). Although not included as a common effect of atrial fibrillation, the combined action of irregular heartbeat and overfilling can compromise the right ventricle function[71]. Due to the complex geometrical shape, the right ventricle volume is not easily estimated. Recent magnetic resonance images[178] show, after cardioversion, a slight decrease of right ventricle (end-systolic and end-diastolic) volumes which is significant only considering a six-month follow-up.

Systemic and Pulmonary Arterial Pressures

Systemic and pulmonary arterial pressures are perhaps the most controversial hemodynamics variables regarding the effects of atrial

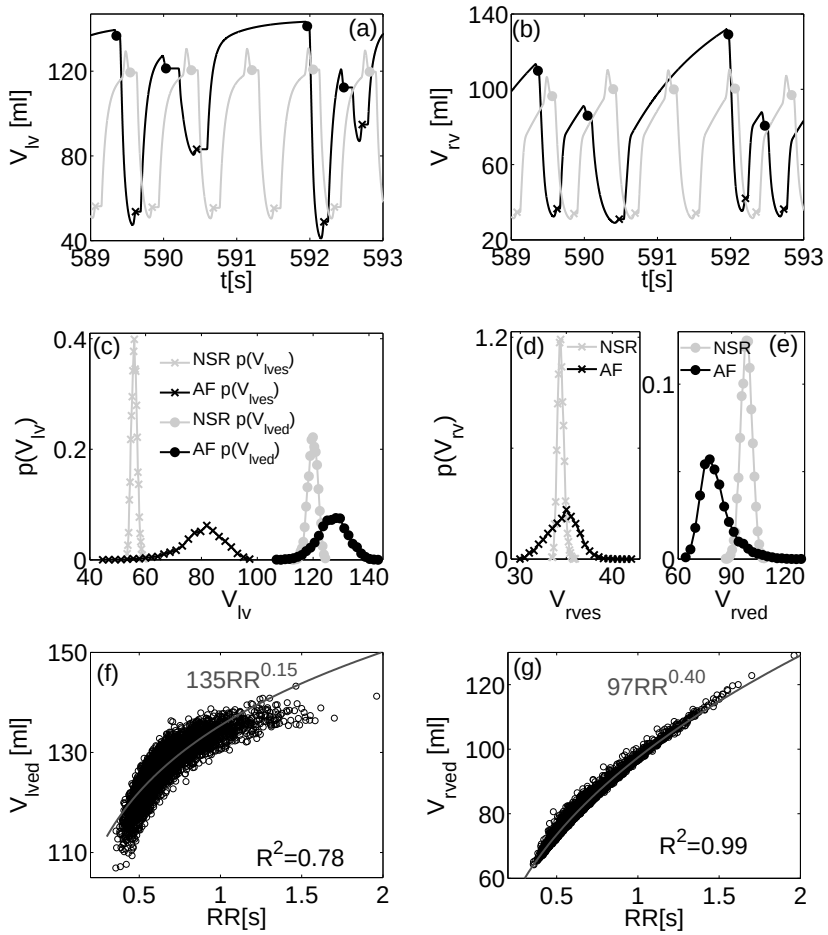

Figure 3.4. (a),(c),(f) Left ventricular volume: (a) temporal series, (c) PDFs of end-systolic and end-diastolic left ventricular volumes. (f) AF: left ventricle end-diastolic volume (V_{lved}) as function of RR. (b),(d)-(e),(f) Right ventricular volume: (b) temporal series, (d)-(e) PDFs of end-systolic and end-diastolic right ventricular volumes. (g) AF: right ventricle end-diastolic volume (V_{rved}) as function of RR. (f),(g) Power-law fittings of the data and coefficients of determination, R^2, are introduced. Light: NSR, dark: AF. Symbols indicate end-systole ($\times$) and end-diastole ($\bullet$) values.

fibrillation. The first reason is that systemic hypertension is among the most common risk factors inducing atrial fibrillation[82;184]. More

recently, AF has been reported in patients with pulmonary hypertension[151]. Therefore, it is not straightforward to identify the specific role of AF on systemic and pulmonary pressure levels. Secondly, systemic arterial pressure is in general variable during AF, and often difficult to estimate as the irregular heartbeat causes problems for non-invasive blood pressure measurements. Because of the beat-by-beat variability, the heart's efficiency and performance can be reduced, leading to a consistent decrease of the blood pressure. In this context, hypotension is more worrying than hypertension.

The variability of systemic arterial pressure is present in the literature of fibrillated data. During AF no substantial differences in terms of systolic, diastolic and mean pressures are displayed[3;39], in particular when patients are not affected by other pathologies [85]. An increase of these quantities is instead registered by Giglioli et al.[61]. Furthermore, Kaliujnaya *et al*[81] showed an increase of diastolic and systolic pressure, along with a decrease of the pulsatile pressure.

We notice a decrease of the mean and standard deviation values of the systemic arterial pressure during atrial fibrillation (NSR: μ=99.52, σ=10.12; AF: μ=89.12, σ=9.10), which is in agreement with the common sign of hypotension caused by a decreased cardiac output[42;138]. The average decrease is accompanied by a decrease of the mean systolic (NSR μ=116.22, AF μ=103.66, see Fig. 3.5b), diastolic (NSR μ=83.24, AF μ=77.24, see Fig. 3.5b), and pulsatile (NSR μ=32.99, AF μ=26.42) pressures. The arterial pulse pressure, P_p=$P_{syst} - P_{dias}$, is the variable which is mostly affected by the variability of the heartbeat (NSR σ=1.13, AF σ=6.20), reaching values that oscillate from 10 to 50 mmHg (in the normal case, P_p varies from 29 to 36 mmHg). The analysis of the fibrillated time series (Fig. 3.5a) highlights that the pulsatile pressure amplitude, $P_p(RR)$, increases with the length of the preceding heartbeat, $RR1$, while decreases with the increase of the pressure amplitude of the preceding beat, $P_p(RR1)$. These findings are summarized in Fig. 3.5 (panels c and d), and confirm what observed by Dodge *et al*[52].

As the systemic pressure, the pulmonary arterial pressure suffers from the same variability of registered data during fibrillation events. The mean value remains unchanged during atrial fibrillation (NSR: μ=20.14, AF μ=20.10), in line with the findings of

Resnekov *et al*[143] and Shapiro and Klein[161]. An increase is instead displayed by the results of Alboni *et al*[3] and Clark *et al*[39]. Systolic pressure decreases (NSR μ=26.73, AF μ=25.38, see Fig. 3.5f). Chirillo *et al*[35] and Clark *et al*[39] register an increase, while Alboni*et al*[3] do not measure significant variations. Diastolic pressure increases during atrial fibrillation (NSR μ=14.27, AF μ=15.68, see Fig. 3.5f), and this result aligns with all the other available data [3;35;39]. Both systolic and diastolic pressure values are more spread out during AF (see Fig. 3.5f). The temporal dynamics is analogous to the arterial systemic pressure (Fig. 3.5e): a large pulsatile pressure amplitude is due to a long preceding heartbeat and is followed by a smaller pressure amplitude.

Pulmonary and Systemic Vein Pressures

The pulmonary capillary wedge pressure (or pulmonary vein pressure) is an indirect estimate of the left atrium pressure, usually obtained with an invasive catheterization through right atrium, right ventricle and pulmonary artery. Mitral valve stenosis and mitral regurgitation as well as aortic valve stenosis and aortic regurgitation can elevate the left atrium pressure, which almost fully transmits back this increase to pulmonary capillaries. During AF an increase of the pulmonary vein pressure is observed by several studies[3;35;39], while no particular differences emerge from others [47;126]. An increase of the mean pulmonary vein pressure is confirmed by the present data (NSR μ=9.60, AF μ=10.72), and is in agreement with an increase of the left atrium pressure (see Section 3.1).

The systemic vein pressure (also referred to as central venous pressure) estimates the pressure in the thoracic vena cava and approximates the right atrial pressure. As for this latter variable, the systemic vein pressure decreases during atrial fibrillation (NSR μ=13.89, AF μ=12.84). To the best of our knowledge, no data treat the effects of atrial fibrillation on the systemic vein pressure.

Stroke Volume and Ejection Fraction

The stroke volume, SV, is the difference between end-diastolic and end-systolic ventricular volumes and here is used to represent the volume of blood pumped from the left ventricle with each beat,

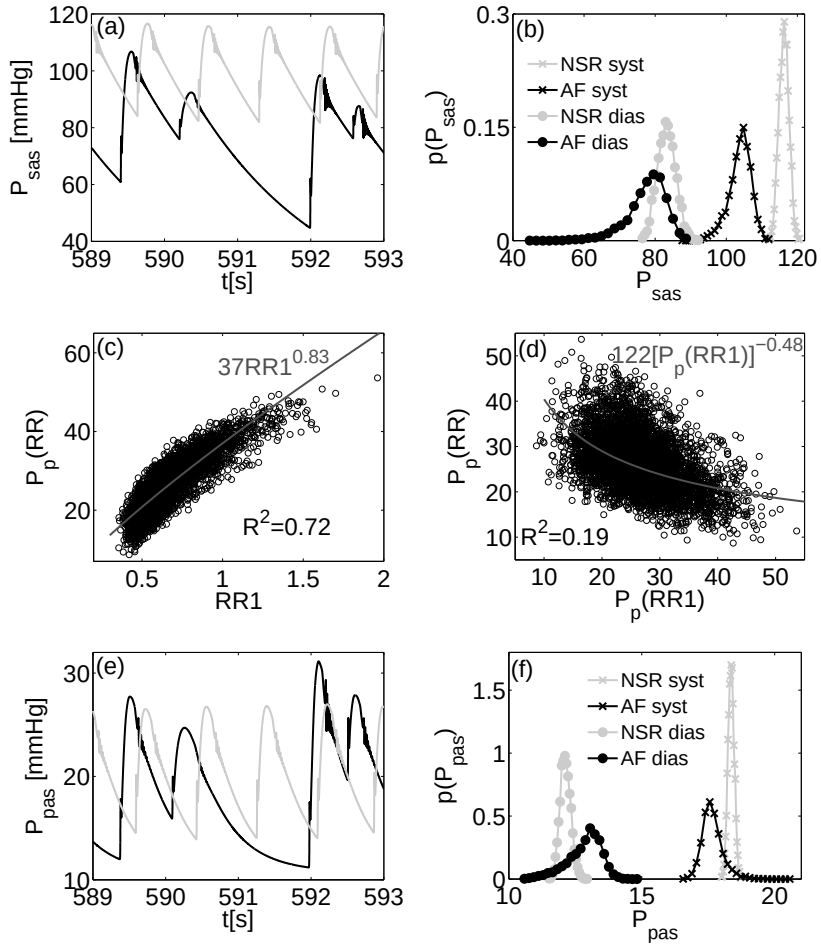

Figure 3.5. (Top) Systemic arterial pressure: (a) temporal series; (b) PDFs of systolic and diastolic pressures. (Middle) AF pulsatile arterial pressure, power-law fittings of the data and coefficients of determination, R^2, are provided: (c) amplitude, $P_p(RR)$, as a function of the preceding heartbeat, $RR1$; (d) amplitude, $P_p(RR)$, as a function of the pulsatile pressure of the preceding beat, $P_p(RR1)$. (Bottom) Pulmonary arterial pressure: (a) temporal series, (b) PDFs of systolic and diastolic pressures. Light: NSR, dark: AF.

SV=$V_{lved}-V_{lves}$. SV coincides with the integral of the flow across the aortic valve.

There is almost unanimity among the collected data in literature saying that atrial fibrillation reduces the stroke volume [3;43;61;72;156]. The relative increase of SV when passing from AF to NSR is up 40% [43;61;72] and in one case is around 30% [156]. Only Killip et al. [85] found no substantial differences with respect to the normal conditions.

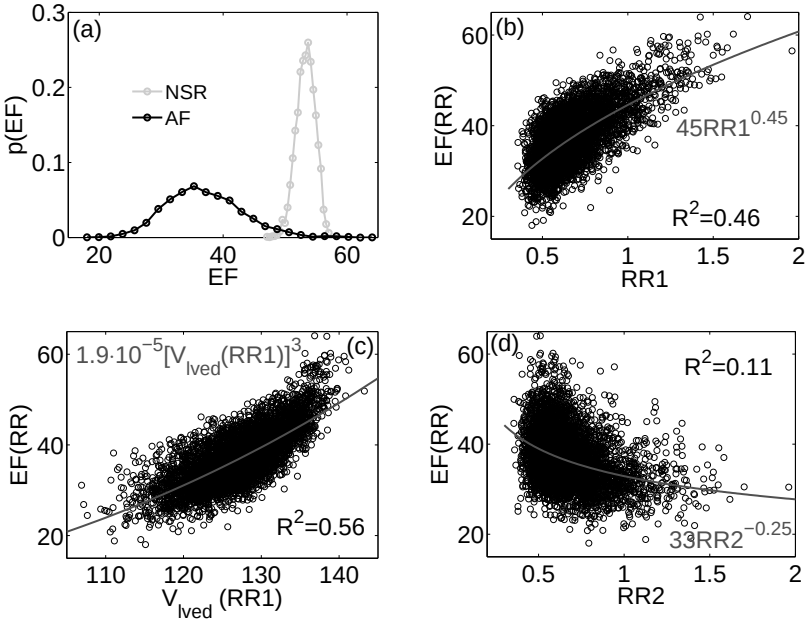

Figure 3.6. Ejection fraction. Power-law fittings of the data and coefficients of determination, R^2, are added in panels (b), (c), (d). (a) Ejection fraction PDFs. (b) AF: ejection fraction, $EF(RR)$, as a function of the preceding beat, $RR1$. (c) AF: ejection fraction, $EF(RR)$, as a function of the end-diastolic volume of the preceding beat, $V_{lved}(RR1)$. (d) AF: ejection fraction, $EF(RR)$, as a function of the pre-preceding beat, $RR2$. Light: NSR, dark: AF.

The present results fully agree with the measured data in literature: from a fibrillated to a normal condition there is a relative increase of SV of about 35% (average SV: NSR μ=63.84, AF μ=47.21). The standard deviation of the stroke volume is much higher during atrial fibrillation (NSR σ=2.63, AF σ=8.32), due to the ejection variability introduced by the irregular heartbeat(see

the PDF in Fig. 3.6a). Greenfield et al.[64] discovered that an inverse relation between stroke volume, $SV(RR)$, and the heart rate of the preceding beat, $HR(RR1)$, exists, a trend which is positively verified by our results (see Fig. 3.6b).

The same concordance found for the stroke volume is encountered in literature regarding the ejection fraction. We recall that the ejection fraction is the fraction of blood ejected into the systemic circulation by the left ventricle relative to its end-diastolic volume, $EF=(SV/V_{lved})/100$. Apart from one case[199] where no variation is found for the EF, all the other results[6;35;60;178;198] agree in observing a decrease of the EF during atrial fibrillation.

We are in agreement with the literature data, by noting a decrease of mean EF during atrial fibrillation, from EF=53.27% (normal case) to EF=37.12% (fibrillation), with values that are much more spread out (NSR: σ=1.46, AF σ=6.01, see also the PDF reported in Fig. 3.6a). Gosselink *et al.*[62] determine an ejection fraction of about 34% during atrial fibrillation, evidencing a positive correlation between $EF(RR)$ and $RR1$ (length of the preceding beat), and between $EF(RR)$ and the end-diastolic volume of the preceding beat, $V_{lved}(RR1)$. The same correlations are obtained by Muntinga et al.[114], and here furthermore confirmed (see Fig. 3.6b and 3.6c). Gosselink*et al.*[62] also recognize a negative correlation between $EF(RR)$ and the pre-preceding beat, RR2, a trend which is in qualitative accordance with the present outcomes (Fig. 3.6d), despite their sparsity as highlighted by a low coefficient of determination, R^2=0.11.

Stroke Work, Pressure-Volume Loop and Cardiac Output

Stroke work, SW, represents the work done by the left ventricle to eject a volume of blood (i.e., stroke volume) into the aorta, and quantifies the amount of energy converted to work by the heart during each heartbeat. The left ventricle stroke work is computed at every heartbeat as the area within the left ventricle pressure-volume loop.

Available results on stroke work show a decrease during atrial fibrillation[84;126]. The relative decrease with respect to the normal rhythm is about 14%[126]. The stroke work here measured show a mean value of μ=0.87 J in the normal case, and μ=0.57 J in the

fibrillated case, leading to a relative decrease of about 34% during AF. The standard deviation is about one order of magnitude larger when beats are irregular (NSR σ=0.02, AF σ=0.14). Stroke work slightly varies during NSR, while wide oscillations are possible during fibrillation events (Fig. 3.7a). A direct proportionality between $SW(RR)$ and the preceding heartbeat, $RR1$, was found [52], and here ascertained as well (Fig. 3.7b).

Left ventricle pressure-volume loops of 5000 cycles are reported for both NSR and AF in Fig. 3.7, panels (c) and (d), respectively. Vertical lines represent the mean end-systolic and end-diastolic LV volumes. Reverse flow evidenced by the lower right corner and upper left corner of the PV-loop is due to heart valve modelling [89], accounting for the influence of the blood pressure effect, the friction effect from the tissue, and from blood motion. The PV loop markedly reduces during AF, as already observed through the SW and also reported in literature[23], while PV values are more spread out during the 5000 fibrillated cycles.

The cardiac output, defined as the volume of blood being pumped by the left ventricle in the time interval of one minute, $CO{=}SV \times HR$, is probably the most evaluated variable to quantify to impact of atrial fibrillation and several data are present in literature. A great part of these deals with measures before and after cardioversion (or catheter ablation), showing a consistent recovery of cardiac output when the normal sinus rhythm is established again[35;47;63;72;84;85;112;126;138;156;180]. In absence of other important pathologies, the relative increase with respect to pre-treatment configuration (that is, fibrillated conditions) varies in the range $7 - 13\%$ for the great majority of authors[35;43;47;85;126;156], while value of 18%[39] and more than 50%[72;180] have been also reported. Furthermore, only few studies[3;61;143;161] encounter no meaningful changes in terms of cardiac output between normal and fibrillated heartbeats.

The present outcomes align with the findings in literature: for the cardiac output there is a relative increase, when passing from fibrillation to normal rhythm, which is around 9.5% (NSR μ=4.80, AF μ=4.38). The decrease of mean cardiac output during AF is accompanied with an increase of the standard deviation (NSR σ=0.17, AF σ=0.67), leading to a wider PDF (see Fig. 3.7c). We can detect a positive correlation between the cardiac output,

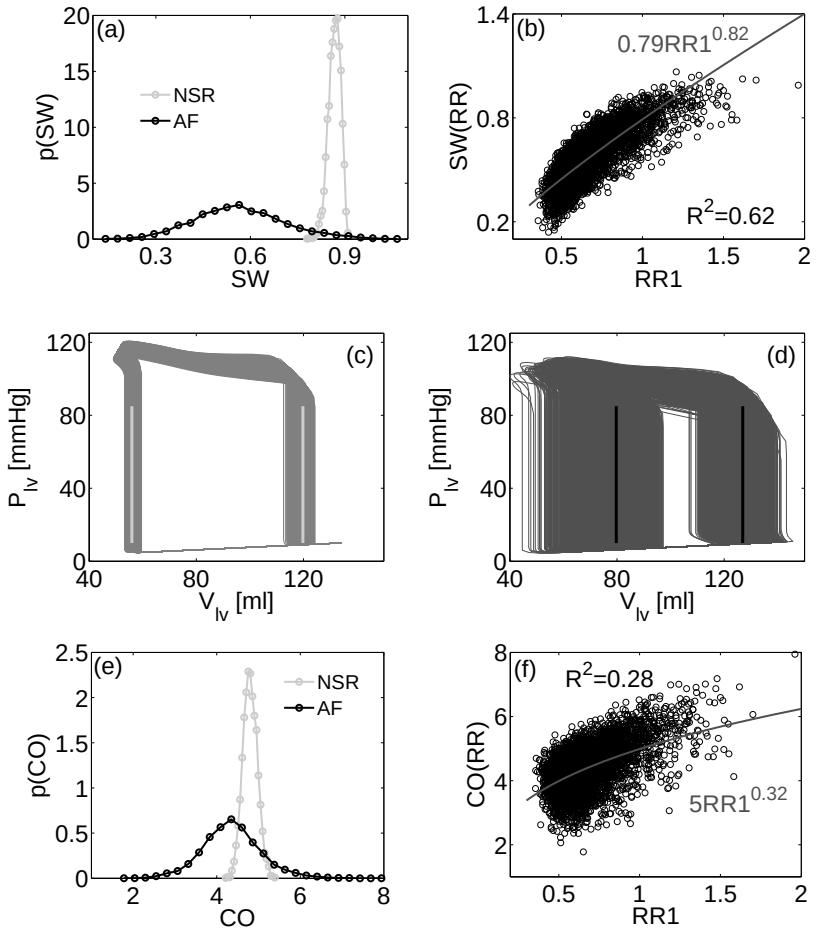

Figure 3.7. (Top) Stroke Work: (a) PDFs; (b) AF stroke work, $SW(RR)$, as a function of the preceding heartbeat, $RR1$. (Middle) Pressure-volume loops of 5000 cycles: (c) NSR, (d) AF. Vertical lines represent the mean end-systolic and end-diastolic LV volumes. (Bottom) Cardiac Output: (e) PDFs; (f) AF cardiac output, $CO(RR)$, as a function of the preceding heartbeat, $RR1$. (b)-(f) Power-law fittings of the data and the coefficients of determination, R^2, are included. Light: NSR, dark: AF.

$CO(RR)$, and the preceding heartbeat, $RR1$ (see Fig. 3.7d). However, the data sparsity around short beats indicates that the presence of rapid beats is not sufficient, by itself, to reduce the cardiac

output during atrial fibrillation.

The contemporary decrease of stroke work and cardiac output confirms that during atrial fibrillation the left ventricle experiences a reduced efficiency and performance.

3.1.2 Discussion

To better understand which hemodynamic changes are dominated by the forced decrease of the LV contractility and which changes do occur due to the heart rate variability, a fibrillated simulation with normal LV contractility ($E_{lv,max} = 2.5$ mmHg/ml constant) is performed. Results in terms of mean and standard deviation values are summarized in the fourth column of Table 3.2. Trying to extract synthetic information from this new simulation, we observe that the changes mainly controlled by the heart rate variability involve the following variables: ejection fraction, stroke volume, stroke work, pulmonary arterial pressure, LA volume, LV pressure, RV pressure and volume. In fact, for these parameters the trends of the variations occurring during AF with reduced contractility with respect to NSR are confirmed by the AF simulation with normal contractility. On the contrary, changes related to RA volume and pressure, LV volume, systemic arterial pressure and cardiac output, are mainly driven by the reduced contractility. For example, indeed, the reduced LV contractility is the main responsible of the cardiac output drop. When the contractility is normal, the accelerated HR makes the cardiac output even increase. It should be noted that dividing the contributions of reduced contractility and heart rate variation is not always straightforward: while during AF the reduced LV contractility enhances a general increase of the LV volumes, the reduction of quantities related to the LV volumes, such as SV and EF, is in large part imputable to the irregular beating.

This work represents a first attempt to quantify, through a stochastic modelling, the role of acute AF on the whole cardiovascular system, thereby leading to a double advantage. First, atrial fibrillation conditions have been analysed without the presence of other pathologies (e.g., hypertension, atrial dilatation, mitral regurgitation), which can all concur to affect the hemodynamic

response. In this regard, our findings about moderate systemic hypotension and left atrial enlargement should be interpreted as pure consequences of AF alone and not induced by other pathologies. In particular, the reduced LV contractility promotes a reduction of the systemic arterial pressure, while the atrial enlargement is first due to the heart rate variability. Second, the main cardiac variables and hemodynamic parameters can all be obtained at the same time, while clinical studies usually focus only on a few of them at a time.

The present outcomes have been compared with more than thirty clinical measures regarding AF. Although literature frequently offers data which are in contrast one with the other (e.g., systemic arterial pressure), the overall agreement is quite remarkable.

Reduced cardiac output with correlated drop of ejection fraction and decreased amount of energy converted to work by the heart during blood pumping, as well as higher left atrial volume and pressure values are some of the most representative outcomes aligned with literature and here emerging during AF with respect to NSR. Keeping in mind the different nature of measurements and clinical conditions, we here quantitatively compare (in terms of mean values) the present results with the ranges of some specific data available in literature for the most commonly measured hemodynamic parameters:

- P_{pvn}: present results (NSR: 9.60 mmHg, AF: 10.72 mmHg). Literature data[3;35;39;47;126] (NSR: [8÷19] mmHg, AF: [12÷21] mmHg).

- SV: present results (NSR: 63.84 ml, AF: 47.21 ml). Literature data[61;72;85] (NSR: $[68 \div 70]$ ml, AF: $[49 \div 62]$ ml).

- EF: present results (NSR: 53.27%, AF: 37.12%). Literature data[6;35;60;178;198;199] (NSR: $[41\% \div 60\%]$, AF: $[12\% \div 52\%]$).

- CO present results (NSR: 4.80 l/min, AF: 4.38 l/min). Literature data[35;39;47;61;72;112;161] (NSR: $[4.1 \div 6.2]$ l/min, AF: $[3.8 \div 5.1]$ l/min).

As can be observed, the values predicted by the present model fall within the typical ranges observed by in vivo measurements.

3.1.3 Limitations

Limiting aspects of the study are the absence of short-term regulation effects of the baroreceptor mechanism, which can act in order to restore the hemodynamic parameters toward normal values. The present model only represents acute episodes of AF lasting less than 24 hours, while the anatomical remodelling due to the effects of AF in the long-term is neglected. For this reason, effects and underlying structural changes due to persistent or chronic AF are not taken into account here. In the meantime, a clear distinction between acute and chronic hemodynamic effects of AF in clinical measurements is not possible. Literature data are contemporary affected by short and long time feedbacks and compared with our outcomes, accounting solely for the early mechanical response of the system to isolated AF events.

Moreover, here we have focused on the unimodal RR distribution only, while a broader inspection of multimodal distributions could give a more complete overview of the cardiovascular response to AF.

Regarding some more specific aspects of the modelling, a few results on the right heart behaviour do not fully agree with the *in vivo* scenario, and this is probably due to the fact that the reduced contractility of the right ventricle and the ventricular interaction (here both neglected) should be properly accounted for. In the present work, the pulsatility properties of the heart are modelled by means of the time-varying elastance. This approach only phenomenologically accounts for the local Starling mechanism. Moreover, we have exclusively focused on the relation between elastance, the reduced contractility due to AF and the beating interval, RR. Other existing dependencies (e.g., on the patient disease condition) are not considered.

Chapter 4

Results from the multi-scale model

This Chapter aims to describe the results obtained through the use of the multi-scale mathematical model presented in Section 2.2..

In the first Section, the model is firstly semi-quantitatively validated against up-to-date literature data. Afterwards, in second Section, a first subject-specific validation is carried out by developing a new setting procedure. Pressure at ascending aorta, brachial, radial, femoral and posterior tibial, along with maximum and minimum left-ventricular volume and ejection fraction, have been checked in a group of six young healthy volunteers. Later on, after the encouraging results of the precedent work, the subject-specific setting procedure has been improved, becoming fully deterministic and avoiding uneasy and unnecessary measurements for input determination. In third Section subject-specific results, obtained from the multi-scale model and its setting procedure, are compared with central pressure esteems obtained from reference commercial instrument in a population of around 50 young healthy subjects. Finally, fourth Section present a wide study of the fluid mechanics of an ageing cardiovascular system. Starting from reference literature data an age-dependent model characterization is described. The analysis of the obtained results gives an embracing description of the most important phenomena: pulse wave propagation, reflection, re-reflection, pulse pressure amplification, transit time, and the role of the left-ventricle.

4.1 Semi-quantitative validation

In this Section a semi-quantitative comparison of the model outcomes with the characteristic behaviour of the cardiovascular system is described.

Figure 4.1 shows that the model gives a left-ventricular pressure-volume loop in agreement with the typical physiological values[70]. A cardiac output of 4.4 l/min, an ejection fraction of 53 %, and an emptying during the first third of the ejection time equal to 65 % testify the good performance of the model[70].

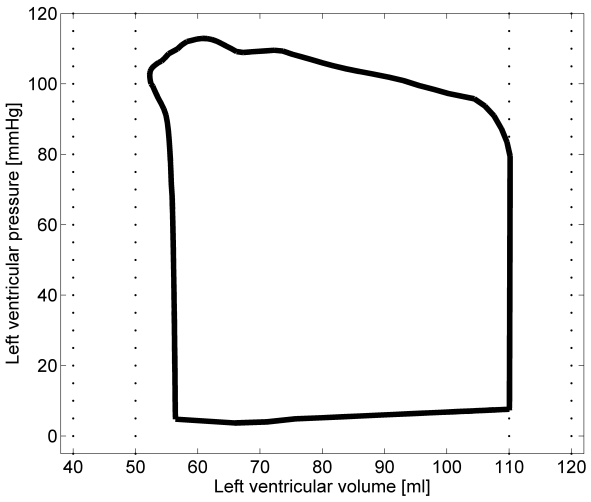

Figure 4.1. Left-ventricular pressure-volume loop. The vertical lines mark the typical physiological ranges[70].

Flow and pressure conditions at the aortic valve are reported in figure 4.2.

A well-known characteristic of the flow through aortic valve is that an amount of backflow accompanies the leaflet closing movement, due to the interactions among the pressure gradient, mechanical response of leaflet tissues, and vortices in the Valsalva sinuses. Once the valve is closed, the backflow determines a local instantaneous increase of pressure, called dicrotic notch or *incisura*, which then propagates forward. All these features are well reproduced by the model: negative values of the flow clearly occur at the closing

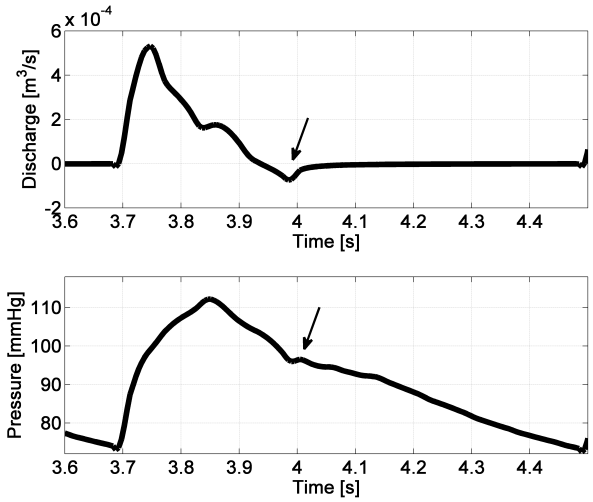

Figure 4.2. Flow (top) and pressure (bottom) through the aortic valve. The backflow and the consequent rise of the local pressure are marked with arrows.

time, while aortic pressure exhibits the consequent increase in pressure. The backflow that accompanies valve closing is also evident in the upper left corner of the loop of figure 4.1, where a small increase of volume occurs in the early relaxation phase.

The periodic left-ventricular ejection induces pressure and flow waves that propagate and reflect along the arterial tree. In figure 4.3 some model results are presented. As expected, the central pressure varies between about 80 to 120 mmHg [70]. Figure 4.3 shows that pressure waves properly become steeper and increase in amplitude during propagation, while their celerity changes [183]. Model simulations give a mean pulse wave celerity around 3.7 m/s in the ascending aorta, 4.2 m/s in the thoracic aorta, 5.2 m/s at the iliac bifurcation, 7 m/s in the femoral artery, and of 8.5 m/s in the posterior tibial. Both values and the increasing trend moving away from the aortic arch are in agreement with typical physiological data [70].

Even flow wave propagation matches very well the physiological behaviour, exhibiting the typical amplitude reduction [139]. This latter is due to (i) the compliance of the arteries, which accommodates flow during the systolic phase, (ii) the inertial forces, which

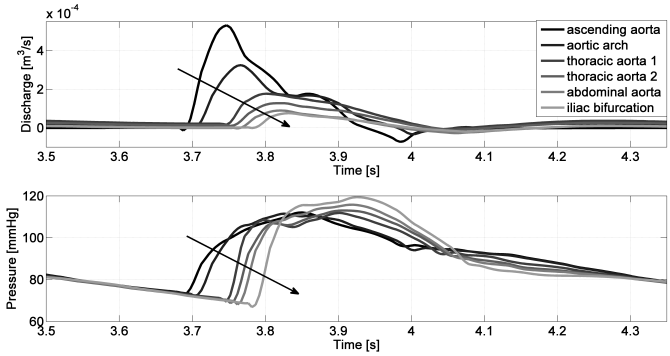

Figure 4.3. Flow (top) and pressure (bottom) at different sites along the aorta. The arrows indicate the increasing distance from the heart.

limit blood accelerations, and (iii) the bifurcations, where the flow divides in different branches.

4.2 Subject-specific validation: small subject set

Due to experimental and clinical difficulties, few studies reported a validation of the cardiovascular models. Some authors validated their model predictions using a mock circulatory loop[24;78], while others used an *in vitro* realistic model of the main arteries[2;107]. Very few validations have been carried out against *in vivo* measurements on humans: a local arm model was validated in the ARCH Consortium project[27]; Reymond *et al.*[145] described a statistically-based semi-quantitative validation; Olufsen *et al.*[125], Reymond *et al.*[144], and Bollache *et al.*[20] quantitatively validated their models by a subject-specific analysis. However, all the *in vivo* validations were carried out by imposing a measured inflow condition, thus decoupling heart and arterial tree modelling. Finally, Reymond *et al.*[144] invoked the development of a procedure that "personalizes to some extent the generic arterial tree based on fewer and clinically feasible measurements".

In this Section we propose an effective procedure for subject-specific model setting and we validate it against a small population of six young healthy subjects.

4.2.1 Measurements on the population

The population consisted of six healthy male 24 ± 1 years old subjects. The clinical work was done at the "Città della Salute e della Scienza" Hospital in Turin, at the Echocardiography laboratory of the Hypertension Center, Department of Medical Sciences, University of Turin; the study was approved by the local ethical committee, protocol number CEI/330; all subjects gave informed consent to the approved study. To check model outcomes in different body areas, blood pressure was measured (3 times at 2 minutes interval) using a validated automatic oscillometric device (Omron Matsusaka Co, Kioto, Japan) at the brachial artery level. Brachial, radial, femoral and posterior tibial pressure signals were evaluated by means of a high fidelity tonometric device (SPC 301, Millar Instruments, Houston, TX, USA). Calibration of tonometric waveforms were carried out with systolic and diastolic values

recorded with the oscillometric device. Central pressures were estimated by means of SphygmoCor System (Atcor Medical, Sydney, Australia). All measurements were made with subjects in a stationary supine position. Left ventricular volumes were obtained by transthoracic echocardiography from apical 4Ch and 2Ch views or from 3D echocardiography whenever possible: end diastolic (EDV) and end systolic volumes (EDV) were evaluated by the Simpson's disks method and stroke volume (SV) was calculated as the difference between these values; ejection fraction (EF) was computed as SV/EDV*100. Heart rate (HR), ejection time (ET), preejection time (PET) and activation time (t_{ce}) (i.e., the Q-T interval [70]) were evaluated from the analysis of the ECG, recorded simultaneously to flow velocity by Pulsed Doppler at the level of the left ventricular outflow tract in apical 5Ch view. For each individual, height and weight were measured and the body mass index, BMI_{PT}, was evaluated. Mean pulse wave velocities were measured between carotid and both femoral and radial and between femoral and posterior tibial arteries by foot-to-foot method. Briefly, pulse wave velocity was obtained as time leg between transcutaneously obtained pressure divided by measured distance between the two recording sites. The measured quantities are listed in table 4.1.

Inclusion criteria were male sex, age and no relevant health issue after outpatient clinical evaluation. Subjects with measured blood pressure values higher than 140/90 mmHg were excluded. Whenever a diagnosis of hypertension was suspected, a 24 hours blood pressure monitoring was required and performed.

4.2.2 Setting of the model parameters

In order to describe a specific subject a number of model parameters were tuned starting from *in vivo* measurements. The parameters underlying the subject-specific calibration were: length, diameter and mechanical properties of the arterial vessels, heart rate, left-ventricle contraction time, mean left atrial pressure, maximum myocardial force of contraction, and overall peripheral resistance. Subject-specific parameters were obtained by multiplying the corresponding values reported in the reference data set used in the

Table 4.1. Measured values for each individual of the population. Pressure is expressed in mmHg. P. Tibial stands for posterior tibial. $\bar{Q}$ is the mean aortic valve outflow.

	Subjects					
	1	**2**	**3**	**4**	**5**	**6**
Height [m]	1.71	1.79	1.80	1.74	1.75	1.83
Weight [kg]	58	89	80	65	72	77
BMI_{PT} [kg/m^2]	19.8	27.8	24.7	21.4	23.5	23.0
HR [bpm]	60	60.5	60	83	67.5	57
$t_{ce}[s]$	0.415	0.407	0.388	0.320	0.402	0.465
PET [s]	0.057	0.059	0.054	0.050	0.056	0.062
ET [s]	0.286	0.333	0.325	0.251	0.296	0.310
EDV [ml]	107	149	103.5	87	97	135
ESV [ml]	48	87	43.5	39	45	62
SV [ml]	59	62	60	48	52	73
EF [%]	55	58	56	56	54	54
$\bar{Q}$ [l/min]	3.76	5.00	3.60	4.00	3.30	4.16
Central pressure	105.5/69	105/67	90/56	115/80.5	101/65	98/63
Brachial pressure	115/60	129/65	115/51	140/80	120/65	116/64
Radial pressure	120/68	128/66	115/55	140/80	120/65	118/63.5
Femoral pressure	116/68	125/60.5	101/48	124.5/76	114/59	116/65
P. Tibial pressure	116/66	124.5/64	115.5/54	120/70	109/60	115.5/68

general result section (see Reymond *et al.*[145]) by suitable subject-specific corrective coefficients η_i as reported in the following procedure (subscript i specifies the parameter considered).

(a) The arterial lengths strongly correlate with the individual height[78;167]. Therefore, the corrective coefficient η_L was calculated as the ratio between the subject height and an average height assumed equal to 1.75 m.

(b) Arterial diameter correlates with several characteristics, like age, sex, race, height, weight, body mass index (BMI), and hypertensive condition[49;73;91;152]. We focused on BMI because (i) individuals considered in the validation share the same age, sex and race, (ii) no hypertensive subjects are included, and (iii) BMI is very often related to the arterial diameter[91]. We analyzed several literature data[46;49;73;91;152;194;203] and found that the ratio between the diameter and BMI variations (with respect to the mean values) is almost constant and is approximately equal to a=0.0056 m^2/kg.

It follows that the corrective coefficient for the diameter results

$$\eta_D = 1 + a\,(\mathrm{BMI}_{pt} - \mathrm{BMI}_{ref}) \tag{4.1}$$

where the reference value BMI_{ref} is assumed to be 22 kg/m^2.

(c) Subject-specific mechanical properties of the arterial wall were determined in the following way. Real pressure wave velocities were assessed from pressure signals measured along the main arterial paths and using ECG as a time reference. The ratios of such velocities to the corresponding ones predicted by the model (using the typical data set), were averaged to obtain the subject-specific corrective coefficient η_W. Finally, coefficients B_i of each artery were modified accordingly.

The heart rate and the left-ventricular contraction time were obtained directly from the ECG. The corrective coefficient for the mean left atrial pressure, $\eta_{P_{LA}}$, was obtained by assuming that the end-diastolic pressure in the left atrium and ventricle are equal, i.e. there is no mitral flow at the end of the filling phase[160]. Consequently, $\eta_{P_{LA}}$ depends on the measured EDV as

$$\eta_{P_{LA}} = \frac{E_{min,LV}\,(EDV - V_0)}{\bar{P}_{LA,ref}} \tag{4.2}$$

where $\bar{P}_{LA,ref} = 7.8$ mmHg, and $E_{min,LV}$ and V_0 are the minimum left-ventricular elastance and the corrective volume of the reference data set, respectively.

(d) The maximum elastance factor η_E was quantified according to Shishido *et al.*[164], who evaluated the maximum left-ventricular force of contraction as a function of the pressure at the end of isovolumic contraction, the end-diastolic and end-systolic pressures, the SV, and the pre-ejection and ejection periods. As the pressure at the end of isovolumic contraction and the end-systolic one can be approximated with the end-diastolic and end-systolic central pressures, respectively, the estimation of η_E for each subject is deducible from measured data. We further assumed that the minimum left-ventricular elastance $E_{min,LV}$ does not change significantly between individuals.

(e) Finally, the unique resistance coefficient for all the terminating models η_R was chosen in order to fit as well as possible the diastolic pressure in the measurement sites. Notice that η_R is the

only coefficient in our subject-specific validation obtained by fitting model outputs on measured data.

Table 4.2 lists the corrective coefficients obtained for each subject. Some preliminary model trials showed that changes of rheological properties in the physiological range (±40%) impact results less than 1 %. Therefore, the same blood viscosity was used for all subjects.

Table 4.2. Values of the subject-specific corrective coefficients for each subject of the population.

	Subjects					
	1	**2**	**3**	**4**	**5**	**6**
η_L	0.97	1.02	1.03	0.99	1.00	1.04
η_D	0.99	1.03	1.01	1.00	1.01	1.01
η_W	0.925	0.95	0.985	1.00	1.00	1.00
$\eta_{P_{LA}}$	0.95	1.31	0.91	0.75	0.85	1.23
η_E	0.99	0.73	0.95	1.58	1.09	0.66
η_R	1.18	0.86	0.99	0.88	1.15	1.06

4.2.3 Results

As presented above, in the subject-specific validation some of the model parameters used to describe a typical (generic) young man are modified in order to fit quantities measured on specific subjects. The aim is to show how the adjustment of few key-parameters gives reliable subject-specific setting of the model for a population of young healthy male. The validation is carried out by quantitatively comparing outcomes of the subject-specific models with data obtained from non-invasive *in vivo* measurements.

Figure 4.4 shows the comparison between measured and simulated pressure waves for the subject 3 (similar results are obtained for all the subjects). The subject-specific left-ventricular pressure-volume loop, with the measured extreme values is also reported.

The overall agreement is very satisfactory. In all measure sites, both the shape and the systolic and diastolic values are in close agreement with the measured ones. The timing of peaks as well as their values are well reproduced, demonstrating that the pressure

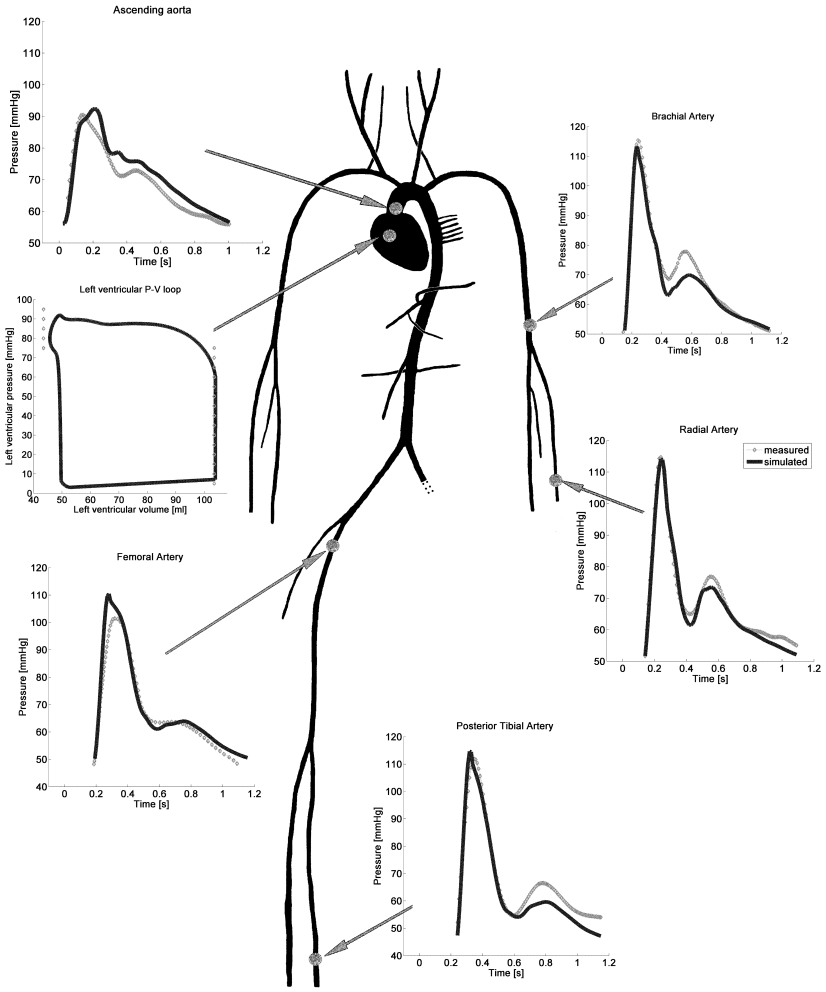

Figure 4.4. Comparisons between measured (lighter lines) and simulated (darker lines) pressure waves for the subject 3. The simulated left-ventricular pressure-volume loop is also shown along with the measured end-sistolic and end-diastolic volumes (dotted lines).

wave propagation along the arterial tree is well simulated. Moreover, in all sites the diastolic decays of the modelled and measured arterial pressures exhibit similar slopes, testifying that resistive and capacitive properties downstream the measuring sites are correctly quantified by the model. Although small errors on maximum and

minimum values occur in the central pressure profile, simulated pressure wave shows a second late-systolic peak that the profile reconstructed with the SphygmoCor does not provide. It is worth noting that such a negative augmentation index is normally associated with a young condition[70]. Finally, the left-ventricular volume range only slightly differs from the measured value.

For each subject, table 4.3 lists the percentile errors of pressures and ventricular quantities obtained with the subject-specific models. The errors about the left-ventricular sector are small and, in particular, the assumption about the left atrial pressure (that determines the EDV) gives very good results, determining an EDV error smaller than 0.4 % for all the subjects. The simulated ESV is always bigger than the measured value, but errors are limited, as well as errors about SV, $\bar{Q}$, and EF.

Regarding the arterial tree, all the errors about the maximum and minimum pressure are generally lower than 8 %, with single values equal to 10 and 12 %, respectively. Mean pressures exhibit an error lower than 7 %, although spurious errors reach 10 %, while the root-mean-square error reaches a maximum of 13 % even if is normally lower. The average of the root-mean-square errors for every subject is less than 8.5 %. For all the subject, the posterior tibial artery presents bigger error than the femoral one, while the best results are observed on the ascending aortic pressure.

Table 4.3 also shows the errors resulting from the model used without subject-specification, namely the generic model with η_i=1. They are (sometimes remarkably) high and demonstrate the effectiveness of the proposed subject-specific setting procedure. Finally, model was run with a flat velocity profile instead of relation (2.27), by obtaining errors systematically higher of about 4-6 % depending on the individual. Such increases are small but not negligible and justify the caution into modelling the velocity profile.

A systematic sensitivity analysis is beyond the scope of this work. However, our experience about model behaviour allows to give some indications about the impact of coefficients η_i. η_R is the most sensitive parameter, being able to (almost uniformly) affect pressure values throughout the heart-arterial system. Also η_E has a significant impact, but mainly concentrated in the systolic phase. Small changes of η_D affect the pulse pressure, while heart variables remain substantially unaltered. Finally, small changes of η_W and

Table 4.3. Percentile errors corresponding to the subject-specific models (SS) and the generic model (G) with respect to the measured data. The first block corresponds to the left ventricle, while the others refer to pressure waves. For pressure blocks, max, min, and mean indicate the percentile errors of the maximum, minimum, mean, while rms is the root-mean-square of errors during the complete cycle pressure. $r\bar{m}s$ is the average root-mean-square in all the measuring sites. A.Aorta and P. Tibial stand for Ascending Aorta and Posterior Tibial, respectively.

		Subjects											
		1		**2**		**3**		**4**		**5**		**6**	
		SS	**G**	**SS**	**G**	**SS**	**G**	**SS**	**G**	**SS**	**G**	**SS**	**G**
Left Ventricle	EDV	0.3	3.1	0.2	-26	0.4	6.4	0.4	26.6	0.3	13.6	0.3	-18.4
	ESV	6.1	8.3	9.6	-16.1	4.6	20.3	7.2	34.1	0.7	16.2	9.3	-15.6
	SV	-4.5	-2.1	-6.9	-6.7	-2.7	-3.5	-5.0	-20.6	-0.1	11.3	-7.6	-20.7
	$\bar{Q}$	-4.8	15.4	-2.0	-13.2	-2.8	20.5	-5.3	8.5	-0.1	21.3	-7.4	4.3
	EF	-2.7	-2.5	-3.6	-5.5	-1.7	-3.5	-3.8	-3.5	-0.6	-1.5	-4.2	-1.5
A.Aorta	max	2.3	6.2	6.2	6.7	2.2	24.5	2.0	-2.8	4.1	10.8	5.1	14.4
	min	-0.1	7.5	1.0	10.7	0.2	32.9	1.4	-8.1	7.6	14.1	1.9	17.7
	mean	-0.7	5.5	5.9	11.3	2.6	33.4	0.9	-3.5	2.6	10.2	4.4	15.8
	rms	3.1	13.0	6.3	15.5	4.5	36.5	3.5	9.0	4.3	11.8	5.8	21.1
Brachial	max	4.1	6.9	-1.2	-4.6	-1.7	6.9	0.7	-12.5	1.4	2.4	3.0	5.8
	min	1.1	8.3	-3.8	0.6	1.1	27.4	-8.2	-18.7	-6.9	1.5	-5.6	1.6
	mean	-4.5	8.6	-5.0	2.9	-3.4	26.7	-9.5	-15.6	-8.1	-0.9	-4.1	3.9
	rms	7.1	21.4	6.9	15.9	5.2	37.6	9.8	23.1	9.5	11.6	7.7	15.3
Radial	max	1.0	3.8	2.3	-2.6	-0.5	8.3	1.6	-11.0	2.3	3.8	1.9	5.5
	min	-12.1	-6.6	-7.8	-3.6	-4.9	15.5	-4.5	-20.6	-4.1	-2.4	-4.4	-0.5
	mean	-9.8	-17.4	5.9	5.2	-2.4	27.6	-5.0	-13.9	3.7	7.8	-1.7	11.6
	rms	13.0	17.6	7.3	17.0	4.1	38.9	8.0	22.8	5.9	16.3	5.2	25.7
Femoral	max	0.8	6.2	2.1	-1.5	8.7	22.0	9.6	-1.1	3.9	8.1	5.2	6.4
	min	-4.5	-2.5	-0.5	9.7	4.1	38.3	-3.5	-12.6	0.8	12.5	-8.8	2.1
	mean	-6.8	-7.3	-1.3	3.8	2.3	32.5	1.1	-6.1	1.6	9.8	-3.8	4.3
	rms	8.8	16.6	3.9	12.9	6.4	41.5	6.2	16.1	5.2	19.7	9.6	17.4
P. Tibial	max	7.8	7.9	4.0	0.3	2.2	8.3	6.0	6.2	-1.6	14.7	6.2	8.3
	min	-12.1	-20.3	-11.5	-18.8	-12.8	-4.0	-7.0	-25.8	-12.4	-13.2	-10.3	-23.5
	mean	-5.8	9.2	-5.0	3.1	-5.1	27.7	-3.9	-14.2	-6.5	2.0	1.5	15.0
	rms	8.9	25.6	7.5	14.7	9.2	38.8	7.1	26.7	10.0	20.9	8.7	26.6
$r\bar{m}s$		8.2	18.8	6.3	15.2	5.9	38.7	6.7	19.5	7.0	16.1	7.4	21.2

η_L have modest effects on model outputs.

4.2.4 Limitations

In spite of the good results of our subject-specific approach, it is worth recalling some limiting aspects of the present approach.

Firstly, we assume axisymmetric geometry, wall impermeability, no longitudinal artery deformation, and Newtonian blood behaviour. Moreover, the structure of the pressure-compliance relation for the arterial walls is maintained through all the arterial tree.

Cerebral circulation, venous return, and coronary arteries are not taken into account in our model albeit their implementation is readily possible. However, when one is not interested in the specific investigation of the cerebral circulation, its effect on the rest of cardiovascular system can be conveniently simulated by suitable distal boundary conditions for carotid and vertebral arteries [145]. Even the assumption of constant pressure at the interface between arterial and venous side is generally accepted [15;78;145;171]. The lacking of the coronary artery modelling is more impacting, since coronary arteries have an important role on the amount of blood carried and on the arterial system behaviour during diastolic period.

Another weak point concerns the reference central pressure, which is not measured but obtained by a transfer function, even if this latter is validated and used in the clinical practice. Similarly, the flow rate is only validated at ventricular level, where simulated mean blood volume has been checked against measured data. Indeed, spatially-distributed flow measurements would add interesting information about the model ability to reproduce not only the blood pressures but also flows in different body areas.

Finally, from the clinical point of view, we are aware of the limited number of subject-specific tests and the fairly-homogeneous conditions of individuals. The reduced spectrum of individual conditions allowed us to impose a general value to the minimum left-ventricular elastance. Moreover, we preferred to test our subject-specific procedure on males only because the relation between pulse wave velocity and diameter, which is used in the computation of the constitutive relation, has been obtained by a collection of previous works that measured clinical data prevalently on males (the male to female ratio is 40:3, when it is specified). However, in future works we will test our model and setting procedure involving female and old subjects, possibly in not healthy conditions.

4.3 Subject-specific validation: large subject set

The encouraging results obtained from the subject specific validation presented above allow us to pursue further improvements on subject-specific multi-scale modelling. The main progresses designed rely on both setting procedure and on the number of volunteers forming the population. Indeed, the limiting aspects of the precedent subject-specific setting procedure, mainly connected to the need of iterative fitting convergence for quantification of the resistance of the distal models, have been overcome.

The aim of the present Section is to present the improved subject-specific setting procedure and to check its capacity to predict central pressure from non-invasive measurements in a clinical context. Indeed, although some very interesting application of subject-specific 1D/0D mathematical model in clinical context has been proposed[20;27;78], the need of simpler model characterization has been widely highlighted[69;144;163]. To this aim, a population of 45 healthy young subjects has been recruited and several non-invasive measurements have been collected. Blind check against reference commercial instrument for systolic and diastolic central pressure estimation is finally performed.

Although this analysis is a part of a larger on-going work, the presented results will allow the Reader to effectively understand the major outcomes of this approach.

4.3.1 Measurements on the population

A number of 45 volunteers were recruited and the same measurements described in Subsection 4.2.1 were performed. Equal inclusion and exclusion criteria were also adopted. The resulting population shares with the previously-described subgroup sex, mean age and no notable differences were found neither in pressure level nor in pulse wave velocities.

4.3.2 Setting of the model parameters

As introduced, the setting procedure described in the last Section has been improved and reviewed in order to accomplish standard

requirements of clinical practice.

The parameters underlying subject-specific calibration were: length, diameter and mechanical properties of the arterial vessels, heart rate, left-ventricle contraction time, mean left atrial pressure, maximum myocardial force of contraction, and overall peripheral resistance. With a scheme similar to the one described in the precedent Section, subject-specific parameters were obtained by multiplying the corresponding reference values by suitable subject-specific corrective coefficients η_i as reported in the following procedure (subscript i specifies the parameter considered).

4.3.3 Results

Clinical and hemodynamic characteristics of the population are summarized in table 4.4.

Table 4.4. Clinical and hemodynamic characteristics of the population. *car*, *fem*, *tib* stand for carotid, femoral and posterior tibial locations, respectively. Results are shown as mean (μ) ± standard deviation (σ).

Quantity	$\mu \pm \sigma$
Age (years)	24±2
Height (cm)	178.1±6.3
Weight (kg)	74.8±10.2
bSBP (mmHg)	122.4±12.5
bDBP (mmHg)	67.7±9.2
BMI (Kg/m^2)	23.4±2.5
HR (bpm)	62.2±11.1
ESV (cm^3)	53.1±8.8
EDV (cm^3)	129.9±20.3
SV (cm^3)	81.7±18.7
Pulse Wave velocity	
car-fem (m/s)	6.0±0.9
car-rad (m/s)	7.3±1.5
fem-tib (m/s)	9.3±1.5

In Table 4.5, mean central diastolic, systolic and pulse pressure estimations by the mathematical model and the SphygmoCore are shown, along with absolute and percentage differences for the whole population.

In figure 4.5 a summarizing comparative plot is shown. Boxes represent values obtained with the two methods, and vertical lines report standard deviations. Furthermore, in top charts of figures 4.6 and 4.7 the best-fit linear regression of both systolic and diastolic comparisons is shown. Differently, in bottom charts of figures 4.6 and 4.7 Bland Altman plots for both values are reported. When errors are lower then 10% we assume that the esteem is acceptably accurate. In all charts of both figures evaluations characterized by discrepancies lower than the 10% of the SphygmoCore esteems are

Table 4.5. Comparison between mathematical model and SphygmoCore predictions for the whole population. Results are shown as mean ± standard deviation. Pressures (Pr.) are expressed in mmHg. P is the p-value.

	Model	SphygmoCore	P	Absolute difference	Relative difference (%)
Systolic Pr.	110.1±19.1	102.2±10.2	0.0004	7.9±15.0	7.7±14.8
Diastolic Pr.	64.7±12.9	68.4±9.4	0.001	-3.8±8.0	-5.8±12.0
Pulse Pr.	45.5±10.8	33.8±6.2	0.0001	11.7±13.2	21.1±24.8

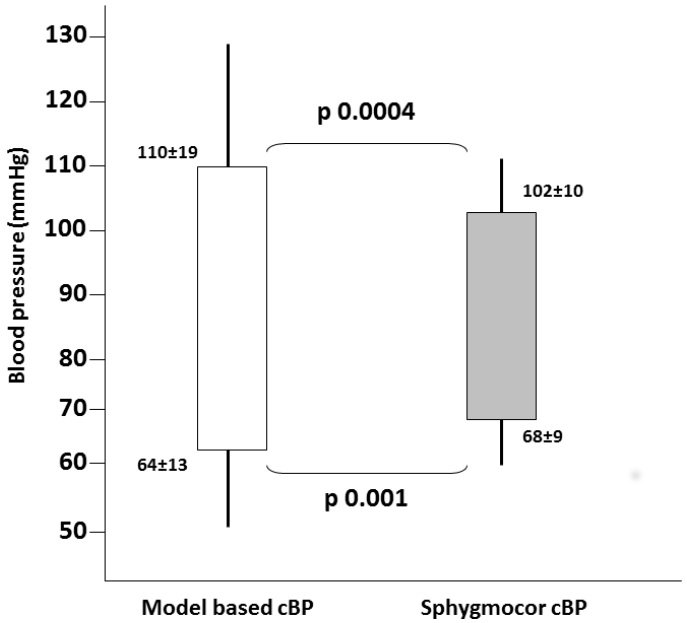

Figure 4.5. Comparisons between model (lighter line) and SphygmoCore (darker line) central pressure predictions. P is the p-value.

highlighted by dark markers.

In Table 4.6, the population is divided in acceptable and impaired accuracy, and the corresponding averaged clinical and hemodynamic data are shown. Whenever the difference between central blood pressure values obtained with the two methods is lower than 10% the model performance is considered acceptable.

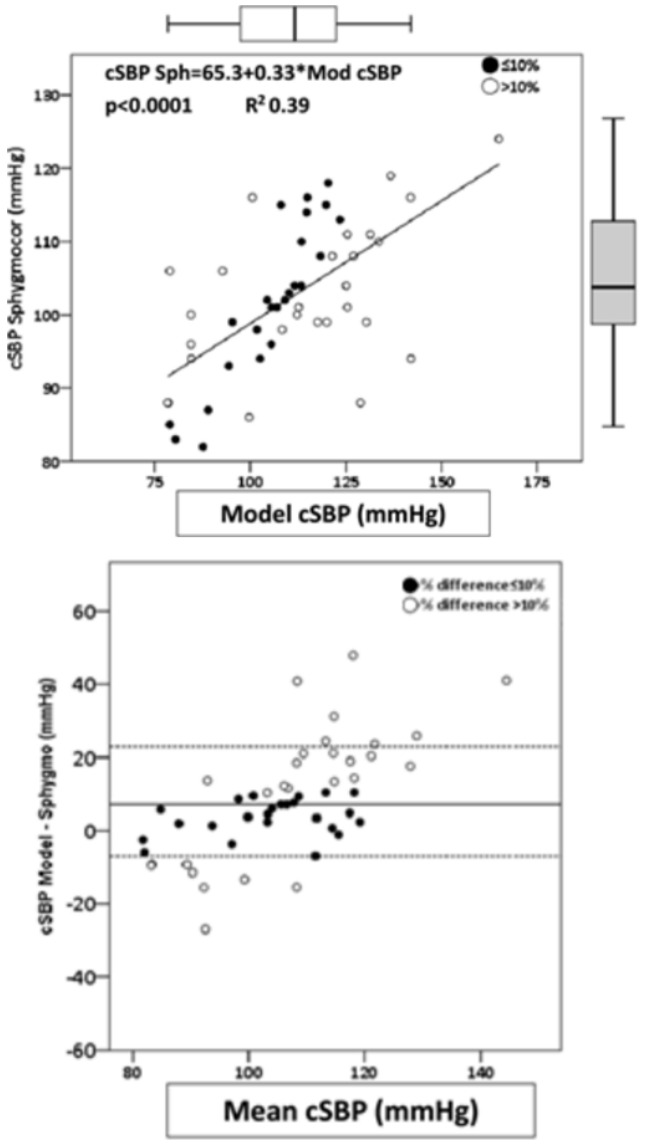

Figure 4.6. Comparisons between model (Model cSBP) and SphygmoCore (SphygmoCore cSBP) systolic central pressure predictions. Top: linear regression analysis. Bottom: Bland Altman plot. Discrepancies lower than the 10% of the SphygmoCore esteems are highlighted by dark markers.

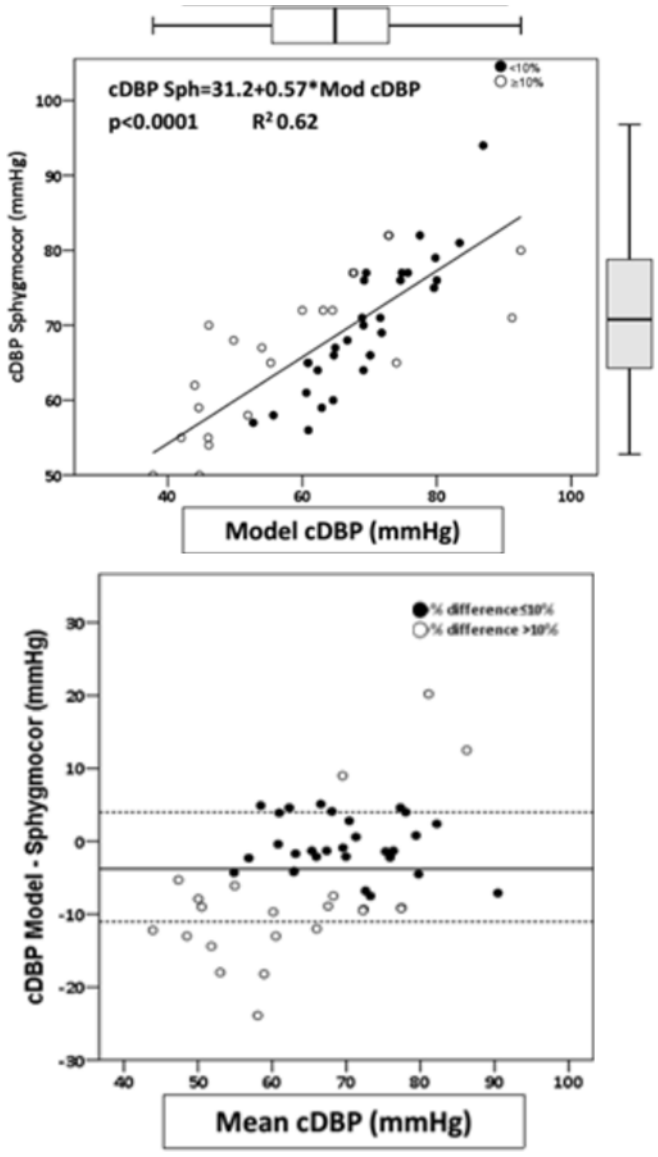

Figure 4.7. Comparisons between model (Model cDBP) and SphygmoCore (SphygmoCore cDBP) diastolic central pressure predictions. Top: linear regression analysis. Bottom: Bland Altman plot. Discrepancies lower than the 10% of the SphygmoCore esteems are highlighted by dark markers.

Table 4.6. Comparison between clinical and hemodynamic variables of acceptable and impaired accuracy values of the population.

	cSBP			cDBP		
	Acceptable Accuracy	Impaired Accuracy	p	Acceptable Accuracy	Impaired Accuracy	p
Clinical variables	n.24	n.27		29	22	
%	48%	52%		56%	44%	
Height (m)	175.46±5.94	180.07±5.64	0.006	177.21±6.50	178.82±5.75	0.36
Weight (Kg)	70.60±9.58	77.11±9.15	0.01	71.95±10.00	76.82±9.08	0.07
bSBP (mmHg)	122.25±13.44	122.44±11.93	0.95	121.55±12.05	123.41±13.35	0.6
bDBP (mmHg)	66.88±7.13	68.57±10.83	0.51	69.33±8.59	65.73±9.83	0.16
BMI (Kg/m^2)	22.89±2.46	23.74±2.19	0.19	22.83±2.21	24.00±2.39	0.7
BSA (m^2)	1.86±0.14	1.96±0.13	0.006	1.88±0.15	1.95±0.13	0.10
HR (bpm)	63.42±10.70	61.13±11.62	0.47	60.03±9.92	65.07±12.21	0.11
Hemodynamic variables						
ESV (cc)	48.70±7.04	56.93±8.58	0.0005	52.24±8.85	54.14±8.93	0.45
EDV (cc)	120.59±15.01	138.17±21.03	0.001	127.71±20.54	132.78±20.09	0.38
SV (cc)	79.13±17.58	83.93±19.79	0.36	79.59±19.30	84.41±18.08	0.36
CO (l/m)	5±1.3	4.9±0.9	0.73	4.7±1.2	5.2±1	0.11
CI ($l/min/m^2$)	2.7±0.7	2.5±0.4	0.22	2.5±0.6	2.7±0.5	0.23
Pulse Wave velocity (m/s)	5.80±0.88	6.13±0.88	0.19	5.70±0.69	6.33±1.00	0.01

4.3.4 Discussion

Compared to peripheral value, central pressure is recognized to be more descriptive of target organ damage[149;150;154], and thus a better predictor of future cardiovascular events.

We compare model prediction against reference commercial instrument SphygmoCore (Atcor Medical, Australia) for all the subjects of the population.

Both diastolic and systolic central pressure estimations by the mathematical model resulted to be significantly correlated with the SphygmoCore esteems (r^2=0.62 (coefficient of determination), p<0.0001 and r^2=0.89, p<0.0001 for diastolic and systolic values, respectively). The mathematical model significantly overestimates systolic pressures (+7 [-1,17] mmHg, p=0.0004) (median [25,75] percentile range) and underestimates diastolic values (-3.9 [-9,0.8] mmHg, p=0.001), leading to a global over-appraisal for pulse pressure. A good accuracy (difference lower than 10%) was shown in the appraisal of central blood pressure values in 48% and 56% of the studied individuals, for systolic and diastolic values, respectively.

Subjects whose central estimations were inaccurate showed significantly higher anthropometric values (height, weight, BMI and BSA) as well as higher left-ventricular dimensions (especially correlated to systolic discrepancies) and slightly higher values of celerity

of propagation of the waves (mainly correlated to diastolic differences).

However, some comments have to be done about the SphygmoCore used as reference. Indeed, prediction by SphygmoCore device showed brilliant agreement with invasive central pressure measurements only when invasive mean and diastolic pressure measurements were used for calibration procedure[34]. In fact, recent large meta-analysis[34] showed that when this device is used with oscillometric pressure calibration, as in the present case, the errors steeply increase. Errors of -1.1±4.1 mmHg (mean± SD), -0.5±2.1 mmHg and -0.8±10.3 mmHg for systolic, diastolic and pulse pressure, respectively, obtained with invasive-setting procedure strongly grow to -8.2±10.3 mmHg (mean± SD), 7.6±8.7 mmHg and -12.2±10.4 mmHg when non-invasive pressure were used[34]. These results further highlight the need of new instruments for central pressure estimation.

In the next paragraphs we explain how these errors reflect on the comparison. Considering a generic error e_n

$$e_n = v_{m,n} - v_{s,n}, \tag{4.8}$$

where $v_{m,n}$ and $v_{s,n}$ are the estimation obtained with the model and with the Shygmocore for the generic n-th subject. The variance of the error is thus written as

$$\mathrm{Var}(e) = \frac{1}{N}\sum_{n=1}^{N}(e_n - \bar{e})^2 = \frac{1}{N}\sum_{n=1}^{N}((v_{m,n} - v_{s,n}) - \bar{e})^2 \tag{4.9}$$

where the mean error is calculated as

$$\bar{e} = \frac{1}{N}\sum_{n=1}^{N} e_n = \frac{1}{N}\sum_{i=n}^{N}(v_{m,n} - v_{s,n}). \tag{4.10}$$

We firstly deal with the bias of the SphygmoCore esteems, as reported by Cheng and colleagues[34]. One can thus eliminate the bias simply as

$$v_{sc,n} = v_{s,n} + A \tag{4.11}$$

where the subscript sc refers to the result obtained from SphygmoCore once corrected for the bias A. We thus obtain the n-th corrected error $e_{c,n}$ as

$$e_{c,n} = v_{m,n} - v_{sc,n}. \tag{4.12}$$

Afterwards, we deal with standard deviation σ, which is a matter of propagation of uncertainty. In the case of uncorrelated variable, i.e. if the values obtained by our model do not depend on the error of the reference instrument, the (unknown) variance of the model result in respect to invasive (denoted by the subscript i) measurement σ_{m-i} would simply be the sum of the variance of the differences between model result and SphygmoCore predictions σ_{m-s} and the variance of SphygmoCore values in respect to invasive measurement σ_{s-i}. In such a case, the covariance between model results and SphygmoCore esteems should be zero.

But this is not the case. Indeed, the difference between model result and SphygmoCore esteems depend on the errors produced by the SphygmoCore itself in respect to invasive reference values. In such a condition, we are obliged to restore the role of non-null covariance, thus writing

$$\sigma^2_{m-i} = \sigma^2_{m-s} + \sigma^2_{s-i} - 2\ cov(m, s). \tag{4.13}$$

But there is no way of quantify this covariance, thus the standard deviation obtained comparing model result and SphygmoCore esteems cannot be extrapolated considering error propagations. Consequently, we can not consider as valuable the information regarding standard deviations. The only information we can finally draw regards mean differences between both esteems. In this respect, remembering relation 4.12, mean systolic error in respect to statistically-derived invasive measurements is almost null (+7-8.2=-1.2 mmHg), and very small positive residual exists for diastolic value (-3.9+7.6=3.7 mmHg).

4.3.5 Limitations

The main limitation of the present study concerns the term of comparison of the model predictions. Since invasive pressure measurements were not available, we analyse the model esteems through comparison against a commercial device for central pressure estimation. But, the non-invasiveness of the study entails that SphygmoCore esteems are possibly affected by large errors. Consequently, although we easily deal with mean error, standard deviation cannot be given for such a comparison.

Other limitations regard the limited number of individuals screened, and the relative homogeneity of their characteristics.

Further studies are needed to check model outcomes against invasive central pressure measurements in a population with different sex, ages and pathological conditions.

4.4 Investigation on ageing process

Cardiovascular ageing is an important process that deeply influence human life. As with all living matter, arterial and cardiac tissues underneath a degenerative evolution which strongly influences the ventricular-arterial interaction. As a result, ageing has been found to be the most important risk factor for cardiovascular diseases[30].

The cycling behaviour of the ventricular ejection imposes time- and space-dependent pressure and flow regimes through the arteries. Consequently, arterial tissues are subjected to a damaging cycling stress state, as expected by fatigue theory[129], which results in both a generalized stiffening and a diffused enlargement of large arteries. The complex interaction between this degeneration and pressure wave pattern entails an augmented load to the ventricle, which becomes progressively stronger in order to preserve blood supply to cells necessary to life.

Being age-related increase of ventricular load a direct consequence of wave pattern changes, fluid-mechanics processes play a mayor role. Although this widely accepted role, there still exists a lack of systematic qualitative studies on arterial ageing through physical description.

The present Section aims to reproduce and analyse the fluid mechanics of an ageing arterial system by means of mathematical modelling. In detail, firstly the age-dependent setting of the multi-scale heart-arterial interaction model is presented (Subsection 4.4.1). Afterwards, the main obtained results are confronted with up-to-date literature data (Subsection 4.4.2). Finally, a discussion (Subsection 4.4.3) includes the physical interpretation of the resulting processes, along with an embracing description and characterization of the cardiovascular ageing.

4.4.1 Age-dependent modelling

With progressive ageing the behaviour of a healthy cardiovascular system changes. The main characteristics of the ageing cardiovascular apparatus includes an increased stiffness and a diffuse geometrical remodelling of large arteries and an increased left-ventricular maximum force of contraction.

Aiming to reproduce the heart-arterial interaction during ageing several physiological quantities are modelled as a function of age. Starting from literature data, we modify the corresponding parameters of the model, obtaining an age-dependent characterization of left ventricular-arterial interaction.

Arterial quantities

The arterial quantities underlying age-dependent setting are diameter, mechanical properties of the arterial wall, length and thickness.

Diameters The evidence that aorta and common carotids non-uniformly dilate with ageing is widely accepted[21;45;54;70;76;79;118;153], while the behaviour of medium vessels is still matter of debate. In this respect, the majority of authors either do not find any correlation between age and medium-vessel diameters or do not reach statistically significance[11;79;98;188], although a weak increase even in medium arteries as been reported[21]. Consequently, we choose to do not change the diameter of muscular arteries.

Following Virmani *et al.*[186], we subdivide the aorta into four different parts, while carotids are considered together. The age-dependent diameter is written as

$$\Delta D(y) = \alpha_D \, (y - 20) \;\; [\text{mm}], \tag{4.14}$$

where y is age in years and the coefficients α_D are 0.1282, 0.1467, 0.1425, 0.1038 and 0.0239 for ascending aorta and aortic arch, descending thoracic aorta, supra-renal aorta, sub-renal aorta and carotids, respectively.

Wall thicknesses The structural changes affecting large arteries during ageing become evident analysing their wall thickness h. During ageing we assist to an increase of intima-media thickness [95;99;117;118;129;186] mainly concentrated in the intima[65;129;186]. In this process there are firm evidences of a disorganization, fragmentation and calcification of elastin fibres[65;118] while collagen fibres progressively acquire further cross-link[54;65].

Coherently with the data source adopted for diameters, we follow Virmani *et al.*[186] and subdivide the aorta into four different

parts where the thickness increase is set as

$$\Delta h(y) = \alpha_h(y - 20) \text{ [mm]}, \tag{4.15}$$

where the coefficients α_h are 0.0041, 0.0071, 0.0064, 0.0088 and 0.007 for ascending aorta and aortic arch, descending thoracic aorta, supra-renal aorta, sub-renal aorta and carotids, respectively.

Even though these changes are implicated into the increase in stiffness, in our mathematical model the arterial thickness has a role only in determining the volume where arterial wall viscoelasticity applies, since the stiffening of the arteries is considered directly by imposing the increase on pulse wave velocity thorough the constitutive relation.

Lengths Only recently the age-related large arteries elongation has been quantified. All the authors agree that only the aorta elongates with age, while iliac [173] and carotid [92;173] do not, but there are still controversies on the specific distribution along the aorta. In fact, Sugawara *et al.* [173] and Hickson *et al.* [76] found a elongation of 0.9 mm/y of the ascending aorta and ascending arch and 0.8 mm/y of the aortic arch, respectively, but none on the descending part. This quantities are confirmed by Kröner *et al.* [92] that report a values of 1.05 mm/y of the aortic arch but do not investigate further downstream. Although the total lengthening of the aorta found by Rylski *et al.* [153] and Craiem *et al.* [45] are similar to those already mentioned, i.e. 1.04 and 1.24 mm/y, respectively, these investigations found a diffuse, non-uniform, elongation of all the aortic segment investigated.

Since the statistically significance of the data proposed by Sugawara *et al.* [173] is elevated with respect to the others data analysed, and considering the convincing argumentation against an effective elongation of more tethered segments proposed by O'Rourke *et al* [128], we chose to uniformly modify only the ascending aorta and the ascending part of the aortic arch imposing a total elongation of 0.9 mm/y on the corresponding vessels.

Mechanical properties Large arteries stiffen with advancing age [54;65;70;76;92;108;111;118;121;128;141;185] in a non-homogeneous way [76;129].

Incremental Young modulus at a defined pressure, eventually mediated through the different layers, should be the information

used to characterize arterial wall mechanical properties. However, such a measurement can only be achieved by invasive technique, which cannot be used neither in large-population studies nor in clinical practice. By the way, in the next future non-invasive technique along with local pressure measurement or estimation will probably give to physicians further possibility to analyse *in-vivo* arterial mechanical response.

But to date, most of the authors measured a unique non-invasive value that should represent the overall large-arterial stiffening: the carotid-femoral pulse wave velocity, i.e. the ratio between the estimated distance and the measured time lag of pressure measurements at these locations. The choice was firstly dictated by both its non-invasive nature and its simplicity. By the way, even such a widely used system of measurement conserves some kind of controversy, specifically relied to distance measure and to automatic identification of the foot of the waves. Considering physician's perspective, in this Section we will occasionally speak about *stiffening* with the improper meaning of a increase of celerity of propagation.

Thanks to enormous advances in measurement technique (mainly ultrasonic phase-locked echo-tracking system and cine phase-contrast magnetic resonance imaging), recent works have evidenced that different districts of the aorta degenerate non homogeneously, and almost all the authors agree on a decreased aortic stiffening rate moving away from the heart.

Differently, the stiffening of other, smaller and more muscular, arteries is still matter of debate. Even if a pulse wave velocity growing trend in both upper and lower limb arteries has been found[9], more recently none age-related changes on femoral[11;83], carotid-brachial[111], radial[21], iliac[66] and femoral[83] mean celerities have been measured. These controversial evidence can be ascribed to different vasoactive stimuli, which deeply influence stiffness indices of peripheral muscular arteries[83]. With a conservative approach, we choose to limit age-dependent mechanical changes to aorta and carotid arteries.

Since the work of Vermeersch *et al*[185] has a much bigger statistical basis in respect to the other published works, we choose to follow the mean carotid-femoral pulse wave velocity increase reported in this work. Afterwards, we use the spatial distribution of such a stiffening proposed by Hickson *et al.*[76]. In detail, we modify

aortic and common carotid pulse wave velocities c as

$$\Delta c = \alpha_{C1}\,(y-20) + \alpha_{C2}\,(y-20)^2\,[\mathrm{m/s}] \tag{4.16}$$

where the list of coefficients is given in table 4.7.

Table 4.7. Values of the stiffening coefficients. *Abd* stands for abdominal.

	arch	**thoracic**	**mid abd.**	**late abd.**	**carotids**
α_{C1}	-0.004	0.011	0.005	0.06	-0.118
$\alpha_{C2}10^{-3}$	0.44	0.58	0.53	0.29	1.94

It is worth noting that such as wave celerity of propagation increase results from changes on arterial diameter, thickness and incremental Young modulus. Indeed, for a given incremental Young modulus pulse wave velocity increases with thickening and decreases with enlargement.

Left ventricle elastance and systole duration

The dramatic changes affecting the arteries have a counterpart on the heart functioning. As suggested by several authors[30–32;41;50;141], left ventricular behaviour changes in order to maintain as efficient as possible the heart-arterial interaction and thus preserving the amount of blood ejected[159].

The well known ventricular load growth with age determines a consequent increase in left ventricular maximum elastance. In order to impose this variation in the age-dependent model we follow Redfield *et al.*[141] that found a 0.5 percent increase on maximum elastance per year. This value is similar to the 0.8 %/year reported by Cohen and colleagues[41].

Since our mathematical model is addressed to study LV-arterial systolic interaction the age-dependence on the left ventricular diastolic filling is not important as long as the final end-diastolic volume does not change with age[32;94].

Finally, although the heart rate does not change during ageing [32;54;57], several studies have reported an increase in systole duration (QT interval)[106;119;176]. Following the data proposed by Mangoni *et al.*[106] we impose an age-dependent systolic duration as

$$t_{ce} = 0.37 + 0.372\ 10^{-3}\ y\ \ [\mathrm{s}]. \tag{4.17}$$

It is worth noting that systolic period become increasingly important with age.

4.4.2 Fluid mechanics of ageing

As a result of the imposed age-dependences of several model parameters, the evolution of the heart-arterial interaction system with age can be reproduced. In the following Section we present the results obtained along with a comparison with the up-to-date knowledge. We especially focus on ascending aortic, left ventricular and brachial sections because they are one of the most interesting locations for medical community. However, since blood flow and pressure field at these locations result from the widespread behaviour of the cardiovascular system, and especially of the aorta, we pursue a study of the whole large arteries.

Ascending aorta

Since it is recognized as the better predictor of different pathologies [187], we firstly focus on ascending aortic condition.

On the top-left box of figure 4.8 the evolution of the ascending aortic pressure profile during ageing is proposed, while on the top-right box an overview of maximum, minimum and pulse pressures at the same location is showed as a function of age.

Analysing the results showed, we can see that systolic value increases with increasing rate with age, resulting in an increment of more than 10 mmHg from 20 to 80 years old. As a reference, we report the 12 mmHg increase in systolic pressure invasively measured by McEniery *et al* [108] in a similar age range. Our maximum increment on a decade basis is 4.8 mmHg, a value slightly smaller that the 6.5 mmHg/decade reported by Chen *et al* [32] from invasive measurement. Differently, literature data using non-invasively calibrated transfer functions report much higher values [76;142], but the systematic error reported by following this practice [34] seems to account of such a disparity.

On the other hand, diastolic pressure firstly grows until around 55 y.o. and then slightly decreases with advancing age. Both the increasing and then decreasing pattern, and the position of the maximum around 55 years are well documented in literature [108;142].

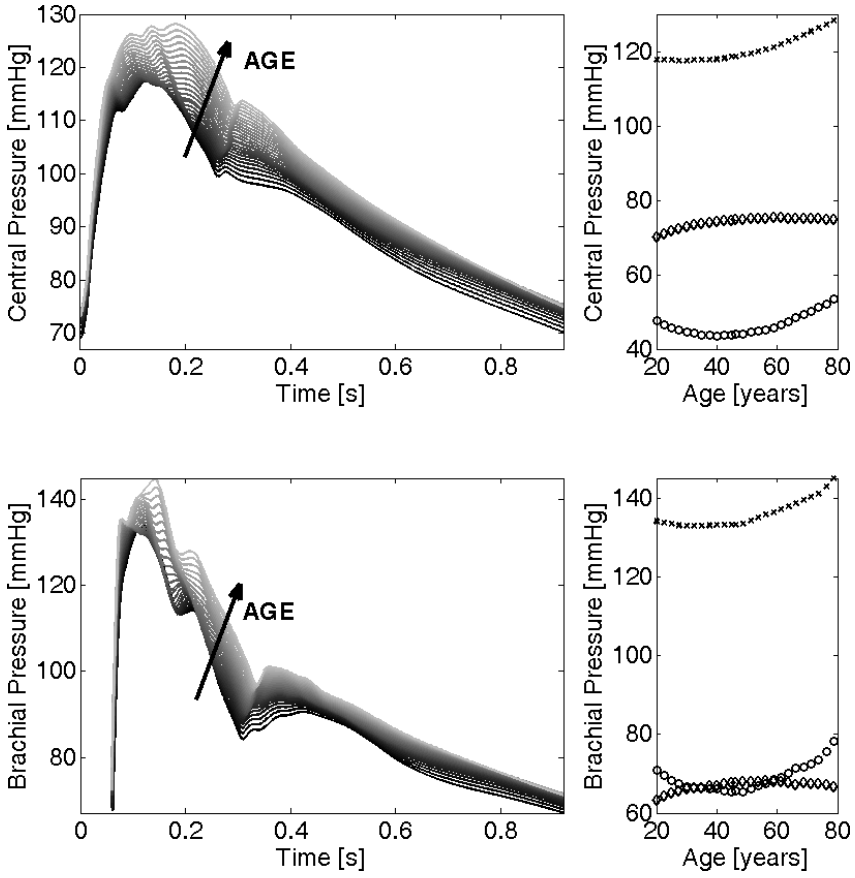

Figure 4.8. The left column reports pressure profile at ascending aortic (top) and brachial (bottom) arteries at different ages. Right column shows systolic (x), diastolic (Δ) and pulse (O) pressure, at same locations for different ages. From 20 to 80 y.o. with a 2.5 years step, the darker the younger.

Systolic and diastolic patterns in turn determine that pulse pressure, i.e. the difference between maximum and minimum pressure, firstly decreases and than inflates. More specifically, from a pulse pressure of 48 mmHg at 20 y.o. there is a decline until the minimum value of 44 is reached around 42 y.o.. Afterwards, pulse pressure increases and reaches a value of 54 mmHg at 80 y.o.. Very similar values have been obtained from in-vivo measurements by McEniery and colleagues, who obtain a values of 50 mmHg at 20 y.o., which

declines to the minimum value of 47 at 40 y.o. and then grows the maximum value of 57 mmHg at 80 y.o.. Analogously, Redheuil*et al*[142] measured values of 35, 33 and 60 mmHg at second, third and seventh decade of life.

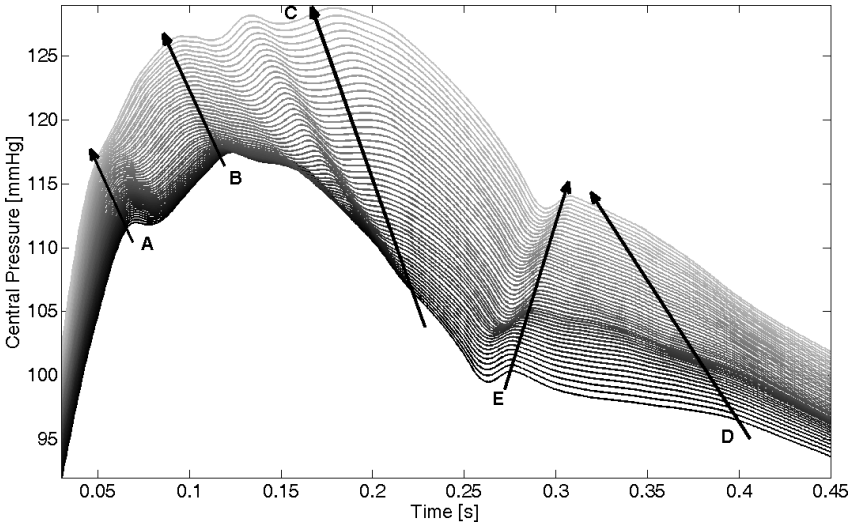

Figure 4.9. Zoom in systolic and early diastolic portion of ascending aortic pressure. From 20 to 80 y.o. with a 1.25 years step, the darker the younger. Arrows indicate ageing direction.

Thanks to the zoom on systolic and early diastolic ascending aortic pressure proposed in figure 4.9 we can appreciate how the pressure curve at young age is characterized by a first inflection point, here marked with the letter A, and a subsequent peak B, which corresponds to the maximum systolic pressure, while diastole presents a relative peak D.

With age the first inflection point A grows in absolute value, it is smoothed and is slightly anticipated, while major changes affect central systolic portion. Indeed, the first peak B is gradually overwhelmed by the second peak C, and late systolic pressure finally dominates. Consequently, the augmentation pressure, i.e. the pressure difference between maximum and first inflexion, and the augmentation index, i.e. the augmentation pressure divided by pulse pressure, progressively increase with age, as reported by several authors[108;121;142;181;195]. Differently, the increased activation time

results in a delayed dicrotic notch with age. Similar backward moving pattern can be seen on diastolic part, where the isolated peak D around half of diastolic time seen at young ages moves backward, even reaching dicrotic notch. Therefore, diastolic decay becomes more regular with advancing age.

Pressure distribution along the aorta

In figure 4.10 maximum and minimum local pressure in a cardiac cycle are shown all along the aorta at different ages.

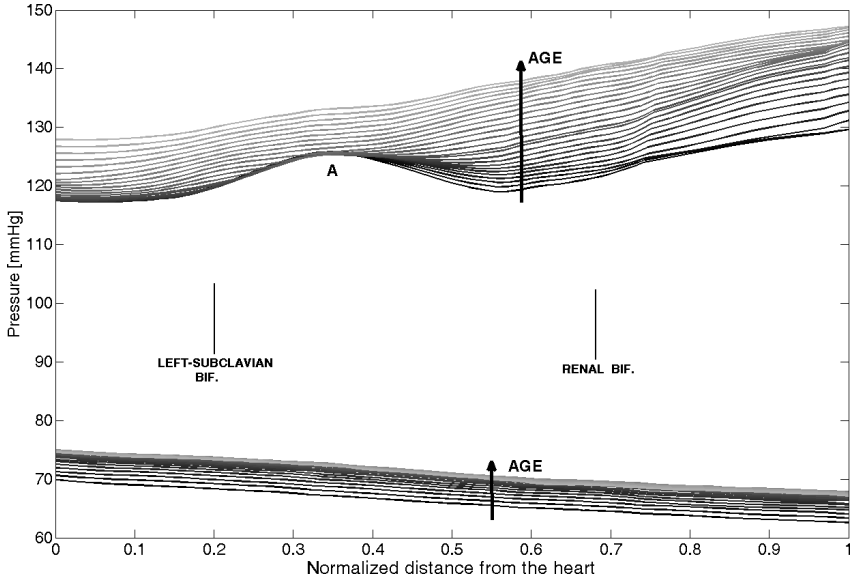

Figure 4.10. Maximum and minimum pressure along the aorta at different age. From 20 to 80 y.o., with 2.5 years step. The darker the younger. Central vertical lines represent the location of left-subclavian and renal bifurcations.

The well documented[121] pulse pressure amplification is here showed. Indeed, for all ages, maximum pressure at more distal locations are higher than their first aortic counterparts, while minima are lower. Furthermore, maximum pressure from 20 to (at least) 50 y.o. presents a peak located in the thoracic aorta, here highlighted by the letter A. This local maximum gradually disappears with age, leaving an almost-uniform pulse pressure amplification with distance from the heart. A quantitative verification of

the systolic trend is obtained by analysing the few data proposed in literature regarding simultaneously invasive pressure measurements along the aorta (see figure 4.11). As we can see, different

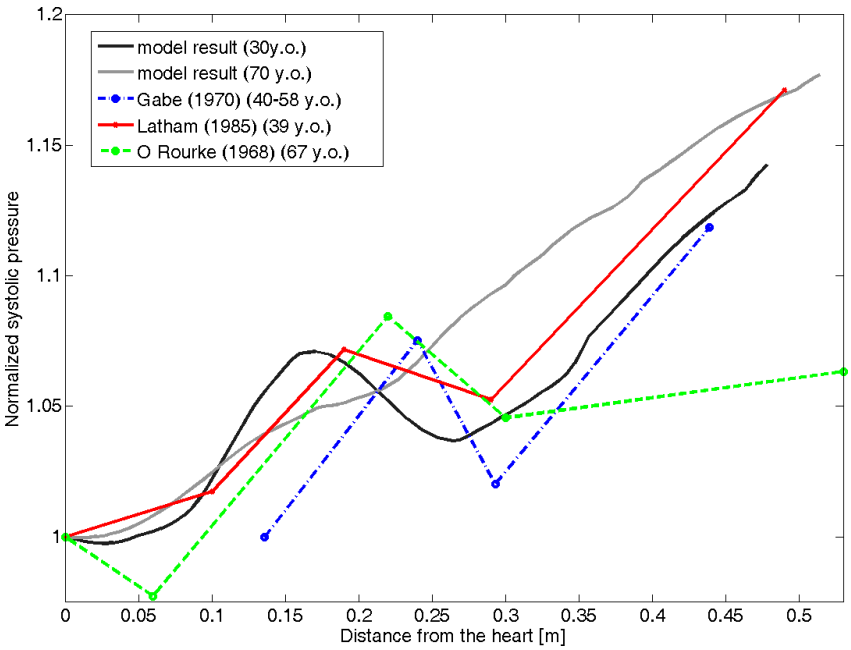

Figure 4.11. Maximum pressure along the aorta normalized to maximum pressure at aortic root. Comparison between simulation data and invasive measurements from literature[59;97;127].

authors[59;97;127] reported a local maximum pressure peak localized around late thoracic aorta.

Brachial artery

Since long time ago, physicians measure brachial pressure by means of oscillometric devices. Although recently central pressure has been proving its superiority in predicting morbidity and mortality [150;154;187], and considering that non-invasive method for aortic pressure quantification are still missing[34], brachial pressure is still used as a fundamental quantity for patient pressure characterization in clinical practice.

In the bottom charts of figure 4.8 brachial pressure profile are showed during ageing. From the bottom-left side, we observe a

progressive deformation of the pressure waveform, which results in a somehow similar trend with respect to what described for ascending aortic pressure, as visible in the right column of figure 4.8. Indeed, maximum pressure grows with increasing rapidity with age, while diastolic pressure firstly increments and then decrements after around 50 years old. Brachial maximum pressure increases of almost 14 mmHg from 20 to 80 years old, whose great majority (around 12.5 mmHg) is concentrated in the age range from 45 to 80. Indeed, from 20 to 45 y.o. maximum brachial pressure does not vary substantially. Despite the absolute values suffer from strong inter-variability, very important overall agreement on ageing trend has been reported. Indeed, Franklin and colleagues[57] measured a very similar pattern, with an almost-stationary value until 50 y.o., followed by a steep increase of around 10 mmHg until 80 y.o.. Similarly, Smulyan[166] and colleagues found a steady value between 40 and 55 y.o., followed by a marked growth of 5 mmHg in the successive five years. Analogous overall increases are obtained by McEniery *et al*[108] (7 mmHg from 20 to 80 y.o.), Kim *et al*[86] (+11.4 from 20 a 60 y.o.) and Segers *et al*[159] (6 mmHg from 38 to 53 y.o.).

About diastolic pressure, our numerical results show an increase from 67 to 71 mmHg from 20 to around 55 y.o., and then a decrease to 70 mmHg at 80 y.o.. Similarly, McEniery*et al*[108] found a values of 73 mmHg at 20 y.o. that grows to a maximum of 79 mmHg at 50-60 y.o. and then decrements to 75 mmHg at 80 y.o.. Similarly, Redheuil*et al*[142] measured values of 62, 79 and 69 mmHg at 20, 50-60 and 70 y.o., while Kim and co-workers[86] found values of 70, 79 and 77, at 20, between 50 and 60, and 70 y.o.. Slightly higher values where obtained by Franklin and colleagues[57], where diastolic brachial pressure at 20 y.o. of 73 mmHg irregularly increases to 76 mmHg at around sixty and then decreases to 70 mmHg at 80 y.o..

Our resulting trend for brachial pulse pressure shows a first decrease from 70 to 66 mmHg from 20 to 45 y.o., followed by a marked increase to 80 mmHg at 80 y.o.. Indeed, McEniery*et al*[108] report brachial pulse pressures of 50, 47 and 57 mmHg at 20, 40 and 80 y.o.. Similarly, Franklin and colleagues[57] and Redheuil*et al*[142] measured values of 37, 36 and 56 mmHg and 48, 46 and 66 at 20, between 40 and 50, and more then 70 years old subjects, respectively. Substantially analogous trend has been reported by Kim and co-workers, who found values of 46, 46 and 50 at 20 years

old and in the third and sixth decades.

Left ventricular condition

The important changes affecting large arteries during ageing have a counterpart on the left ventricular mechanics, as already described in the Section 4.4.1.. The resulting age-dependent left ventricular pressure-volume loop is reported in figure 4.12. The ascending

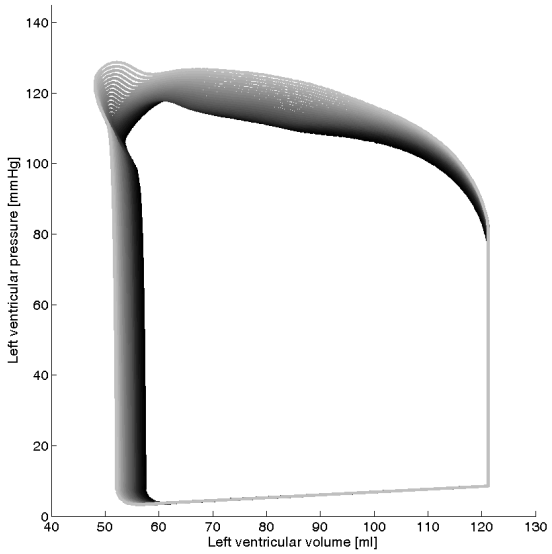

Figure 4.12. Left ventricular pressure-volume loop at different age. From 20 to 80 y.o., with 2.5 years step. The darker the younger.

aortic systolic pressure growth has its counterpart in the increasing left-ventricular pressure during the ejecting phase. Furthermore, the end-systolic volume, i.e. the left-ventricular volume at the end of the ejection, is almost preserved, as found by several authors [54;108;159]. As measured by Mangoni *et al.* [106], these changes result in an increased left-ventricular work, which our model quantifies in about 17 %, from 0.9 to 1.05 Joule.

4.4.3 Discussion

In this Section we give some physical interpretations of the obtained results, along with a description and characterization of the cardiovascular ageing.

Once left-ventricular pressure exceeds the ascending aortic one the aortic valve opens, thus connecting the fulfilled ventricular volume with the arterial tree. As a result of the higher ventricular pressure a positive pressure gradient exists, thus determining an acceleration of the blood contained in the ventricular volume through the aorta. This ejected amount of blood enters the aorta and generates a first pressure pulse that propagates along the arterial tree.

Locally, the passage of pressure wave leads to a cycling stress state on the arterial walls. As described by the theory of fatigue of the material[129;196], this cycling stress entails a cumulative damage on the arterial wall matrix, especially affecting elastin, because it is mainly synthesized during early life and because undergoes a very slow turnover[4;193]. Differently, the larger turnover of the collagen and its enhanced cross-link imply a good conservation of its overall mechanical properties[4].

The reduction of elastin presence and the continuous collagen synthetization determine a progressively increase of collagen predominance in relation to elastin[4;193]. Since collagen is much more stiffer that elastin, large arteries matrix stiffens with age[193]. Vessels structural properties reflect on the celerity of propagation of waves. Indeed, the stiffer the vessel walls are, the faster the travelling waves propagates.

At the same time, several processes, whose description is out of the scope of the present analysis, concur in a plastic increase on diameter. Briefly, a mix of pro-inflammatory mechanisms, the exhaustion of aortic distensibility reserve[4] and collagen and fibronectin expression over a progressively-more damaged matrix seem to play key roles in such a plastic deformation.

It is important to underline that an increase in diameter entails a rise of vessel deformation capacity, thus producing a decrease in pulse wave velocity c for a given incremental Young modulus E_{inc} and arterial wall thickness h. Indeed, Moens-Korteweg relation

reads

$$c = \sqrt{\frac{E_{inc}h}{D\rho}}. \tag{4.18}$$

Since during ageing the arterial wall matrix stiffening overwhelms the plastic-remodelling effect (i.e. the increase on diameter) pulse wave velocity increases with age.

Characteristic impedance and first pressure pulse

Both increased stiffness and plastic enlargement affect the capacity of an arterial section to receive an amount of blood. This property can be efficiently described by the characteristic impedance Z_C, which is a local property of an artery and, approaching the limit at high frequency of input impedance, quantifies the pressure-flow relation in absence of reflection[121;134;193], when pressure and flow are in phase[134;193]. The characteristic impedance of a given section, at least for large artery, can be calculated as

$$Z_C = \rho c/A, \tag{4.19}$$

where A is the cross-sectional area[134]. Geometrical remodelling and increase in wave celerity have antagonist roles on characteristic impedance: the former tending to decrease it, the latter increasing it.

Since characteristic impedance is obtained by neglecting viscous effect, as generally accepted at least in large arteries[193], it is a real number. Physically, the characteristic impedance of the first part of the aorta defines the load the heart would have if the aorta were infinitely long, where no reflections arise. Practically, the ventricular load is by far bigger, because the total resistance, i.e. the low frequency limit of input impedance, is much bigger than the characteristic one. In fact, more distal circulating districts are formed by very small vessels, where hydraulic resistance is higher. A classical example can be obtained by assuming Poiseuille profile in such a small vessels, thus writing resistance as

$$R = \frac{P}{Q} = \frac{8\mu l}{\pi r^4}, \tag{4.20}$$

where l is the artery length and r its radius. Resistance thus increase proportionally to the fourth power of the vessel diameter.

In figure 4.13 the resulting trend for characteristic impedance of several aortic sections over age is showed. The changes affecting

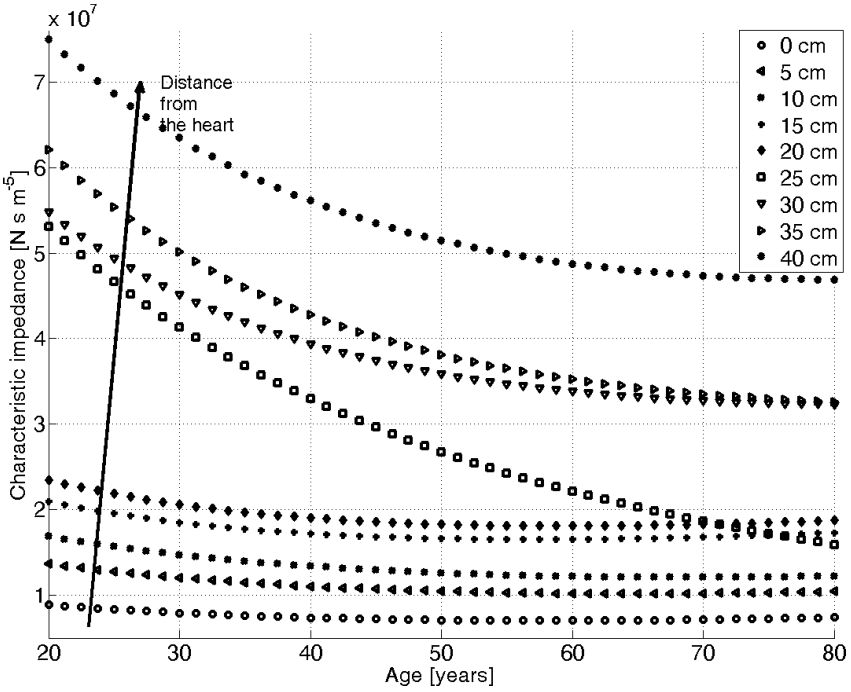

Figure 4.13. Characteristic impedance with age at every 5 cm of distance from ascending to abdominal aorta.

first aortic part entail an initial decrease of the local characteristic impedance in all the sections, although different degree of reduction are present, and a late increase at old age. Abdominal sections are characterized by larger decrease from young to middle age, while the late increase often disappear. Evidence of decreasing trend are reported in literature [4;159]. Evidently, arterial remodelling effect dominates characteristic impedance one, especially for young people.

Consequently, in the very initial ejection phase (where no reflections can interfere) the decline of characteristic impedance results in a reduction of first pressure pulse for a given ejection pattern. Furthermore, plastic enlargement produces an increase on total blood inertia, thus requiring more energy in order to accelerate blood in early systolic phase, and reducing the amount of energy

available for pressure increase in the early ejection phase.

Pulse pressure amplification

The initial pulse pressure generated by ventricular ejection subsequently propagates through the arterial network. Once travelling, the pressure pulse underneaths important changes that have a primary role on the behaviour of the cardiovascular system. In detail, the initial pulse pressure is gradually amplified (see figure 4.10) and become steeper[25;183].

In order to start the analysis of the pulse pressure amplification and of its evolution with age, we firstly introduce the theoretical model about pressure propagation proposed by Zamir[202]. Starting from one-dimensional equations describing inviscid flow in a thin, uniform and non-tethered linear elastic vessel, where only small radial displacement are considered, and further considering a non-null ending reflection coefficient, Zamir analytically obtained the pulse pressure spatial distribution along a simplified version of the aorta.

Considering the simplest case, in which a complex exponential pressure $e^{i\omega t}$ of unitary modulus is applied at the tube entrance, and neglecting re-reflection at the tube entrance, one can write[202]

$$P(x,t) = P_x(x)e^{i\omega t} = (e^{-i\omega x/c} + \Gamma e^{i\omega(x-2l)/c})e^{i\omega t} \tag{4.21}$$

where the spatial distribution $P_x(x)$ depends on the celerity of propagation c, on the length of the conduit l, on the ending reflection coefficient Γ and on the fundamental frequency of oscillation of the pressure at the entrance ω.

Applying previous formulation to a simplified version of the aorta, where lateral branches and space-dependences of both diameter and local celerity are neglected, and characterized by a fundamental frequency equal to the heart one, and further introducing age dependences on geometrical and mechanical properties and on ending reflection coefficient, one can obtain the theoretical predictions showed in figure 4.14. A total pulse pressure amplification of about 22% characterizes theoretical result at young age. Furthermore, a slight decrease on pulse pressure amplification is predicted with age, resulting in a value around 18% at 80 years old.

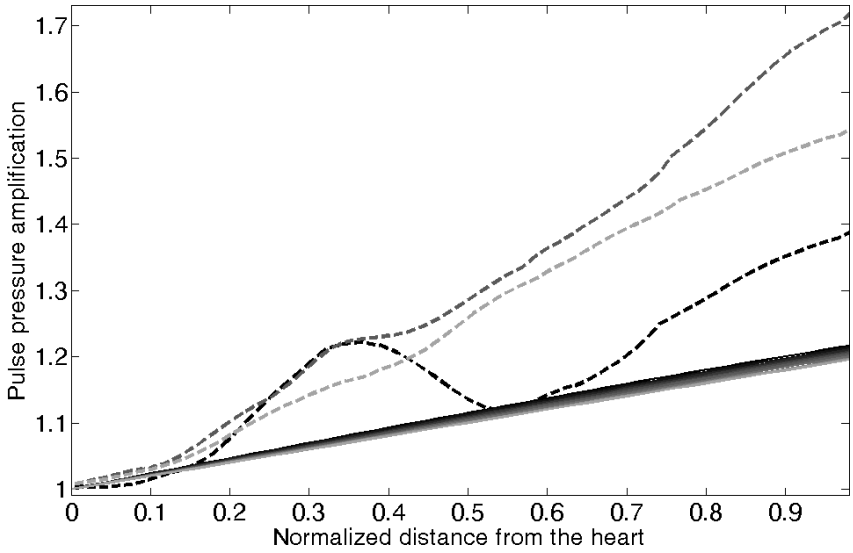

Figure 4.14. Comparison between pulse pressure amplification for a elastic uniform aorta with non-null ending resistance[202] with age (continuous lines) and model results at 20,50 and 80 y.o.. The lighter the older. Aortic length has been normalized.

Aortic length plays a major role in pulse pressure amplification: theory predicts that pulse pressure amplification assumes a cycling behaviour in space. In figure 4.15 the obtained results for a tube with aortic characteristic but by far longer than aorta (25 times) are showed. In particular, maxima distribution is regulated by the ratio of wavelength to tube length, which has changed with age by increased celerity of propagation. Such a maximum pressure wave behaviour on space affects little real aorta, since the fundamental wave-length is much more than 4 times its length, so that aortic pulse pressure increase somehow uniformly through its whole length, as shown in figure 4.14.

But real aorta is by far more complex, and other characteristics deeply influence pulse pressure amplification and can account for the depart from the analytical solution. Firstly, aorta is tapered and exhibits several bifurcations. Furthermore, it is characterized by a non-linear space-dependent viscoelastic mechanical response (see equation 2.40). The space dependence enhances pulse pressure

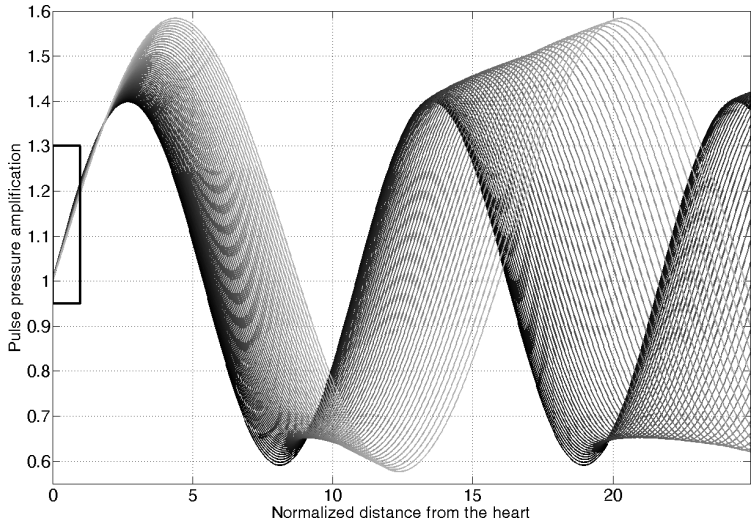

Figure 4.15. Pulse pressure amplification for a very long elastic uniform aorta with non-null ending resistance[202] with age. Distances are normalized to true aortic length. The box represent true aortic length. The lighter the older.

amplification since characteristic impedance increases when moving away from the heart[134] (see figure 4.13). The non-linearities of the mechanical response enhances celerity of propagation of the wave's peak, since celerity at systolic pressure exceeds its diastolic counterpart of around 20%[134], resulting in a steepening of travelling wave. Finally, viscous dissipation, which arises from both blood and vessel walls viscosities, attenuates pressure pulse, although in a comparatively smaller measure[134]. As expected, figure 4.14 shows how our numerical results are characterized by both higher values and less regular trends. Furthermore, aortic pulse pressure amplification increases in middle age and then declines at very old ages.

In order to understand how plastic remodelling and arterial stiffening separately affect pulse pressure amplification, suitable simulations have been conducted. In figure 4.16 we show pulse pressure evolution along the whole aorta if arterial stiffening or plastic remodelling are eliminated from normal ageing scenario.

Comparing the results shown in the uppermost and central boxes of figure 4.16, it is clear that the absence of age-related

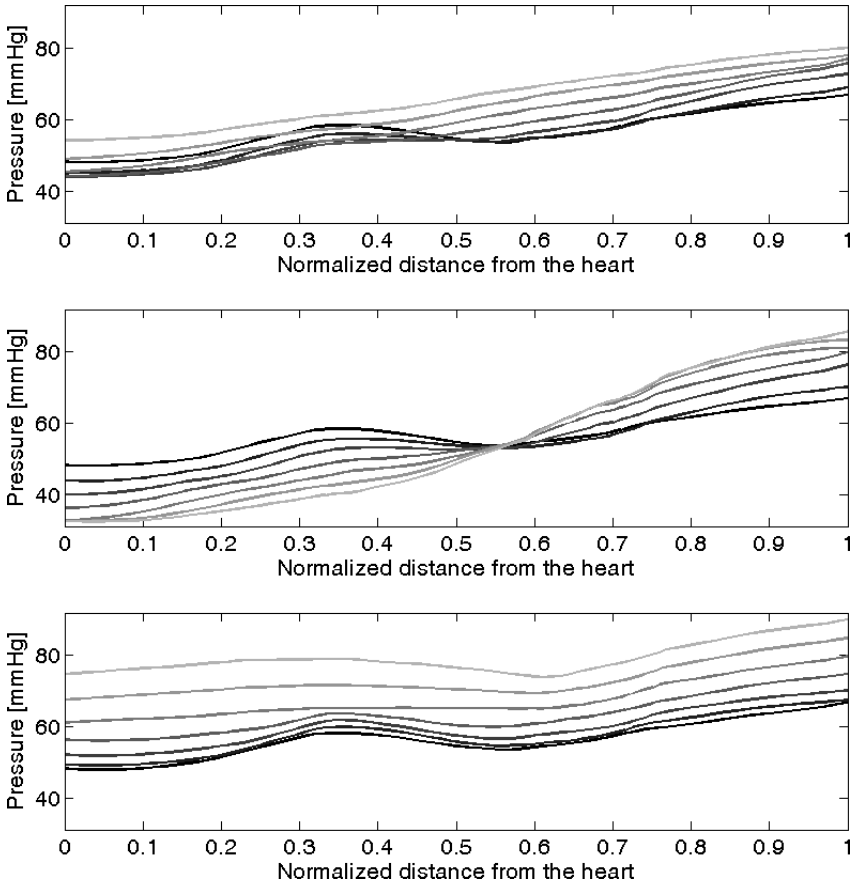

Figure 4.16. Pulse pressure along the aorta at different ages. From top to down: physiologic ageing, ageing without increase of pulse wave velocity and ageing without plastic geometric remodelling. Distances are normalized to aortic length. From 20 to 80 y.o., with 10 years step. The darker the younger.

increase on pulse wave velocity has the effect of increasing pulse pressure amplification. Indeed, ascending aortic maximum systolic pressure and thus left-ventricular work are reduced with respect to normal ageing, but late abdominal pressure is further enhanced. Specularly, the negative role of an incremented aortic celerity on ventricular condition is thus highlighted along with its reducing role on pulse pressure amplification. The role of aortic increased waves celerity on reducing pulse pressure amplification is partly

explained by the analytical solution proposed by Zamir[202] since it results in a decreased rate x/c, thus flattening the amplification trend, as shown in figure 4.14.

Differently, the bottom chart of figure 4.16 reveals that if plastic remodelling is removed, i.e. original diameters are maintained, a large increase on maximum ascending aortic pressure is observed, not accompanied by similar increase at abdominal sections. The pulse pressure amplification is thus augmented by the presence of arterial plastic remodelling, highlighting the protective role of such a deformation on ventricular work but worrying about actual pulse pressure at more distal organs.

In summary, age-related aortic increase of pulse wave velocity and diameters are antagonist with respect to the pressure pulse amplification: the former enhances aortic root pressure and reduces abdominal values, while the latter lessens proximal more that distal pressure. With age, aortic pulse pressure amplification firstly increases and then declines, highlighting that aortic enlargement dominates in early ageing and stiffening afterwards. The balance of aortic enlargement and stiffening thus play a key role in maintaining low pressure level on aortic root and other internal organs, simultaneously.

Reflection coefficients

One of the most important reasons why the theoretical predictions of the pulse pressure amplification locally deviates from the model results is related to local reflections. Indeed, every time travelling waves encounter a difference in characteristic impedance , i.e. the so-called impedance mismatch, a part of the wave is reflected and backward propagating pressure and flow waves are produced.

At a bifurcation, an approximation of the amount of backward-propagating wave produced by a change of impedance can be calculated by means of a linearisation of the governing equation and imposing the preservation of total pressure through the bifurcation [162]. This yields

$$P_b = \Gamma P_f \qquad \text{and} \qquad Q_b = -\Gamma Q_f \tag{4.22}$$

where the subscripts f and b refer to forward and backward waves,

and the reflection coefficient Γ is calculated as

$$\Gamma = \frac{Z_{C(in)} - \sum Z_{C(out)}}{Z_{C(in)} + \sum Z_{C(out)}} \tag{4.23}$$

where the subscripts *in* and *out* represent bifurcation inlet and the outlet sections, respectively. A positive reflection coefficient means that part of the forward travelling wave is reflected as a positive compression wave, so that the backward propagating pressure sums to the forward one while flow subtracts. Differently, when a pressure wave encounters a negative reflection a negative backward expansion wave is generated, which subtracts to the existing pressure and sums to the flow.

Since we here consider only motion through the aorta, i.e. we choose not to follow pressure waves along lateral branches, a bifurcation can be traversed in only two ways: forward, i.e. streamwise, or backward, i.e. going back from abdominal to aortic root sections.

The important changes affecting stiffness and size of large arteries impact reflection coefficients at various bifurcation. In figure 4.17 the reflection coefficients at aortic bifurcations are shown for both forward and backward travelling waves.

Let us firstly focus on the reflection coefficients as seen for forward travelling waves. First of all, we notice that the reflection coefficients at aortic bifurcation are very close to zero, confirming that aorta is well-matched for forward travelling waves[145]. The existing balance between characteristic impedances seen at young ages is lost at subclavian, renals and iliac bifurcations while is almost preserved in all the other bifurcations. In particular, in all these three locations reflection coefficients substantially increase and pass from negative to positive values. This means that, with advancing age, backward compression waves are generated at the place of expansion waves, resulting in an increasing sum of reflected waves generated.

Another important feature of aortic wave propagation relies in the reflection coefficient for backward propagating waves. Indeed, backward waves generated at a bifurcation are partially re-reflected at every most proximal bifurcation. At young age, bifurcations are not so much well-matched for backward propagating waves as they are for their forward counterpart[162]. This protective phenomenon has been called *wave trapping*[48;132;189] and substantially smooths

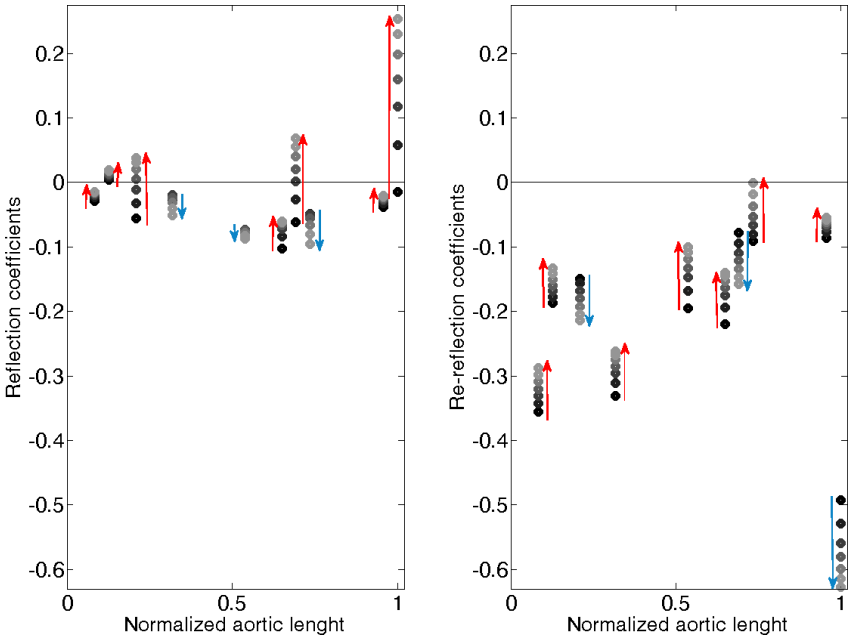

Figure 4.17. Reflection coefficients at every aortic bifurcation as seen by forward (left) and backward (right) travelling wave along the aorta during ageing. From left: Brachiocefalic, left common carotid, left subclavian, intercostals, celiac, superior mesenteric, left renal, right renal and inferior mesenteric bifurcations. From 20 to 80 y.o., with 10 years step. The darker the younger. Distance is normalized to aortic length. Arrows highlight changing directions.

out the effect of backward waves on first aortic locations, resulting in a *horizon effect*[48;121]. As showed in figure 4.17, reflection coefficients for backward waves are all negative and are generally bigger in modulus than the correspondent forward ones. A backward wave thus produces a re-reflected forward expansion wave that enhance forward flow and reduces pressure in more distal location, while the remaining pulse goes beyond the bifurcation and enhances pressure and reduces flow upstream. A more negative coefficient better protects upstream aorta from reflected wave. Our numerical results showed that most of the backward reflection coefficients move toward zero for increasing age, resulting in an increased amount of backward waves that reaches the aortic root, although an opposite behaviour is found at iliac bifurcation.

In figure 4.18 the different contributions of arterial plastic remodelling and stiffening on the most-changing reflection coefficients are shown. Since the behaviour of both reflection coefficients is only

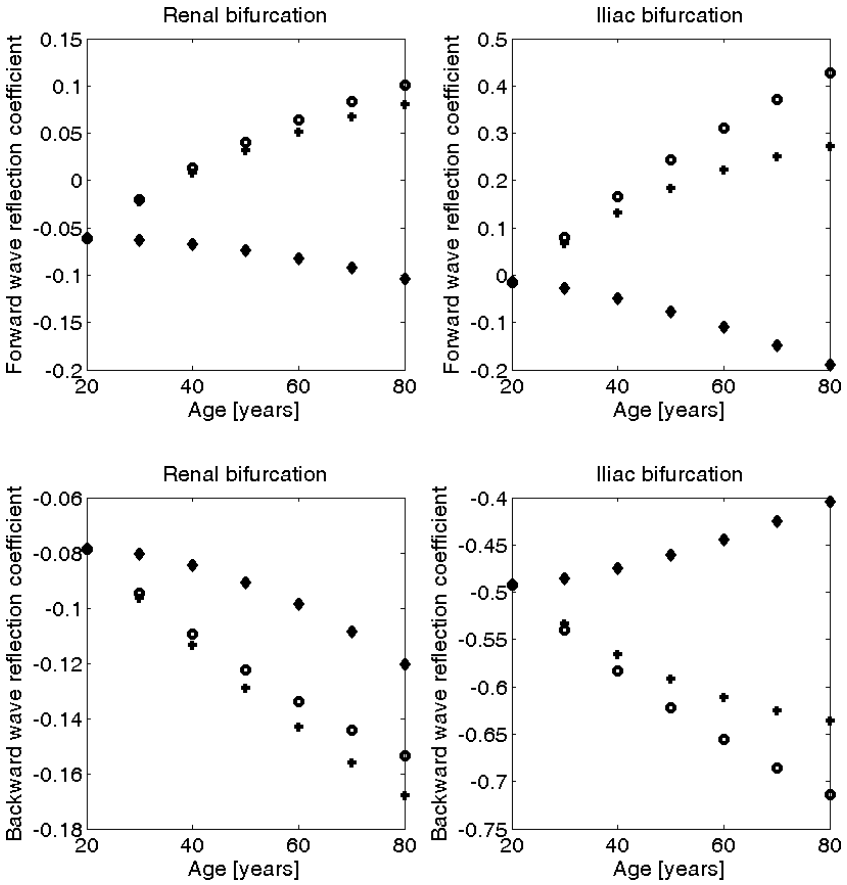

Figure 4.18. Reflection coefficients at renal (left) and iliac (right) bifurcations as seen by forward (top) and backward (bottom) travelling wave along the aorta during normal ageing (+), and without increase on pulse wave velocity (o) and on diameters (◊). From 20 to 80 y.o., with 10 years step. The darker the younger. Distance in normalized to aortic length.

slightly modified when the increase on celerity is neglected, aortic enlargement is the most impacting action. Again, it is important to point out how arterial plastic remodelling and stiffening act in

an opposite way, although here one exception exists (reflection coefficient for backward waves at renal bifurcation).

Although large reflections are generally originated at bifurcations or at very distal sections (arterioles), the general increasing trend of characteristic impedance moving away from the heart (see figure 4.13) produces a diffuse impedance mismatch and thus diffused negative reflection[36]. Consequently, although with much less degree with respect to bifurcations, reflections arise even inside every single vessel. However, the coupling between ageing-associated increase in diameter and mean wave celerity damps the difference of characteristic impedance between two generic section on the same arterial segment with advancing age, as visible in figure 4.13, at least before renal arteries. The resulting reduction of diffuse reflections exasperates the importance of reflection at bifurcations.

Increased magnitude of the reflected waves

As outlined, several processes influence the magnitude of reflected wave generated. Firstly, the initial amount of pulse pressure generated by early ventricular ejection phase creates the baseline condition. In this respect, the age-related decrease of characteristic impedance downsizes the amount of forward pressure pulse. Opposite role is played by left ventricular strengthening, which enhances ejection velocity, consequently increasing first pressure pulse. The combined effect entails a slight increase on early pulse pressure.

Secondly, the balance between arterial plastic remodelling and celerity of propagation with ageing entails a modest increase of pulse pressure amplification (see top chart of figure 4.16 and figure 4.14). Consequently, the slightly augmented amount of forward wave generate by left ventricular ejection with age is further amplified before reaching impedance mismatches. At bifurcations the large increase on reflection coefficients, mainly consequent to geometrical remodelling, further enhances backward waves generation. Finally, the reduction on trapping properties for backward wave of the aorta allows backward waves to travel in an easier way. All these processes result in an increase on reflected wave reaching first aortic sections.

Arrival time of reflected wave arrival at aortic root

Backward pressures waves sum to its forward counterpart at every location, resulting in the effective pressure. Let us introduce the transit time, i.e. the time a wave needs to reach the reflecting site and to come back to a generic section. Since we are principally interested in analysing the effect of travelling waves on left-ventricular load, we here only consider the transit time as seen from the first aortic section. Indeed, transit time variability plays a fundamental role in ascending aortic pressure profile, which in turn determines the left-ventricular load and work and it is correlated to several disease[190].

The transit time of a generic wave can change for the following reasons. Firstly, a change on the distance of reflecting site, since closer reflecting site entails lower transit times. Secondly, the celerity of propagation depends on local mechanical properties of the artery crossed and on pressure level. In fact, arteries are characterized by a non-linear elastic behaviour. For this reason, the higher the pressure is, the stiffer the arterial wall is and thus the faster the wave travels.

In order to understand the impact of such a timing on ascending aortic pressure profile, it is useful to show how pressure is composed by its forward and backward propagating pressure waves. In a frictionless system, as generally accepted in the aorta[193], one can write

$$P_f = \frac{P + Z_C Q}{2} \qquad P_b = \frac{P - Z_C Q}{2}. \tag{4.24}$$

In figure 4.19 the ascending aortic pressure decomposition is introduced. Before analysing the age-dependent evolution, we firstly concentrate on the youngest condition considered, i.e. the darkest lines in figure 4.19. Forward component steeply increases at the beginning of systole where backward propagating wave is still around minimum. Indeed, the increase of reflected component starts with less steepness and with a delay, since a definite time is needed before the amount of reflection grows to a significant value, even if reflections are known to arise also close to the ascending aorta[36]. By analysing the darkest backward pressure profile we notice the existence of three peaks (marked by arrows in the figure): the first one, which at this age corresponds to the maximum, is due to the

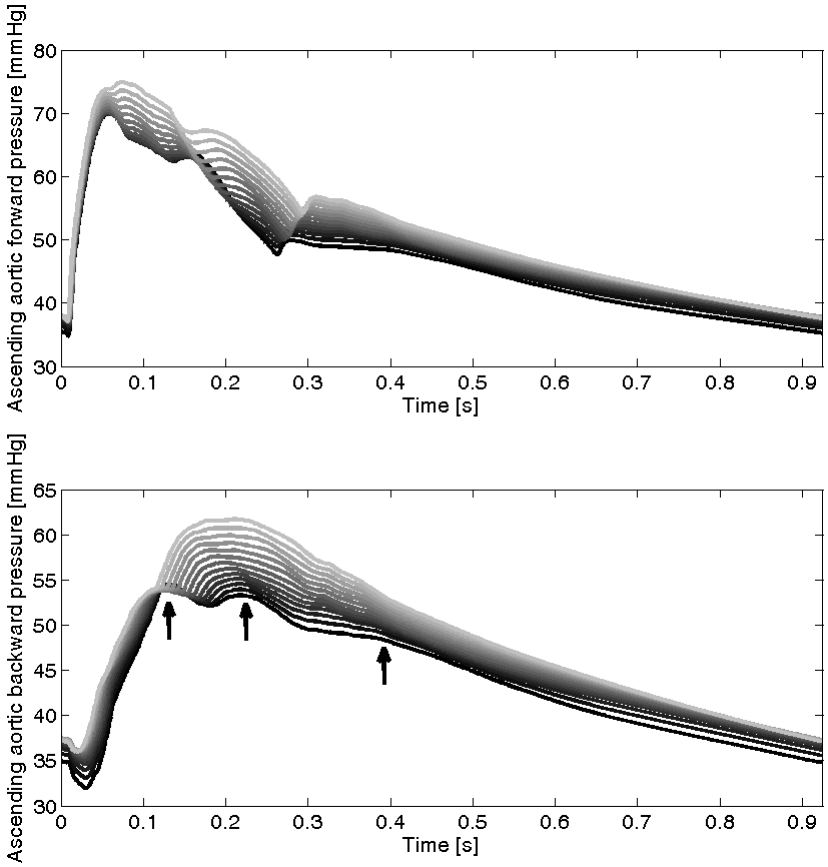

Figure 4.19. Forward (top) and backward (bottom) propagating pressures components at ascending aorta. From 20 to 80 y.o., with 5 years step. The darker the younger. Arrows indicates first, second and third peak of backward pressure waves at 20 y.o..

reflection of the closer site (mainly first aorta and arms), the second peak is primarily formed by reflections from abdominal aorta and iliac bifurcation, and the third is more diffused and principally comes from distal reflections at the end of the legs and from complex re-reflection patterns. Forward pressure wave profile presents a predominant early peak followed by a minor second peak mainly due to reflection of backward waves at the interface with the LV.

Let us firstly analyse the age effect on backward travelling pressure component. Referring to the bottom chart of figure 4.19, and

remembering that arterial stiffening is limited to the aorta, we see that the first peak (first arrow from left) moves to the left only slightly. Indeed, the second peak (central arrow) increases in magnitude and returns earlier in a much more degree, gradually merging with the first peak. Even if it does not significantly increase in magnitude, also the third peak (third arrow from left) returns earlier, determining a different curvature of the total pressure during diastole. The key role of the second peak on the maximum pressure is indisputable (see top-left box of figure 4.8 and figure 4.9). Since the second peak gradually merges to the first one, and considering the limited importance of the third peak, there is less evidence of two reflecting sites[121].

Differently, the evolution of forward pressure wave with age is minor and it mainly consists of the increased second peak due to the larger amount of backward waves that re-reflect at aortoventricular interface. Indeed, the expected increase of the forward pressure wave due to enhanced ventricular force of contraction is deeply smoothed out by the decrease of the local characteristic impedance, in turn resulting from the antagonistic balance of remodelling and stiffening.

Therefore, the early return of reflected pressure waves further enhances central systolic pressure.

Role of the left ventricle

During ageing the necessary preservation of the nutrient cell supply imposes a constraint: the mean blood flow has to be conserved in order to feed cells. The increased left-ventricular load thus enhances the strength needed to achieve a regular ejection, and the left-ventricular response has been described by the increase on maximum elastance[30–32;41;50;141].

The overall effect of increased force of contraction is the preservation of total cardiac output, as shown in figures 4.12. Indeed, simulations (not shown for sake of space) have shown that the absence of left-ventricular strengthening would entails an unacceptable decrease on mean blood ejected.

Fortunately, the tendency of enhanced force of contraction and afterload to increase first forward peak is alleviated by the ascending aortic characteristic impedance, which decreases the same

quantity. Their balance entails an almost perfect conservation of the first peak of forward pressure (see figure 4.19).

Wave intensity analysis

A detailed description of the ageing wave propagation pattern can be achieved by analysing the energy associated to single waves. To this aim, wave intensity $I(x,t)$, i.e. the product of the change in pressure ΔP and the change in flow ΔQ on sampling time[133], is here analysed. Dimensionally, the wave intensity is an energy flux per unit of sampling time carried by the waves when propagate. Forward wave results in a positive wave intensity while backward one entails negative values. Being such a quantity the algebraic sum of its component, it is positive when forward waves dominate, negative otherwise. However, a problem of wave intensity analysis is that it depends on the time interval Δt analysed. Consequently, wave intensity is often normalized to the sampling interval Δt writing[133]

$$I = \frac{\Delta P}{\Delta t}\frac{\Delta Q}{\Delta t}. \tag{4.25}$$

In figure 4.20 a space-time plot shows wave intensity along the normalized length of the aorta during systolic period at 20, 50 and 80 years old.

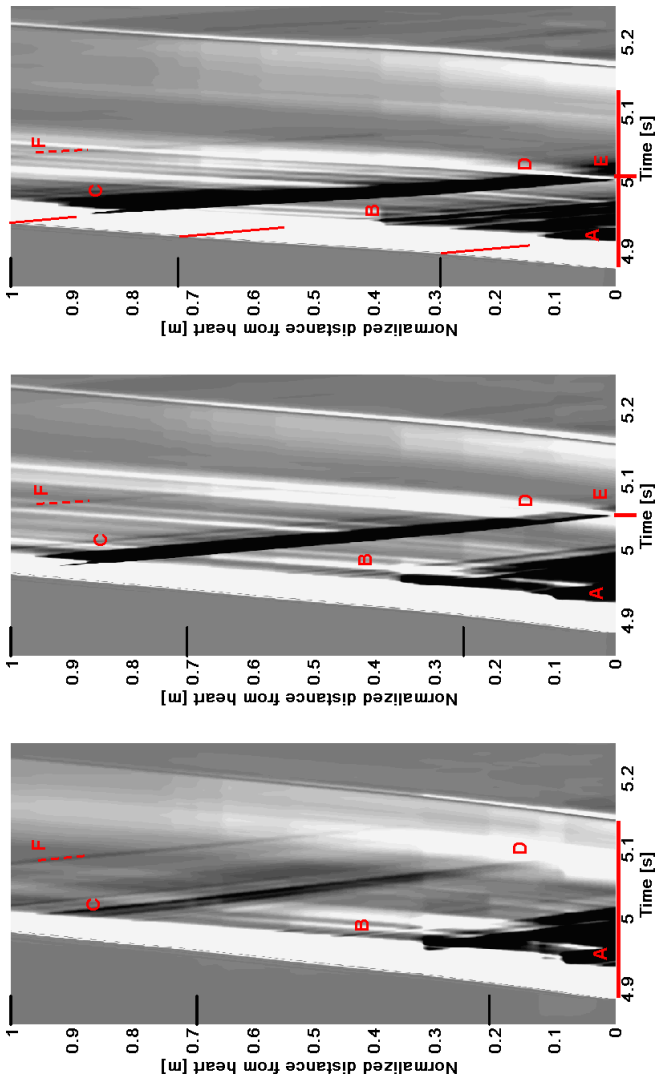

Figure 4.20. Wave intensity analysis in young (left), middle aged (center) and old (right) subject. In white positive (forward dominated) and in black negative (backward dominated) wave intensity area. Distance is normalised to aortic length. From top, horizontal lines represent iliac, renal and subclavian bifurcation positions, while red letter and lines highlight particular characteristics, which are explained in the text.

The great majority of the ageing processes analysed in the previous Sections reveals their contribution to wave intensity pattern. In particular, (i) the increase of mean celerity (see equation 4.16) is visible as an increase slope of both forward (brightest) and backward (darkest) wave fronts from left to right. (ii) The enhanced reflections at the subclavian, renal and iliac bifurcation (see figures 4.17 and 4.18) are visible as a thicker, darker reflected wave front produced at the corresponding locations (see letters A, B and C), although the presence of concomitant dominating forward waves hides the perfect location of reflected wave generations. To help the reader, we have introduced apposite red line in the right box, highlighting part of the hidden path of reflected waves. (iii) The reduction of diffuse reflection entails more defined patterns of backward dark front, as especially clear confronting left and central charts. In fact, in the left box there exist wide portions were the color is shaded, and soft transition in color happens in every directions. However, moving to the right, in these area the color contrast becomes more and more marked, showing how moving waves are more defined. These changes highlight the decreased relative importance of diffused reflections in respect to local reflections with age. (iv) The impaired re-reflections are visible as the increased distance travelled by reflected wave from, for instance, iliac bifurcation (see letter D). Indeed, looking at reflections generated at iliac bifurcation (C) in the left box, we appreciate how backward travelling waves is completely smoothed before reaching aortic arch (D). Differently, in the right box the same line lasts until reaching aortoventricular junction (E), thus demarcating the impaired protective role of reflection coefficient for backward travelling waves with age. (v) The early arriving of reflected waves at first aortic location (see figure 4.19) is clearly distinguishable. Referring again to reflection from iliac bifurcation for the sake of simplicity, we highlighted with apposite vertical lines on Time axis its arrival at aortic root in central and right boxes. In the right box reflected waves arrive early. (vi) Reflection of backward waves at the interface between left-ventricle and aortic root are visible, especially in the middle and right figures (letters E), where well-defined white line arise. These forward waves generated in last systolic portion are responsible for the second peak of forward waves seen to arise with age (see figure 4.19). (vii) Backward waves coming

from legs are almost completely smoothed out by the strong decrease of (negative) re-reflection coefficient at the iliac bifurcation (see for instance letter F and corresponding dashed lines). Indeed, backward waves travelling from the leg are clearly visible in the left box, while completely disappear with age, where iliac bifurcation increasingly isolates leg from aorta. Finally, (viii) the effect of increased left-ventricular activation time with age (see equation 4.17) is deducible from the augmented horizontal distance between first ejection front and dicrotic notch, as outlined by reporting the distance between first ejection and dicrotic notch characteristic of young age (left) on the chart of old age (see horizontal red line on abscissa).

Closing the loop

In order to help the reader to summarize the complex interacting ageing processes, in figure 4.21 a conceptual scheme is proposed.

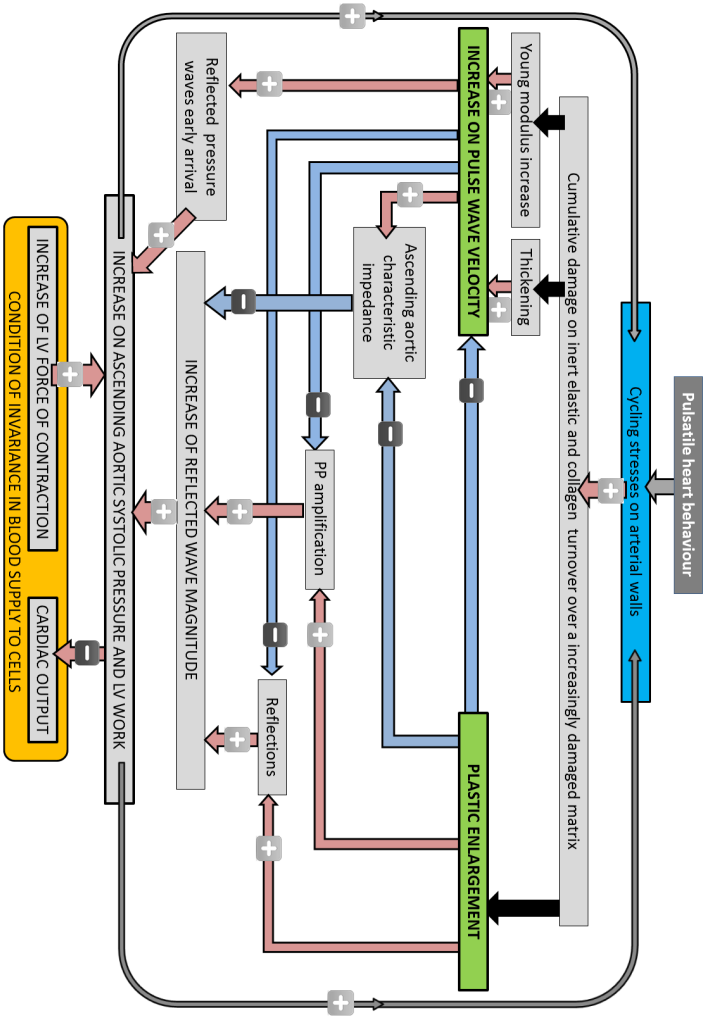

Figure 4.21. Scheme of the cardiovascular ageing process. Red arrows are associated with a negative effect (increase in PP, max systolic pressure, LV work, etc.), while blue arrows represent a beneficial effect.

The cycling behaviour of the heart induces pulsatile flow field through arteries. The consequent repeated cycling stress state acting on the arterial wall tissues entails a cumulative stress [129], especially on elastin fibre. Despite such a theory was originally deduced for non-living material, the very slow turnover of elastin determines that considerations from fatigue theory are practically efficient on this material [129]. The degeneration of elastin and the faster turnover of the stiffer collagen, along with complex biochemical activities [4], imply a stiffening and a plastic remodelling of the arterial walls. Consequently, arterial walls become stiffer and thicker, diameters grow and the very large arteries become longer. The increased incremental Young modulus and thickness enhances arterial rigidity thus fastening the celerity of propagation of waves. As we have shown, increased celerity and diameter play antagonist roles on a great variety of hemodynamic processes.

Firstly, increased pulse wave velocity enhances ascending aortic characteristic impedance, while plastic enlargement damps the same quantity (see equation 4.19). Since the effect of increased diameter overwhelms, ascending aortic characteristic impedance slightly decrease with age, especially from young to middle-aged individuals (see figure 4.13). Secondly, both arterial pulse wave velocity and cross-section affect pulse pressure amplification: the former tends to decrease pulse pressure amplification while the latter to increase it. Celerity of propagation tends to increase pulse pressure at first aortic sections and to decrease it more distally while plastic remodelling ensues mayor decrease on proximal aorta (see figure 4.16). The resulting behaviour is characterized by a slight increase in pulse pressure amplification. The antagonist role of arterial stiffening and geometrical growth is further evident analysing the changes of reflection at the most important bifurcations (see figures 4.17 and 4.18). Geometrical remodelling largely dominates the opposing role of aortic stiffening, thus resulting in a rise of reflection coefficients at main bifurcations for forward propagating waves and reducing the negative coefficients as seen for reflected waves.

The large growth of reflection coefficients entails an increased amount of reflected wave generated at main bifurcations, despite the decline of ascending aortic characteristic impedance largely mitigate this effect by reducing forward waves entity. Furthermore, the

augmented celerity of propagation anticipates the backward wave arrival at first aortic sections (see figure 4.19), thus enhancing left-ventricular work. In turn, the consequent increase of ventricular afterload tends to reduce cardiac output. Being the mean blood flow a quantity indispensable to life, the cardiac muscle responds strengthening its contracting capacity, thus maintaining a balanced ventricular-arterial interaction[30].

The overall result of the age-induced degeneration of the aortic and ventricular condition is an increase in pulse pressure throughout the vessel network. The increasing trend of aortic root pressure has been obtained without increasing distal resistances, confirming that the healthy pressure elevation is a pure result of wave propagation, as only recent studies have shown[31;141], and stressing the limitation of lumped description of the cardiovascular system [13;68], where the increase in (distal) resistance has to be imposed to overwhelm the inefficiency of reproducing wave phenomena. This pressure growth is in turn responsible for a further increase in the cumulative damage of the aortic walls, thus creating a positive loop: the more the arteries are damaged, the more they will degenerate.

4.4.4 Limitations

The limitation of the present work are mostly related to its modelling nature. Several simplification are in fact needed to reproduce the flow field. Firstly, axisymmetric geometry, wall impermeability, no longitudinal artery deformation, and Newtonian blood behaviour are assumed. Cerebral circulation, venous return, and coronary arteries are not taken into account in our model albeit their implementation would be straightforward. Furthermore, characteristic impedance is calculated neglecting viscosity, as normally accepted in large arteries[193] and therefore reflection coefficients are real numbers, and no lag is considered between forward wave arrival at an impedance mismatch and the corresponding backward wave generation. Finally, the age-dependent parameter setting is achieved by means of heterogeneous literature data. Consequently, the resulting ageing pattern should be seen as an averaged healthy process, where subject-specific conditions are not considered.

Conclusions

Mathematical description of the cardiovascular system is a fast-growing research area and the ground is ready for important step forward. The results obtained in the present Thesis, which span three years of intensive work, seem to confirm that the use of mathematical models can break the boundary between research and clinical practice.

We have developed a lumped model of the global circulation and a multi-scale (1D/0D) model of the left ventricular-arterial interaction, and both have showed strong agreement with literature data on their generic implementation.

Through the lumped model and a stochastic representation of irregular heart beat, we have been able to analyse paroxysmal atrial fibrillation, without the presence of other, often concomitant, pathologies (e.g., hypertension, atrial dilatation, mitral regurgitation), which can all concur to affect the hemodynamic response. Reduced cardiac output with correlated drop of ejection fraction and decreased amount of energy converted to work by the heart during blood pumping, as well as higher left atrial volume and pressure values are some of the most representative outcomes aligned with literature and here emerged during atrial fibrillation with respect to normal sinus rhythm.

However, the most important information come from the use of the multi-scale model. We design and test a subject-specific setting procedure, with the crucial characteristic of being based on only non-invasive measurement. The aim was to show how the adjustment of few key-parameters gives reliable subject-specific setting of the model for a population of young healthy male. The validation is carried out by quantitatively comparing outcomes of the subject-specific models with data obtained from non-invasive

in vivo measurements. Pressure at ascending aorta, brachial, radial, femoral and posterior tibial artery, along with maximum and minimum left-ventricular volume and ejection fraction, have been checked in a group of six young healthy volunteers, highlighting strong agreement.

The encouraging results obtained from the first validation allowed us to pursue further improvements in the subject-specific setting procedure for the multi-scale model. Consequently, ameliorations in the setting procedure have been introduced, avoiding the need of iterative fitting convergence for quantification of distal-model resistance, improving arterial mechanical characterization and reviewing the anthropomorphic indices used. Blind check against reference non-invasive commercial device for systolic and diastolic central pressure estimation on a population of 45 healthy young subjects has been performed. Both diastolic and systolic central pressure estimations by the mathematical model resulted to be significantly correlated with the instrument counterparts ($r=0.62$, $p<0.0001$ and $r=0.89$, $p<0.0001$ for systolic and diastolic values, respectively). However, the mathematical model significantly overestimated systolic pressures (+7 [-1,17] mmHg, $p=0.0004$) and underestimated diastolic values (-3.9 [-9,0.8] mmHg, $p=0.001$), leading to a global over-appraisal for pulse pressure. A lecture of these results can be given by analysing the performance of the reference device. Although having demonstrated impressive agreement against invasive central pressure when invasive values were used for its calibration, recent large-scale meta-analysis showed both underestimation of systolic (-8.2 ± 10.3 (mean$\pm$ SD)) and overestimation of diastolic (7.6 ± 8.7) values when fully non-invasive use is performed. Further comment on subject-specific mathematical model reliability on central pressure evaluation can be given only when invasive pressure measurement will be used as reference. To present, only a statistical viewpoint can be given, which strongly suggest the potential of this method in daily clinical activities.

Furthermore, multi-scale model has been used in understanding the cardiovascular ageing process, highlighting new features of such a complicated process. Indeed, aiming to reproduce heart-arterial interaction during ageing several physiological quantities have been modelled as a function of age. Starting from literature data, we

modified the corresponding parameters of the model, obtaining an age-dependent characterization. The quantities underlying age-dependent setting were: arterial diameter, mechanical properties, length and thickness, and left ventricular maximum elastance and systolic duration. The transversal antagonist role of aortic plastic enlargement and stiffening has been widely analysed by means of suitable simulations. Firstly, increased pulse wave velocity enhances ascending aortic characteristic impedance, while plastic enlargement lessens the same quantity. Since the effect of increased diameter overwhelms is antagonist, ascending aortic characteristic impedance slightly decrease with age, especially from young to middle-aged individuals. Secondly, both pulse wave velocity rise and cross-section growth affect pulse pressure amplification. The former tending to decrease pulse pressure amplification while the latter to increase it. The resulting behaviour is characterized by a slight increase in pulse pressure amplification. The antagonist role of arterial stiffening and geometrical growth is further evident analysing reflection coefficient changes at the most important bifurcations. The latter largely dominates the contrasting role of the former, thus resulting in a rise of reflection coefficients at main bifurcations for forward propagating waves and reducing the negative coefficients as seen for reflected waves, at least in mayor bifurcations. The large increase in reflection entails an increased amount of reflected wave generated at bifurcations, despite the decline of ascending aortic characteristic impedance largely mitigate this effect by reducing first pressure pulse. Furthermore, the augmented celerity of propagation anticipates the backward wave arrival at first aortic sections, thus enhancing left-ventricular work. In turn, the consequent increase in ventricular afterload tends to reduce cardiac output. Being mean blood flow a quantity indispensable to life, the cardiac muscle respond strengthening his contracting capacity, thus maintaining a balanced ventricular-arterial interaction. The overall result of the age-induced degeneration of the aortic and ventricular condition is an increase in pulse pressure at all the location analysed. This growth is in turn responsible of a further increase in cumulative damage on the aortic walls, thus creating a positive loop: the more the arteries are damaged, the more they will degenerate.

Concluding, pathophysiology studies could include mathematical model in their setting, and clinical use of multi-scale mathematical model appears feasible. Further work should be done to develop light, economical and practical setting procedures for different pathological conditions, and to check it against invasive pressure measurements in a wider range of conditions.

Bibliography

[1] B.R. Agner, P. Akeson, J.J. Linde, G.B. Jensen, and U. Dixen. Assessment of left atrial volume by magnetic resonance in patients with permanent atrial fibrillation. The short-axis method vs the single plane area-length method. *OCIJ*, 4:4–10, 2013.

[2] J. Alastruey, A.W. Khir, K.S. Matthys, P. Segers, S.J. Sherwin, P.R. Verdonck, K.H. Parker, and J. Peirò. Pulse wave propagation in a model human arterial network: Assessment of 1-D visco-elastic simulations against in vitro measurements. *J. Biomech.*, 44(12):2250–8, 2011.

[3] P. Alboni, S. Scarfo, G. Fuca, N. Paparella, and P. Yannacopulu. Hemodynamics of idopathic paroxysmal atrial-fibrillation. *Pacing Clin. Electrophysiol.*, 18:980–985, 1995.

[4] M. AlGhatrif and E.G. Lakatta. The reality of aging viewed from the arterial wall. In O'Rourke M. Frohlich E.D. Safar, M.E., editor, *Blood Pressure and Arterial Wall Mechanics in Cardiovascular Diseases*. Springer-Verlag, London, 2014.

[5] J.S. Alpert. Atrial fibrillation: a growth industry in the 21st century. *Eur. Heart J.*, 21:1207–1208, 2000.

[6] E. Anter, M. Jessup, and D.J. Callans. Atrial fibrillation and heart failure: treatment considerations for a dual epidemic. *Circulation*, 119:2516–2525, 2009.

[7] R.L. Armentano, J.G. Barra, D.B. Santana, F.M. Pessana, S. Graf, D. Craiem, L.M. Brandani, H.P. Baglivo, and R.A.

Sanchez. Smart damping modulation of carotid wall energetics in human hypertension: effects of angiotensin-converting enzyme inhibition. *Hypertension*, 47(3):384–90, 2006.

[8] A.P. Avolio. Multi-branched model of the human arterial system. *Med. Biol. Eng. Comput.*, 18(6):709–18, 1980.

[9] A.P. Avolio, F.Q. Deng, W.Q. Li, Y.F. Luo, Z.D. Huang, L.F. Xing, and M.F. O'Rourke. Effects of aging on arterial distensibility in populations with high and low prevalence of hypertension: comparison between urban and rural communities in China. *Circulation*, 71(2):202–210, 1985.

[10] O.K. Baskurt and H.J. Meiselman. Blood rheology and hemodynamics. *Seminars in thrombosis and hemostasis*, 29(5):435–450, 2003.

[11] A. Benetos, S. Laurent, A.P. Hoeks, P.H. Boutouyrie, and M.E. Safar. Arterial alterations with aging and high blood pressure. A noninvasive study of carotid and femoral arteries. *Arterioscl. Throm. Vas.*, 13(1):90–97, 1993.

[12] E.J. Benjamin, P.A. Wolf, R.B. D'Agostino, H. Silbershatz, Kannel W.B., and D. Levy. Impact of atrial fibrillation on the risk of death: the framingham heart study. *Circulation*, 98:946–952, 1998.

[13] D.S. Berger, John K., and J. Li. Concurrent compliance reduction and increased peripheral resistance in the manifestation of isolated systolic hypertension. *The American Journal of Cardiology*, 65(1):67 – 71, 1990.

[14] D. Bessems, C.G. Giannopapa, M.C.M. Rutten, and F.N. van de Vosse. Experimental validation of a time-domain-based wave propagation model of blood flow in viscoelastic vessels. *J. Biomech.*, 41(2):284–91, 2008.

[15] D. Bessems, M. Rutten, and F.N. van de Vosse. A wave propagation model of blood flow in large vessels using an approximate velocity profile function. *J. Fluid Mech.*, 580:145, 2007.

[16] M. Bessis. *Living Blood Cells and their Ultrastructure*. Springer Verlag, Heidelberg, 1973.

[17] P.J. Blanco and R.A. Feijóo. A dimensionally-heterogeneous closed-loop model for the cardiovascular system and its applications. *Med. Eng. Phys.*, 35(5):652–67, 2013.

[18] P.J. Blanco, R.A. Feijóo, and S.A. Urquiza. A unified variational approach for coupling 3D-€“1D models and its blood flow applications. *Comput. Method Appl. M.*, 196(41-44):4391–4410, 2007.

[19] P.J. Blanco, P.R. Trenhago, L.G. Fernandes, and R.A. Feijóo. On the integration of the baroreflex control mechanism in a heterogeneous model of the cardiovascular system. *Int. J. Numer. Method Biomed. Eng.*, pages 412–433, 2012.

[20] E. Bollache, N. Kachenoura, A. Redheuil, F. Frouin, E. Mousseaux, P. Recho, and D. Lucor. Descending aorta subject-specific one-dimensional model validated against in vivo data. *J. Biomech.*, 47(2):424–31, 2014.

[21] L.A. Bortolotto, O. Hanon, G. Franconi, P.H. Boutouyrie, S. Legrain, and X. Girerd. The Aging Process Modifies the Distensibility of Elastic but not Muscular Arteries. *Hypertension*, 34(4):889–892, 1999.

[22] E. Braunwald, R. Frye, M. Aygen, and J. Gilbert. Studies on Straling's law of the heart. III. Observations in patients with mitral stenosis and atrial fibrillation on the relationships between left ventricular end diastolic segment length, filling pressure, and the characteristics of ventricular contraction. *J Clin Invest*, 39:1874–1884, 1960.

[23] C.I.O. Brookes, P.A. White, M. Staples, P.J. Oldershaw, A.N. Redington, P.D. Collins, and M.I.M. Noble. Myocardial contractility is not constant during spontaneous atrial fibrillation in patients. *Circulation*, 98:1762–1768, 1998.

[24] S. Canic, C.J. Hartley, D. Rosenstrauch, J. Tambaca, G. Guidoboni, and A. Mikelić. Blood flow in compliant arteries: an effective viscoelastic reduced model, numerics, and

experimental validation. *Ann. Biomed. Eng.*, 34(4):575–92, 2006.

[25] C.G. Caro, T.J. Pedley, R.C. Schroter, and W. A. Seed. *The Mechanics of the Circulation*. Cambridge University Press, second edition, 2011. Cambridge Books Online.

[26] C.G. Caro, T.J. Pedley, R.C. Schroter, and W.A. Seed. *The Mechanics of the Circulation*. Oxford University Press, 1978.

[27] A. Caroli, S. Manini, L. Antiga, K. Passera, B. Ene-Iordache, S. Rota, G. Remuzzi, A. Bode, J. Leermakers, F.N. van de Vosse, R. Vanholder, M. Malovrh, J. Tordoir, and A. Remuzzi. Validation of a patient-specific hemodynamic computational model for surgical planning of vascular access in hemodialysis patients. *Kidney Int.*, 84(6):1237–45, 2013.

[28] L.C. Cerny and W.P. Walawender. Leonhardi Euleri's ""Principia pro motu sanguinis per arterias determinando"". *J. Biol. Phys.*, 1:41–56, 1974.

[29] Y.M. Cha, M.M. Redfield, W.K. Shen, and B.J. Gersh. Atrial fibrillation and ventricular dysfunction: a vicious electromechanical cycle. *Circulation*, 109:2839–2843, 2004.

[30] P.D. Chantler and E.G. Lakatta. Arterial-ventricular coupling with aging and disease. *Front. Physiol.*, 3(May):90, 2012.

[31] P.D. Chantler, E.G. Lakatta, and S.S. Najjar. Arterial-ventricular coupling: mechanistic insights into cardiovascular performance at rest and during exercise. *J. Appl. Physiol.*, 105:1342–1351, 2008.

[32] C.H. Chen, M. Nakayama, E. Nevo, B.J. Fetics, W.L. Maughan, and D.A. Kass. Coupled systolic-ventricular and vascular stiffening with age: implications for pressure regulation and cardiac reserve in the elderly. *JACC*, 32(5):1221–1227, 1998.

[33] P. Chen, A. Quarteroni, and G. Rozza. Simulation-based uncertainty quantification of human arterial network hemodynamics. *Int. J. Numer. Method Biomed. Eng.*, 29(6):698–721, 2013.

[34] H.M. Cheng, D. Lang, C. Tufanaru, and A. Pearson. Measurement accuracy of non-invasively obtained central blood pressure by applanation tonometry: a systematic review and meta-analysis. *Int. J. Cardiol.*, 167(5):1867–76, 2013.

[35] F. Chirillo, M.C. Brunazzi, M. Barbiero, D. Giavarina, M. Pasqualini, G. Franceschini, A. Cotogni, A. Cavarzerani, G. Rigatelli, P. Stritoni, and C. Longhini. Estimating mean pulmonary wedge pressure in patients with chronic atrial fibrillation from transthoracic doppler indexes of mitral and pulmonary venous flow velocity. *JACC*, 30:19–26, 1997.

[36] J.A. Chirinos and P. Segers. Ventricular-arterial coupling and mechanism of wave reflections. In O'Rourke M. Frohlich E.D. Safar, M.E., editor, *Blood Pressure and Arterial Wall Mechanics in Cardiovascular Diseases*. Springer-Verlag, London, 2014.

[37] A. Chugh, F. Pelosi, and F. Morady. Atrial fibrillation and atrial flutter. In K.A. Eagle and R.R. Baliga, editors, *Practical Cardiology: Evaluation and Treatment of Common Cardiovascular Disorders*. Wolters Kluwer health, Philadelphia, Pa., 2008.

[38] S.S. Chugh, R. Havmoeller, K. Narayanan, D. Singh, M. Rienstra, E.J. Benjamin, R.F. Gillum, Y.H. Kim, J.H. McAnulty, Z.J. Zheng, M.H. Forouzanfar, M. Naghavi, G.A. Mensah, M. Ezzati, and C.J.L. Murray. Worldwide epidemiology of atrial fibrillation: A global burden of disease 2010 study. *Circulation*, 2013.

[39] D.M. Clark, V.J. Plumb, A.E. Epstein, and G.N. Kay. Hemodynamic effects of an irregular sequence of ventricular cycle lengths during atrial fibrillation. *JACC*, 30:1034–1045, 1997.

[40] B. Cockburn. An introduction to the discontinuous galerkin method for convection-dominated problems. In A. Quarteroni, editor, *Advanced Numerical Approximation of Nonlinear Hyperbolic Equations*. Springer, Berlin Heidelberg, 1998.

[41] A. Cohen-Solal, B. Caviezel, T. Laperche, and R. Gourgon. Effects of aging on left ventricular-arterial coupling in man: assessment by means of arterial effective and left ventricular elastances. *J. Hum. Hypertens.*, 2(10):111–116, 1996.

[42] M.B. Conover. *Understanding Electrocardiography*. Elsevier Health Sciences, 2003.

[43] R.J. Corliss, D.H. McKenna, C.W. Crumpton, and G.G. Rowe. Hemodynamic effects after conversion of arrhythmias. *J. Clin. Invest.*, 47:1774–1786, 1968.

[44] K.S. Coyne, C. Paramore, S. Grandy, M. Mercader, M. Reynolds, and P. Zimetbaum. Assessing the direct costs of treating nonvalvular atrial fibrillation in the united states. *Value Health*, 9:348–356, 2006.

[45] D.O. Craiem, G. Chironi, A. Redheuil, M.E. Casciaro, E. Mousseaux, A. Simon, and R.L. Armentano. Aging impact on thoracic aorta 3D morphometry in intermediate-risk subjects: looking beyond coronary arteries with non-contrast cardiac CT. *Ann. Biomed. Eng.*, 40(5):1028–1038, May 2012.

[46] J.R. Crouse, U. Goldbourt, G. Evans, J. Pinsky, A.R. Sharrett, P. Sorlie, W. Riley, and G. Heiss. Risk factors and segment-specific carotid arterial enlargement in the atherosclerosis risk in communities (aric) cohort. *Stroke*, 27(1):69–75, 1996.

[47] E.G. Daoud, R. Weiss, M. Bahu, B.P. Knight, F. Bogun, R. Goyal, M. Harvey, S.A. Strickberger, K.C. Man, and F. Morady. Effect of an irregular ventricular rhythm on cardiac output. *Am. J. Cardiol.*, 78:1433–1436, 1996.

[48] J.E. Davies, J. Alastruey, D.P. Francis, N. Hadjiloizou, Z.I. Whinnett, C.H. Manisty, J. Aguado-Sierra, K. Willson, R.A. Foale, I.S. Malik, A.D. Hughes, K.H. Parker, and J. Mayet.

Attenuation of wave reflection by wave entrapment creates a "horizon effect" in the human aorta. *Hypertension*, 60(3):778–785, 2012.

[49] A. Davis, C. Holloway, A.J. Lewandowski, N. Ntusi, R.M. Nethononda, A. Pitcher, J.M. Francis, P. Leeson, S. Neubauer, and O.J. Rider. Diameters of the normal thoracic aorta measured by cardiovascular magnetic resonance imaging; correlation with gender, body surface area and body mass index. *J. Cardiov. Magn. Reson.*, 15:77, 2013.

[50] P.P. De Tombe, S. Jones, D. Burkhoff, W.C. Hunter, and D.A. Kass. Ventricular stroke work and efficiency both remain nearly optimal despite altered vascular loading. *Am. J. Physiol.-Heart C.*, 264(6):1817–1824, 1993.

[51] R.B. Devereux, G. de Simone, D.K. Arnett, L.G. Best, E. Boerwinkle, B.V. Howard, D. Kitzman, E.T. Lee, T.H. Mosley, A. Weder, and M.J. Roman. Normal limits in relation to age, body size and gender of two-dimensional echocardiographic aortic root dimensions in persons $\geq$15 years of age. *Am. J. Cardiol.*, 110(8):1189–1194, 2012.

[52] H.T. Dodge, F.T. Kirkham, and C.V. King. Ventricular dynamics in atrial fibrillation. *Circulation*, 15:335–347, 1957.

[53] D.L. Dries, D.V. Exner, B.J. Gersh, M.J. Domanski, M.A. Waclawiw, and L.W. Stevenson. Atrial fibrillation is associated with an increased risk for mortality and heart failure progression in patients with asymptomatic and symptomatic left ventricular systolic dysfunction: a retrospective analysis of the solvd trials. *JACC*, 32:695–703, 1998.

[54] A.U. Ferrari, A. Radaelli, and M. Centola. Invited review: aging and the cardiovascular system. *J. Appl. Physiol.*, 95(6):2591–2597, 2003.

[55] D.H. Fitchett. Lv-arterial coupling: interactive model to predict effect of wave reflections on lv energetics. *Am. J, Physiol.-Heart C.*, 261(4):1026–1033, 1991.

[56] L. Formaggia, D. Lamponi, and A. Quarteroni. One dimensional models for blood flow in arteries. *J. Eng. Math.*, 2002.

[57] S.S. Franklin, W. Gustin, N.D. Wong, M.G. Larson, M.A. Weber, W.B. Kannel, and D. Levy. Hemodynamic patterns of age-related changes in blood pressure: The framingham heart study. *Circulation*, 96(1):308–315, 1997.

[58] V. Fuster, L.E. Ryden, D.S. Cannom, H.J. Crijns, A.B. Curtis, K.A. Ellenbogen, J.L. Halperin, J.Y. Le Heuzey, G.N. Kay, J.E. Lowe, S.B. Olsson, E.N. Prystowsky, J.L. Tamargo, S. Wann, S.C. Smith, A.K. Jacobs, C.D. Adams, J.L. Anderson, E.M. Antman, J.L. Halperin, S.A. Hunt, R. Nishimura, J.P. Ornato, R.L. Page, B. Riegel, S.G. Priori, J.J. Blanc, A. Budaj, A.J. Camm, V. Dean, J.W. Deckers, C. Despres, K. Dickstein, J. Lekakis, K. McGregor, M. Metra, J. Morais, A. Osterspey, J.L. Tamargo, and J.L. Zamorano. Guidelines for the management of patients with atrial fibrillation acc/aha/esc 2006. *Circulation*, 114:257–354, 2006.

[59] I.T. Gabe, J.H. Gault, J. Ross, D.T. Mason, C.J. Mills, J.P. Schillingford, and E. Braunwald. Measurement of Instantaneous Blood Flow Velocity and Pressure in Conscious Man with a Catheter-Tip Velocity Probe. *Circulation*, 40(5):603–614, 1969.

[60] P.J. Gentlesk, W.H. Sauer, E.P. Gerstenfeld, D. Lin, S. Dixit, E. Zado, D. Callans, and F.E. Marchlinski. Reversal of left ventricular dysfunction following ablation of atrial fibrillation. *J. Cardiovasc. Electr.*, 18:9–14, 2007.

[61] C. Giglioli, M. Nesti, E. Cecchi, D. Landi, M. Chiostri, G.F. Gensini, V. Spini, and S.M. Romano. Hemodynamic effects in patients with atrial fibrillation submitted to electrical cardioversion. *Int. J. Cardiol.*, 168:4447–4450, 2013.

[62] A.T.M. Gosselink, P.K. Blanksma, H.J.G.M. Crijns, I.C. Van Gelder, P. De Kam, H.L. Hillege, M.G. Niemeijer, K.I. Lie, and F.L. Meijler. Left ventricular beat-to-beat performance in atrial fibrillation: contribution of Frank-Starling mechanism after short rather than long RR intervals. *JACC*, 26:1516–1521, 1995.

[63] J.S. Graettinger, R.A. Carleton, and J.J. Muenster. Circulatory consequences of change in cardiac rhythm produced in patients by transthoracic direct-current shock. *J. Clin. Invest.*, 43:2290–2302, 1964.

[64] J.C. Greenfield, A. Harley, H.K. Thompson, and A.G. Wallace. Pressure-flow studies in man during atrial fibrillation. *J. Clin. Invest.*, 47:2411–2421, 1968.

[65] S.E. Greenwald. Ageing of the conduit arteries. *J. Pathol.*, 211:157–172, 2007.

[66] S.E. Greenwald, A.C. Carter, and C.L. Berry. Effect of age on the in vitro reflection coefficient of the aortoiliac bifurcation in humans. *Circulation*, 82(1):114–123, 1990.

[67] J.B. Grotberg and O.E. Jensen. Biofluid Mechanics in Flexible Tubes. *Annu. Rev. Fluid Mech.*, 36(1):121–147, 2004.

[68] A. Guala, C. Camporeale, and L. Ridolfi. A lumped hydrodynamic model to assess ageing and hypertension effects on the aortic stiffness. *Eu. J. Mech. B. Fluid*, 35:111–116, 2012.

[69] A. Guala, C. Camporeale, F. Tosello, C. Canuto, and L. Ridolfi. Modelling and subject-specific validation of the heart-arterial tree system. *Ann. Biomed. Eng.*, 43(1):222–237, 2015.

[70] A.C. Guyton and J.E. Hall. *Textbook of medical physiology*. Elsevier Saunders, 2006.

[71] F. Haddad, S.A. Hunt, D.N. Rosenthal, and D.J. Murphy. Right ventricular function in cardiovascular disease, part i: anatomy, physiology, aging, and functional assessment of the right ventricle. *Circulation*, 117:1436–1448, 2008.

[72] P.B. Halmos and G.C. Patterson. Effect of atrial fibrillation on cardiac output. *Brit. Heart J.*, 27:719–723, 1965.

[73] N.M. Hamburg, M.M. Mott, S.J. Bigornia, M. Duess, M. Kluge, D.T. Hess, C.M. Apovian, J. Vita, and N. Gokce.

Maladaptive enlargement of the brachial artery in severe obesity is reversed with weight loss. *Vasc. Med.*, 15(3):215–22, 2010.

[74] J. Hayano, F. Yamasaki, S. Sakata, A. Okada, S. Mukai, and T. Fujinami. Spectral characteristics of ventricular response to atrial fibrillation. *Am J Physiol Heart Circ Physiol*, 273:2811–2816, 1997.

[75] T. Hennig, P. Maass, J. Hayano, and S. Heinrichs. Exponential distribution of long heart beat intervals during atrial fibrillation and their relevance for white noise behaviour in power spectrum. *J. Biol. Phys.*, 32:383–392, 2006.

[76] S.S. Hickson, M. Butlin, M. Graves, V. Taviani, A.P. Avolio, C.M. McEniery, and I.B. Wilkinson. The relationship of age with regional aortic stiffness and diameter. *JACC. Cardiovascular imaging*, 3(12):1247–1255, 2010.

[77] A. Holenstein, P. Niederer, and M. Anliker. A viscoelastic model for use in predicting arterial pulse waves. *J. Biomech. Eng.*, 102:318–326, 1980.

[78] W. Huberts, C. de Jonge, W.P.M. van der Linden, M.A. Inda, J.H.M. Tordoir, F.N. van de Vosse, and E.M.H. Bosboom. A sensitivity analysis of a personalized pulse wave propagation model for arteriovenous fistula surgery. part a: Identification of most influential model parameters. *Med. Eng. Phys.*, 35(6):810–826, 2013.

[79] J.H. Joh, H.J. Ahn, and H.C. Park. Reference diameters of the abdominal aorta and iliac arteries in the Korean population. *Yonsei Med. J.*, 54(1):48–54, 2013.

[80] P. Kalita and R. Schaefer. Mechanical Models of Artery Walls. *Arch. Comput. Method E.*, 15(1):1–36, 2007.

[81] V.S. Kaliujnaya and S.I. Kalyuzhny. The assessment of blood pressure in atrial fibrillation. *Comput. Cardiol.*, 32:287–290, 2005.

[82] W.B. Kannel, P.A. Wolf, E.J. Benjamin, and D. Levy. Prevalence, incidence, prognosis, and predisposing conditions for atrial fibrillation: population-based estimates. *Am. J. Cardiol.*, 82:2–9, 1998.

[83] T. Kawasaki, S. Sasayama, S.I. Yagi, T. Asakawa, and T. Hirai. Non-invasive assessment of the age related changes in stiffness of major branches of the human arteries. *Cardiovasc. Res.*, 21(9):678–687, 1987.

[84] F. Khaja and J.O. Parker. Hemodynamic effects of cardioversion in chronic atrial fibrillation. *Arch Intern Med*, 129:433–440, 1972.

[85] T. Killip and R.A. Baer. Hemodynamic effects after reversion from atrial fibrillation to sinus rhythm by precordial shock. *J. Clin. Invest.*, 45:658–671, 1966.

[86] E.K. Kim, S.A. Chang, S.Y. Jang, Y. Kim, S.M. Kim, J.K. Oh, Y.H. Choe, and D.K. Kim. Assessment of regional aortic stiffness with cardiac magnetic resonance imaging in a healthy Asian population. *Intern. J. Cardiovasc. Imag.*, 29:57–64, 2013.

[87] Y. Kivity and R. Collins. Non linear wave propagation in viscoelastic tubes: application to aortic rupture. *J. Biomech.*, 7:67–76, 1974.

[88] M. Kobayashi and T. Musha. 1/f fluctuation of heartbeat period. *IEEE T. Bio-Med. Eng.*, 29:456–457, 1982.

[89] T. Korakianitis and Y. Shi. Numerical simulation of cardiovascular dynamics with healthy and diseased heart valves. *J. Biomech.*, 39(11):1964–82, 2006.

[90] A.D. Krahn, J. Manfreda, R.D. Tate, F.A. Mathewson, and T.E. Cuddy. The natural history of atrial fibrillation: incidence, risk factors, and prognosis in the manitoba follow-up study. *Am. J. Med.*, 98:476–484, 1995.

[91] J. Krejza, M. Arkuszewski, S.E. Kasner, J. Weigele, A. Ustymowicz, R.W. Hurst, B.L. Cucchiara, and S.R. Messe.

Carotid artery diameter in men and women and the relation to body and neck size. *Stroke*, 37(4):1103–5, 2006.

[92] E.S.J. Kröner, H.J. Lamb, H.M.J. Siebelink, S.C. Cannegieter, P.J. van den Boogaard, E.E. van der Wall, A. de Roos, and J.J.M. Westenberg. Pulse wave velocity and flow in the carotid artery versus the aortic arch: Effects of aging. *JMRI*, 00:1–7, 2013.

[93] D.N. Ku. Blood flow in arteries. *Annu. Rev. Fluid Mech.*, 29:399–434, 1997.

[94] E.G. Lakatta. Arterial and Cardiac Aging: Major Shareholders in Cardiovascular Disease Enterprises: Part II: The Aging Heart in Health: Links to Heart Disease. *Circulation*, 107(2):346–354, 2003.

[95] E.G. Lakatta and D. Levy. Special review : Clinical cardiology : New frontiers arterial and cardiac aging : Major shareholders in cardiovascular disease enterprises part i : Aging arteries : A set up for vascular disease. *Circulation*, 107:139–146, 2003.

[96] G.J. Langewouters. *Visco-elasticity of the human aorta in vitro in relation to pressure and age*. PhD thesis, Amsterdam: Free University, 1982.

[97] R.D. Latham, N. Westerhof, P. Sipkema, B.J. Rubal, P. Reuderink, and J.P. Murgo. Regional wave travel and reflections along the human aorta: a study with six simultaneous micromanometric pressures. *Circulation*, 72(6):1257–1269, 1985.

[98] S. Laurent, P. Lacolley, X. Girerd, P. Boutouyrie, Y. Bezie, and M. Safar. Arterial stiffening: opposing effects of age- and hypertension-associated structural changes. *Can. J. Physiol. Pharamacol.*, (74):842–849, 1996.

[99] B.M. Learoyd and M.G. Taylor. Alterations with Age in the Viscoelastic Properties of Human Arterial Walls. *Circ. Res.*, 18(3):278–292, 1966.

[100] F. Liang, S. Takagi, R. Himeno, and H. Liu. Biomechanical characterization of ventricular-arterial coupling during aging: a multi-scale model study. *J. Biomech.*, 42(6):692–704, 2009.

[101] J. Lighthill. *Mathematical Biofluiddynamics*. CBMS-NSF Regional Conference Series in Applied Mathematics. Society for Industrial and Applied Mathematics, 1975.

[102] F.Y. Lin, R.B. Devereux, M.J. Roman, J. Meng, V.M. Jow, A. Jacobs, J.W. Weinsaft, L.J. Shaw, D.S. Berman, A. Gilmore, T.Q. Callister, and J.K. Min. Assessment of the thoracic aorta by multidetector computed tomography: age- and sex-specific reference values in adults without evident cardiovascular disease. *J. Cardiov. Comp. Tom.*, 2(5):298–308, 2008.

[103] D. Lloyd-Jones, R.J. Adams, T.M. Brown, M. Carnethon, S. Dai, G. De Simone, T.B. Ferguson, E. Ford, K. Furie, C. Gillespie, A. Go, K. Greenlund, N. Haase, S. Hailpern, P.M. Ho, V. Howard, B. Kissela, S. Kittner, D. Lackland, L. Lisabeth, A. Marelli, M.M. McDermott, J. Meigs, D. Mozaffarian, M. Mussolino, G. Nichol, V.L. Roger, W. Rosamond, R. Sacco, P. Sorlie, V.L. Roger, T. Thom, S. Wasserthiel-Smoller, N.D. Wong, and J. Wylie-Rosett. Heart disease and stroke statistics-2010 update a report from the american heart association. *Circulation*, 121:46–215, 2010.

[104] J.W. Magnani, M. Rienstra, H. Lin, M.F. Sinner, S.A. Lubitz, D.D. McManus, J. Dupuis, P.T. Ellinor, and E.J. Benjamin. Atrial fibrillation: current knowledge and future directions in epidemiology and genomics. *Circulation*, 124:1982–1993, 2011.

[105] A.C.I. Malossi, P.J. Blanco, and S. Deparis. A two-level time step technique for the partitioned solution of one-dimensional arterial networks. *Comput. Method Appl. M.*, 237-240:212–226, 2011.

[106] A.A. Mangoni, M.T. Kinirons, C.G. Swift, and S.H.D. Jackson. Impact of age on QT interval and QT dispersion

in healthy subjects: a regression analysis. *Age Ageing*, 32(3):326–331, 2003.

[107] K.S. Matthys, J. Alastruey, J. Peirò, A.W Khir, P. Segers, P.R. Verdonck, K.H. Parker, and S.J. Sherwin. Pulse wave propagation in a model human arterial network: assessment of 1-d numerical simulations against in vitro measurements. *J. Biomech.*, 40(15):3476–86, 2007.

[108] C.M. McEniery, Yasmin, I.R. Hall, A. Qasem, I.B. Wilkinson, and J.R. Cockcroft. Normal vascular aging: differential effects on wave reflection and aortic pulse wave velocity: the Anglo-Cardiff Collaborative Trial (ACCT). *JACC*, 46(9):1753–60, 2005.

[109] L.M. Mielniczuk, G.A. Lamas, G.C. Flaker, G. Mitchell, S.C. Smith, B.J. Gersh, S.D. Solomon, L.A. Moyé, J.L. Rouleau, J.D. Rutherford, and M.A. Pfeffer. Left ventricular end-diastolic pressure and risk of subsequent heart failure in patients following an acute myocardial infarction. *Congest. Heart Fail.*, 13:209–217, 2007.

[110] V. Milisiic and A. Quarteroni. Analysis of lumped parameter models for blood flow simulations and their relation with 1d models. *ESAIM - Math. Model. Num.*, 38:613–632, 2004.

[111] G.F. Mitchell, H. Parise, E.J. Benjamin, M.G. Larson, M.J. Keyes, J.A. Vita, R.S. Vasan, and D. Levy. Changes in arterial stiffness and wave reflection with advancing age in healthy men and women: the Framingham Heart Study. *Hypertension*, 43(6):1239–1245, 2004.

[112] J.J. Morris, M. Entman, W.C. North, Y. Kong, and H. McIntosh. The changes in cardiac output with reversion of atrial fibrillation to sinus rhythm. *Circulation*, 31:670–678, 1965.

[113] L.O. Müller and E.F. Toro. A global multiscale mathematical model for the human circulation with emphasis on the venous system. *Int. J. Numer. Method Biomed. Eng.*, 2014.

[114] H.J. Muntinga, A.T.M. Gosselink, P.K. Blanksma, P.J. De Kam, E.E. Van Der Wall, and H.J.G.M. Crijns. Left ventricular beat to beat performance in atrial fibrillation: dependence

on contractility, preload, and afterload. *Heart*, 82:575–580, 1999.

[115] J.P. Murgo, N. Westerhof, J.P. Giolma, and S.A. Altobelli. Aortic input impedance in normal man: relationship to pressure wave forms. *Circulation*, 62(1):105–116, 1980.

[116] J.P. Mynard, M.R. Davidson, D.J. Penny, and J.J. Smolich. A simple, versatile valve model for use in lumped parameter and one-dimensional cardiovascular models. *Int. J. Numer. Method Biomed. Eng.*, (28):626–641, 2012.

[117] Y. Nagai, E.J. Metter, C.J. Earley, M.K. Kemper, L.C. Becker, E.G. Lakatta, and J.L. Fleg. Increased Carotid Artery Intimal-Medial Thickness in Asymptomatic Older Subjects With Exercise-Induced Myocardial Ischemia. *Circulation*, 98(15):1504–1509, 1998.

[118] S.S. Najjar, A. Scuteri, and E.G. Lakatta. Arterial aging: is it an immutable cardiovascular risk factor? *Hypertension*, 46(3):454–462, 2005.

[119] C. Naughton, K. Bennett, and J. Feely. Prevalence of chronic disease in the elderly based on a national pharmacy claims database. *Age Ageing*, 35(6):633–666, 2006.

[120] M. Nichols, N. Townsend, R. Luengo-Fernandez, J. Leal, A. Gray, P. Scarborough, and M. Rayner. European cardiovascular disease statistics 2012. 2012. European Heart Network, Brussels, European Society of Cardiology, Sophia Antipolis.

[121] W.W. Nichols and M.F. O'Rourke. *McDonald's blood flow in arteries*. 2005.

[122] S. Nicosia and G. Pezzinga. Mathematical models of blood flow in the arterial network. *J. Hydraul. Res.*, 45(2):188–201, 2007.

[123] A. Noordergraaf. *Physical Basis of Ballistocardiography. Proefschrift, Etc. [With a Summary in Dutch.].* Uitgeverij Excelsior, 1956.

[124] M.S. Olufsen. Structured tree outflow condition for blood flow in larger systemic arteries. *Am J Physiol Heart Circ Physiol*, pages 257–268, 1999.

[125] M.S. Olufsen, C.S. Peskin, W.Y. Kim, E.M. Pedersen, A. Nadim, and J. Larsen. Numerical simulation and experimental validation of blood flow in arteries with structured-tree outflow conditions. *Ann. Biomed. Eng.*, 28(11):1281–99, 2000.

[126] J.R. Orlando, R. Van Herick, W.S. Aronow, and H.G. Olson. Hemodynamics and echocardiograms before and after cardioversion of atrial fibrillation to normal sinus rhythm. *Chest*, 76:521–526, 1979.

[127] M.F. O'Rourke, J.V. Blazek, C.L. Morreels, and L.J. Krovetz. Pressure Wave Transmission along the Human Aorta: changes with age and in arterial degenerative disease. *Circ. Res.*, 23(4):567–579, 1968.

[128] M.F. O'Rourke, A. Farnsworth, and J. O'Rourke. Aortic dimensions and stiffness in normal adults. *JACC. Cardiovascular imaging*, 1(6):749–751, November 2008.

[129] M.F. O'Rourke and J. Hashimoto. Mechanical factors in arterial aging: a clinical perspective. *JACC*, 50(1):1–13, 2007.

[130] M. Osranek, F. Bursi, K.R. Bailey, B.R. Grossardt, R.D. Brown, S.L. Kopecky, T.S. Tsang, and J.B. Seward. Left atrial volume predicts cardiovascular events in patients originally diagnosed with lone atrial fibrillation: three-decade follow-up. *Eur. Heart J.*, 26:2556–2561, 2005.

[131] J.T. Ottesen, M.S. Olufsen, and J.K. Larsen. *Applied Mathematical Models in Human Physiology*, volume 33. 2005.

[132] K.H. Parker. An introduction to wave intensity analysis. *Med. Biol. Eng. Comput.*, 47(2):175–88, 2009.

[133] K.H. Parker and C.J.H. Jones. Forward and backward running waves in the arteries: Analysis using the method of characteristics. *J. Biomech. Eng.*, 112(3):322–326, 1190.

[134] T.J. Pedley. *The Fluid Mechanics of Large Blood Vessels.* Cambridge University Press, 1980. Cambridge Books Online.

[135] G. Pedrizzetti and F. Domenichini. Left Ventricular Fluid Mechanics: The Long Way from Theoretical Models to Clinical Applications. *Ann. Biomed. Eng.*, 2014.

[136] G. Pedrizzetti, F. Domenichini, and G. Tonti. On the left ventricular vortex reversal after mitral valve replacement. *Ann. Biomed. Eng.*, 38(3):769–773, 2010.

[137] S.M. Pikkujamsa, T.H. Makikallio, K.E.J. Airaksinen, and H.V. Huikuri. Determinants and interindividual variation of r-r interval dynamics in healthy middle-aged subjects. *Am J Physiol Heart Circ Physiol*, 280:1400–1406, 2001.

[138] E.N. Prystowsky, D.W. Benson, V. Fuster, R.G. Hart, G.N. Kay, R.J. Myerburg, G.V. Naccarelli, and D.G. Wyse. Management of patients with atrial fibrillation. *Circulation*, 93:1262–1277, 1996.

[139] A. Quarteroni. *Cardiovascular Mathematics: modeling and simulation of the circulatory system.* MSA. Springer, 2009.

[140] R. Raghu, I.E. Vignon-Clementel, C.A. Figueroa, and C.A. Taylor. Comparative Study of Viscoelastic Arterial Wall Models in Nonlinear One-dimensional Finite Element Simulations of Blood Flow. *J. Biomech. Eng.*, 133:1–11, 2011.

[141] M.M. Redfield, S.J. Jacobsen, B.A. Borlaug, R.J. Rodeheffer, and D.A. Kass. Age- and gender-related ventricular-vascular stiffening: a community-based study. *Circulation*, 112(15):2254–2262, 2005.

[142] A. Redheuil, W.C. Yu, C.O. Wu, E. Mousseaux, A. de Cesare, R. Yan, N. Kachenoura, D. Bluemke, and J.A.C. Lima. Reduced ascending aortic strain and distensibility: earliest manifestations of vascular aging in humans. *Hypertension*, 55(2):319–326, 2010.

[143] L. Resnekov and L. McDonald. Electroversion of lone atrial fibrillation and flutter including haemodynamic studies at rest and on exercise. *Brit. Heart J.*, 33:339–350, 1971.

[144] P. Reymond, Y. Bohraus, F. Perren, F. Lazeyras, and N. Stergiopulos. Validation of a patient-specific one-dimensional model of the systemic arterial tree. *Am. J. Physiol.- Heart C.*, 301(3):H1173–82, 2011.

[145] P. Reymond, F. Merenda, F. Perren, D. Rüfenacht, and N. Stergiopulos. Validation of a one-dimensional model of the systemic arterial tree. *Am. J. Physiol.- Heart C.*, 297(1):208–222, 2009.

[146] O.J. Rider, S.E. Petersen, J.M. Francis, M.K. Ali, L.E. Hudsmith, M.R. Robinson, K. Clarke, and S. Neubauer. Ventricular hypertrophy and cavity dilatation in relation to body mass index in women with uncomplicated obesity. *Heart*, 97(3):203–208, 2011.

[147] I.S. Rogers, J.M. Massaro, Q.A. Truong, A. Mahabadi, M.F. Kriegel, C.S. Fox, G. Thanassoulis, E.M. Isselbacher, U. Hoffmann, and C.J. O'Donnell. Distribution, determinants, and normal reference values of thoracic and abdominal aortic diameters by computed tomography (from the Framingham Heart Study). *Am. J. Cardiol.*, 111(10):1510–1516, 2013.

[148] S. Rokas, S. Gaitanidou, S. Chatzidou, C. Pamboucas, D. Achtipis, and S. Stamatelopoulos. Atrioventricular node modification in patients with chronic atrial fibrillation: role of morphology of rr interval variation. *Circulation*, 103:2942–2948, 2001.

[149] M.J. Roman and R.B. Devereux. Association of central and peripheral blood pressures with intermediate cardiovascular phenotypes. *Hypertension*, 63(6):1148–1153, 2014.

[150] M.J. Roman, R.B. Devereux, J.R. Kizer, E.T. Lee, J.M. Galloway, T. Ali, J.G. Umans, and B.V. Howard. Central pressure more strongly relates to vascular disease and outcome than does brachial pressure: the Strong Heart Study. *Hypertension*, 50(1):197–203, 2007.

[151] D. Rottlaender, L.J. Motloch, D. Schmidt, S. Reda, R. Larbig, M. Wolny, D. Dumitrescu, S. Rosenkranz, E. Erdmann,

and U.C. Hoppe. Clinical impact of atrial fibrillation in patients with pulmonary hypertension. *Plos One 7*, 2012.

[152] L. Ruan, W. Chen, S.R. Srinivasan, M. Sun, H. Wang, A. Toprak, and G.S. Berenson. Correlates of common carotid artery lumen diameter in black and white younger adults: the bogalusa heart study. *Stroke*, 40(3):702–707, 2009.

[153] B. Rylski, B. Desjardins, W. Moser, J.E. Bavaria, and R.K. Milewski. Gender-related changes in aortic geometry throughout life. *Eur. J. Cardio-Thorac.*, 45:805–811, 2014.

[154] M.E. Safar, J. Blacher, B. Pannier, A.P. Guerin, S.J. Marchais, P. Guyonvarc, and G.M. London. Central Pulse Pressure and Mortality in End-Stage Renal Disease. *Hypertension*, 39:735–738, 2002.

[155] K. Sagawa. *Cardiac contraction and the pressure-volume relationship.* Oxford University Press, 1988.

[156] P. Samet. Hemodynamic sequelae of cardiac arrhythmias. *Circulation*, 47:399–407, 1973.

[157] A.J. Sanfilippo, V.M. Abascal, M. Sheehan, L.B. Oertel, P. Harrigan, R.A. Hughes, and A.E. Weyman. Atrial enlargement as a consequence of atrial fibrillation a prospective echocardiographic study. *Circulation*, 82:792–797, 1990.

[158] H. Schmid-Schönbein, G. Grunau, and H. Brauer. *Exempla hämorheologica. Das strömende Organ Blut.* Albert-Roussel Pharma GmbH, 1980.

[159] P. Segers, E.R. Rietzschel, M.L. De Buyzere, S.J. Vermeersch, D. De Bacquer, L.M. Van Bortel, G. De Backer, T.C. Gillebert, and P.R. Verdonck. Noninvasive (input) impedance, pulse wave velocity, and wave reflection in healthy middle-aged men and women. *Hypertension*, 49(6):1248–55, 2007.

[160] P. Segers, N. Stergiopulos, N. Westerhof, P. Kolh, and P.R. Verdonck. Systemic and pulmonary hemodynamics assessed with a lumped-parameter heart-arterial interaction model. *J. Eng. Math.*, 47:185–199, 2003.

[161] W. Shapiro and G. Klein. Alterations in cardiac function immediately following electrical conversion of atrial fibrillation to normal sinus rhythm. *Circulation*, 38:1074–1084, 1968.

[162] S.J. Sherwin, V. Franke, J. Peirò, and K.H. Parker. One-dimensional modelling of a vascular network in space-time variables. *J. Eng. Math.*, 47:217–25, 2003.

[163] Y. Shi, P. Lawford, and R. Hose. Review of zero-d and 1-d models of blood flow in the cardiovascular system. *Biomed. Eng. Online*, 10(1):33, 2011.

[164] T. Shishido, K. Hayashi, K. Shigemi, T. Sato, M. Sugimachi, and K. Sunagawa. Single-beat estimation of end-systolic elastance using bilinearly approximated time-varying elastance curve. *Circulation*, 102(16):1983–1989, 2000.

[165] B. Sievers, S. Kirchberg, M. Addo, A. Bakan, B. Brandts, and H.J. Trappe. Assessment of left atrial volumes in sinus rhythm and atrial fibrillation using the biplane area-length method and cardiovascular magnetic resonance imaging with TrueFISP. *J. Cardiov. Magn. Reson.*, 6:855–863, 2004.

[166] H. Smulyan, R.G. Asmar, A. Rudnicki, G.M. London, and M.E. Safar. Comparative effects of aging in men and women on the properties of the arterial tree. *JACC*, 37(5):1374–1380, 2001.

[167] H. Smulyan, S.J. Marchais, B. Pannier, A.P. Guerin, M.E. Safar, and G.M. London. Influence of body height on pulsatile arterial hemodynamic data. *JACC*, 31(5):1103–1109, 1998.

[168] M. Sosnowski, B. Korzeniowska, P. Macfarlane, and M. Tendera. Relationship between r-r interval variation and left ventricular function in sinus rhythm and atrial fibrillation as estimated by means of heart rate variability fraction. *Cardiol. J.*, 18:538–545, 2011.

[169] Blausen staff. *Wikiversity Journal of Medicine.*

[170] N. Stergiopulos, B.E. Westerhof, and N. Westerhof. Total arterial inertance as the fourth element of the windkessel model. *Am. J. Physiol.*, 276(1):81–88, 1999.

[171] N. Stergiopulos, D.F. Young, and T.R. Rogge. Computer simulation of arterial flow with applications to arterial and aortic stenoses. *J. Biomech.*, 25(12):1477–1488, 1992.

[172] G.S. Suarez, S. Lampert, S. Ravid, and B. Lown. Changes in left atrial size in patients with lone atrial fibrillation. *Clin Cardiol*, 14:652–656, 1991.

[173] J. Sugawara, K. Hayashi, T. Yokoi, and H. Tanaka. Age-associated elongation of the ascending aorta in adults. *JACC. Cardiovascular imaging*, 1(6):739–748, 2008.

[174] J. Sugawara, K. Hayashi, T. Yokoi, and H. Tanaka. Carotid-Femoral Pulse Wave Velocity: Impact of Different Arterial Path Length Measurements. *Artery Res*, 4(1):27–31, 2011.

[175] M. Tanabe, K. Onishi, K. Dohi, T. Kitamura, M. Ito, T. Nobori, and T. Nakano. Assessment of left ventricular systolic function in patients with chronic atrial fibrillation and dilated cardiomyopathy using the ratio of preceding to prepreceding r-r intervals. *Int. J. Cardiol.*, 108:197–201, 2006.

[176] T. Taneja, B.W. Mahnert, R. Passman, J. Goldberger, and A. Kadish. Effects of sex and age on electrocardiographic and cardiac electrophysiological properties in adults. *PACE*, 24(1):16–21, 2001.

[177] K. Tateno and L. Glass. Automatic detection of atrial fibrillation using the coefficient of variation and density histograms of rr and δrr intervals. *Med. Biol. Eng. Comput.*, 39:664–671, 2001.

[178] S.K. Therkelsen, B.A. Groenning, J.H. Svendsen, and G.B. Jensen. Atrial and ventricular volume and function evaluated by magnetic resonance imaging in patients with persistent atrial fibrillation before and after cardioversion. *Am. J. Cardiol.*, 97:1213–1219, 2006.

[179] T.S.M. Tsang, M.E. Barnes, K.R. Bailey, C.L. Leibson, S.C. Montgomery, Y. Takemoto, P.M. Diamond, M.A. Marra, B.J. Gersh, D.O. Wiebers, G.W. Petty, and J.B. Seward. Left atrial volume: important risk marker of incident atrial fibrillation in 1655 older men and women. *Mayo Clin. Proc.*, 76:467–475, 2001.

[180] C.B. Upshaw. Hemodynamic changes after cardioversion of chronic atrial fibrillation. *Arch. Intern. Med.*, 157:1070–1076, 1997.

[181] P.V. Vaitkevicius, J.L. Fleg, J.H. Engel, F.C. O'Connor, J.G. Wright, L.E. Lakatta, F.C. Yin, and E.G. Lakatta. Effects of age and aerobic capacity on arterial stiffness in healthy adults. *Circulation*, 88(4):1456–1462, 1993.

[182] D. Valdez-Jasso, D. Bia, Y. Zocalo, R.L. Armentano, M.A. Haider, and M.S. Olufsen. Linear and nonlinear viscoelastic modeling of aorta and carotid pressure-area dynamics under in vivo and ex vivo conditions. *Ann. Biomed. Eng.*, 39(5):1438–1456, 2011.

[183] F.N. van de Vosse and N. Stergiopulos. Pulse Wave Propagation in the Arterial Tree. *Annu. Rev. Fluid Mech.*, 43(1):467–499, 2011.

[184] P. Verdecchia, G.P. Reboldi, R. Gattobigio, M. Bentivoglio, C. Borgioni, F. Angeli, E. Carluccio, M.G. Sardone, and C. Porcellati. Atrial fibrillation in hypertension: predictors and outcome. *Hypertension*, 41:218–223, 2003.

[185] S.J. Vermeersch. Determinants of pulse wave velocity in healthy people and in the presence of cardiovascular risk factors: establishing normal and reference values. *Eu. Heart J.*, 31(19):2338–2350, October 2010.

[186] R. Virmani, A.P. Avolio, W.J. Mergner, M. Robinowitz, E.E. Herderick, J.F. Cornhill, S. Guo, T. Liu, D. Ou, and M.F. O'Rourke. Effect of Aging on Aortic Morphology in Populations with High and Low Prevalence of Hypertension and Atherosclerosis. *Am. J. Pathol.*, 139(5):1119–1129, 1991.

[187] C. Vlachopoulos, K. Aznaouridis, M.F. O'Rourke, M.E. Safar, K. Baou, and C. Stefanadis. Prediction of cardiovascular events and all-cause mortality with central haemodynamics: a systematic review and meta-analysis. *Eu. Heart J.*, 31(15):1865–71, 2010.

[188] S.M.L. Wallace, Yasmin, C.M. McEniery, K.M. Mäki-Petäjä, A.D. Booth, J.R. Cockcroft, and I.B. Wilkinson. Isolated systolic hypertension is characterized by increased aortic stiffness and endothelial dysfunction. *Hypertension*, 50(1):228–233, 2007.

[189] J.J. Wang and K.H. Parker. Wave propagation in a model of the arterial circulation. *J. Biomech.*, 37:457–470, 2004.

[190] K.L. Wang, H.M. Cheng, S.H. Sung, S.Y. Chuang, C.H. Li, H.A. Spurgeon, C.T. Ting, S.S. Najjar, E.G. Lakatta, F.C.P. Yin, P. Chou, and C.H. Chen. Wave reflection and arterial stiffness in the prediction of 15-year all-cause and cardiovascular mortalities: a community-based study. *Hypertension*, 55(3):799–805, 2010.

[191] P. Weismüller, C. Kratz, B. Brandts, K. Kattenbeck, H.J. Trappe, and C. Ranke. Av nodal pathways in the r-r interval histogram of the 24-hour monitoring ecg in patients with atrial fibrillation. *Ann. Noninvas. Electro.*, 6:285–289, 2001.

[192] N. Westerhof, F. Bosman, C.J. De Vriens, and A. Noordergraaf. Analog studies of the human systemic arterial tree. *J. Biomech.*, 2(2):121–134, 1969.

[193] N. Westerhof, N. Stergiopulos, and M.I.M. Noble. *Snapshots of Hemodynamics*. Springers, 2010.

[194] R.P. Wildman, V. Mehta, T. Thompson, S. Brockwell, and K. Sutton-Tyrrell. Obesity is associated with larger arterial diameters in caucasian and african-american young adults. *Diabetes care*, 27(12):2997–2999, 2004.

[195] I.B. Wilkinson, S.S. Franklin, I.R. Hall, S. Tyrrell, and J.R. Cockcroft. Pressure Amplification Explains Why Pulse Pressure Is Unrelated to Risk in Young Subjects. *Hypertension*, 38(6):1461–1466, 2001.

[196] A. Wohler. Theorie rechteckiger eiserner Brückenbalken mit Gitterwänden und mit Blechwänden. *Zeitschrift für Bauwesen*, 5:121–166, 1855.

[197] A. Wolak, H. Gransar, L.E.J. Thomson, J.D. Friedman, R. Hachamovitch, A. Gutstein, L.J. Shaw, D. Polk, N.D. Wong, R. Saouaf, S.W. Hayes, A. Rozanski, P.J. Slomka, G. Germano, and D.S. Berman. Aortic size assessment by noncontrast cardiac computed tomography: normal limits by age, gender, and body surface area. *JACC. Cardiovascular imaging*, 1(2):200–209, 2008.

[198] B. Wozakowska-Kaplon. Changes in left atrial size in patients with persistent atrial fibrillation: a prospective echocardiographic study with a 5-year follow-up period. *Int. J. Cardiol.*, 101:47–52, 2005.

[199] J.V. Wylie, D.C. Peters, V. Essebag, W.J. Manning, M.E. Josephson, and T.H. Hauser. Left atrial function and scar after catheter ablation of atrial fibrillation. *Heart Rhythm*, 5:47–52, 2008.

[200] N. Xiao, J. Alastruey, and C.A. Figueroa. Systematic comparison between 1-D and 3-D hemodynamics in compliant arterial models. *int.J.Numer.Meth.Biomed.Engng*, 30:204–231, 2014.

[201] A.P. Yoganathan, Z. He, and S. Casey Jones. Fluid mechanics of heart valves. *Annu. Rev. Biomed. Eng.*, 6:331–62, 2004.

[202] M. Zamir. *The Physics of Pulsatile Flow*. Biological and Medical Physics, Biomedical Engineering. Springer, 2000.

[203] P.E. Zebekakis, T. Nawrot, L. Thijs, E.J. Balkestein, J. van der Heijden-Spek, L.M. Van Bortel, H.A. Struijker-Boudier, M.E Safar, and J.A. Staessen. Obesity is associated with increased arterial stiffness from adolescence until old age. *J Hypertens.*, 23(10):1839–1846, 2005.